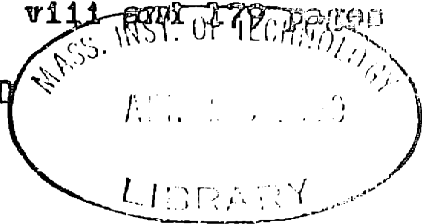


Copy No. 1 of 6 copies

Each copy contains viii and 179 pages

METHODS OF INFERRING AIRCRAFT GEOMETRY AND  
MOTION FROM MICROWAVE RADAR REFLECTIONS



DECLASSIFIED

per

Letter DSC-42:GEC/4

U.S. Navy

Bureau Navy Weapons

(dated)

8 March 1960

by

Douglas Byron Armstrong

B.A., University of Toronto  
(1940)

M.S., Massachusetts Institute of Technology  
(1951)

SUBMITTED IN PARTIAL FULFILLMENT OF THE  
REQUIREMENTS FOR THE DEGREE OF  
DOCTOR OF SCIENCE

at the

MASSACHUSETTS INSTITUTE OF TECHNOLOGY  
June, 1955

Signature of Author  
Department of Electrical Engineering, May 16, 1955

Certified by \_\_\_\_\_ Thesis Supervisor

Accepted by \_\_\_\_\_  
Chairman, Departmental Committee on Graduate Students

[REDACTED]

METHODS OF INFERRING AIRCRAFT GEOMETRY AND  
MOTION FROM MICROWAVE RADAR REFLECTIONS

by

Douglas Byron Armstrong

Submitted to the Department of Electrical Engineering on May 16, 1955  
in partial fulfillment of the requirements for the degree of  
Doctor of Science.

ABSTRACT

A study is made of the possibilities of obtaining information about the surface geometry and motion of an aircraft in flight, by suitable analysis of microwave radar return signals, for the ultimate purpose of recognizing different types of aircraft. In Chapter 1 it is shown that the maximum information deducible by microwave radar concerning the surface geometry is contained in the projected positions and intensities of the highlight areas. The thesis is therefore primarily a study of methods for determining the highlight distribution from the received radar signals.

In Chapter 2 it is shown that, for distant aircraft, the projected highlight distribution is given approximately by the Fourier transform of the received radar field over an aperture, and that the approximation can be made as exact as desired by letting the wavelength approach zero. It is also shown that the Fourier transform of the square of the amplitude of the received field yields the autocorrelation of the projected distribution. A method of computing the distribution from its autocorrelation is presented in an appendix.

The design of multireceiver radar systems for determining a one-dimensional projection of the highlights, and its autocorrelation, is studied in Chapter 3, and the possibility of detecting random aircraft motion, vibrations and propeller rotation with these systems is considered.

In Chapter 4 it is shown for a conventional radar that the short-time Fourier transform of the received doppler signal yields a "relative" one-dimensional highlight distribution, while the transform of the amplitude squared gives its autocorrelation, as before. It is predicted that random motions and vibrations should be clearly observable with conventional radars, but that propeller rotation may mask the highlight distribution.

Estimates of maximum permissible radar wavelengths for obtaining



[REDACTED]

prescribed standards of high light resolution are made in Chapter 5. It is estimated that good resolution is obtainable with a conventional radar operating at a wavelength of 2 or 3 millimeters, while the same standard of resolvability may be possible with multireceiver radars at 5 or 6 millimeters.

Chapters 6 and 7 present an experimental analysis of 3 centimeter radar data taken with a conventional radar, which shows that 3 centimeters lies approximately at the upper edge of the wavelength region in which resolution is possible. This result serves as a partial check on the validity of the preceding theory.

The important results of the thesis are summarized in Chapter 8, along with suggestions for further research.

Thesis Supervisor: H. J. Zimmermann  
Title: Associate Professor of Electrical Engineering








v

ACKNOWLEDGEMENT


The author wishes to express his appreciation to his supervisor, Professor H. J. Zimmermann, and also to the thesis readers, Professors J. B. Wiesner and R. M. Fano, for their guidance in the course of this research. The extensive facilities of the Research Laboratory of Electronics were also of great assistance in carrying out the experimental phase of the thesis.





  
TABLE OF CONTENTS

	<u>PAGE</u>
<u>CHAPTER 1. BASIC CONCEPTS OF THE RESEARCH</u>	1.
1.1 Motivation of the Research. Summary of Objectives.	1.
1.2 Previous Studies of Target Recognition by Radar.	4.
1.3 Approach to the Highlight Concept Through the Theory of Diffraction.	7.
1.4 Comparison of Visual and Microwave Viewing of Aircraft.	13.
 <u>CHAPTER 2. DEVELOPMENT OF THE FOURIER TRANSFORM RELATION BETWEEN THE APERTURE FIELD AND THE HIGHLIGHT DISTRIBUTION</u>	 18.
2.1 Fourier Transform Relation in an Optical System.	18.
2.2 Fourier Transform Relation in a Radar System.	22.
2.3 A More Exact Treatment of the Fourier Transform Relation.	24.
2.4 Highlight Information Derivable from the Amplitude of the Scattered Field.	33.
 <u>CHAPTER 3. DESIGN AND PERFORMANCE OF MULTIRECEIVER RADARS</u>	 40.
3.1 Design of a Radar to Compute Highlight Distributions Directly.	40.
3.2 Design of a Radar to Compute the Autocorrelation of Highlight Distributions.	48.
3.3 Possibility of Counting Aircraft in a Formation.	51.
3.4 Detection of Random Motion, Vibrations, and Propeller Rotation.	53.



<u>CHAPTER 4. PARTIAL DETERMINATION OF HIGHLIGHT DISTRIBUTIONS</u>	
<u>BY CONVENTIONAL RADARS</u>	56.
4.1 The Kinematics of Aircraft Motion Pertinent to Conventional Radar Measurements.	57.
4.2 Derivation and Interpretation of the Short-Time Fourier Transform in the Conventional Case.	64.
4.3 Practical Problems in Obtaining the Relative Projected Distribution.	71.
4.4 Counting Aircraft, and the Effects of Random Motion, Vibrations and Propeller Rotation.	75.
<u>CHAPTER 5. DERIVATION OF MAXIMUM ALLOWABLE WAVELENGTHS FOR</u>	
<u>PRESCRIBED RESOLUTION</u>	78.
5.1 Derivation of a General Formula for the Maximum Permissible Wavelength.	79.
5.2 Calculation of Permissible Wavelengths for a Conventional Radar.	86.
5.3 Calculation of Permissible Wavelengths for a Multireceiver Radar.	94.
<u>CHAPTER 6. DESCRIPTION OF EXPERIMENTAL DATA, METHODS OF</u>	
<u>ANALYSIS, AND EQUIPMENT</u>	98.
6.1 Description of the Experimental Data.	99.
6.2 Methods of Analysis.	100.
6.3 Description of the Analyzing Equipments.	106.
6.31 Short-Time Spectrum Analyzer.	107.
6.32 Short-Time Distribution Analyzer.	108.
6.33 Remarks Concerning Short-Time Integration.	110.

	<u>PAGE</u>
<u>CHAPTER 7. EXPERIMENTAL RESULTS</u>	114.
7.1 Probability Distributions of Target Simulator Waveforms.	115.
7.2 General Characteristics of the Experimental Data.	121.
7.3 Examples of Multi-Point Behavior, and other Results.	126.
<u>CHAPTER 8. SUMMARY, AND SUGGESTIONS FOR FURTHER RESEARCH</u>	141.
8.1 Summary of Main Results.	141.
8.2 Suggestions for Further Research.	144.
<u>APPENDIX A. EQUIPMENT DETAILS</u>	147.
A.1 Control Equipment.	147.
A.2 Short-Time Spectrum Analyzer.	150.
A.21 Low Frequency Oscillator.	151.
A.22 Channel Filter Circuit.	153.
A.23 Sequential Sampler.	158.
A.24 Remarks on the Spectrum Analyzer Design.	161.
A.3 Short-Time Distribution Analyzer.	162.
<u>APPENDIX B. EVALUATION OF THE PROJECTED DISTRIBUTION FROM     <u>ITS AUTOCORRELATION</u></u>	169.
<u>BIOGRAPHICAL NOTE</u>	176.
<u>BIBLIOGRAPHY</u>	177.

[REDACTED]

CHAPTER 1

BASIC CONCEPTS OF THE RESEARCH

1.1 Motivation of the Research. Summary of Objectives

It is well known that at microwavelengths the amplitude of the radar echo from an aircraft fluctuates rapidly, and that the rate of fluctuation increases as the wavelength is decreased. A rough explanation of this phenomenon is that the received echo is the sum of electromagnetic waves reflected from various parts of the aircraft surface, so that its amplitude (i.e., envelope) depends on the phases as well as the amplitudes of the component waves. The phase of each wave is determined by the wavelength and by the length of the two-way path from the transmitter to a particular point on the aircraft surface and back to the receiver. Specifically, a phase shift of  $(\frac{2\pi}{\lambda} \cdot \Delta R)$  results from a path length alteration of  $\Delta R$ , where  $\lambda$  is the wavelength. With a wavelength of three centimeters (and considering an aircraft of nominal size), a fraction of a degree of aspect change may alter the path length of a component wave by a wavelength or more. Such a change may result in a major variation in echo amplitude.

A plot of the echo amplitude as a function of aircraft aspect is commonly referred to as a back-scattering pattern. A typical back-scattering pattern, taken with a ten-centimeter radar and plotted in polar coordinates, is illustrated in Fig. 6.31 of reference (1) .\* The figure indicates that a 360° polar plot does not adequately show all of the fine detail in the pattern.

-----

\* Numbers in parentheses refer to numbered references in the bibliography.

[REDACTED]


[REDACTED]

Figure 13 of this thesis exhibits linear plots of echo amplitude as a function of time for a three-centimeter radar, and for different types of aircraft. A rough scale of aspect angle in degrees is included under each plot. These plots, which are sample reproductions of data obtained by J. B. Angell in the course of a doctoral research at the Research Laboratory of Electronics (2), indicate that different types of aircraft produce noticeably different echo waveform structure. An obvious example of this difference, observable in Fig. 13, is that the echo fluctuations from a large aircraft (B-29) are much more rapid than those from a small one (AT-6). Another noticeable difference occurs in the left-hand portions of the waveforms for the C-46 and B-26 aircraft, which are of roughly similar size. The C-46 echo has a much more complex structure in this region than has that of the B-26. Further differences, which are discussed in Chapter 7, will become evident to the reader upon detailed examination of the waveforms.

The presence of distinctive waveform characteristics in the three-centimeter echo data led the author to believe that they might provide a means of distinguishing between different types of aircraft. The initial task undertaken as part of the thesis research was an endeavor to analyze the Angell records in order to uncover or accentuate distinguishing features, for the purpose of achieving aircraft identification. As the work progressed, this initial motivation developed into a specific set of objectives, which are outlined below.


The theme of the investigation is based on the fact that, in the microwave region, the radar echo is composed solely of

[REDACTED]



reflections from the highlight areas on the aircraft surface. These are the regions that would appear much brighter than the remaining surface area if an aircraft were illuminated by a searchlight beam on a clear night. It is therefore evident that the highlight configuration (i.e., the relative positions of the highlight areas and their reflected intensities) contains the total information that is available to a microwave radar concerning the surface geometry of an aircraft. This fact suggests that a study of the possibility of identifying aircraft by radar may be divided into two phases: to find methods by which highlight configurations can be determined from radar echo analysis; and to determine the extent to which highlight configurations provide means for distinguishing between different aircraft types. It was decided to confine the research exclusively to the first phase, since an adequate coverage of both phases would have protracted the work unduly.

Our primary objective is therefore to conduct a theoretical study of the possibility of determining highlight configurations by microwave radar, and to test the theoretical conclusions by experimental analysis of radar echo data. An initial theoretical objective is to show that the highlight configuration can be obtained approximately by a "finite" Fourier transform of the scattered field over a small aspect interval. This will be followed by a detailed examination of the conditions under which the transform yields the highlight distribution to some prescribed degree of accuracy. One result of the theoretical study will be the proposal of a new multireceiver radar system for partially determining instantaneous highlight configurations. A thorough



[REDACTED]

investigation of the capabilities of a conventional radar with regard to highlight determination will then be made.

As a collateral result, these studies will indicate to what extent a sequence of instantaneous highlight distributions can yield information concerning the random motion of an aircraft (yaw and the like) and the character of both propeller modulation and significant nonrigid structural vibrations. The possibility of counting the number of aircraft in a formation through highlight evaluation will also be considered.

The experimental objectives are to determine the extent to which highlight configurations are revealed through analysis of the three-centimeter data recorded by Angell, and also to search for other distinguishing features of echoes that may have been overlooked by the theory. The main tools of the experimental work will be a short-time spectrum analyzer and a short-time probability distribution analyzer.

## 1.2 Previous Studies of Target Recognition by Radar

The approach to aircraft recognition through the determination of highlight configurations is quite different from most previous attacks on the problem of target identification by radar. The following short review summarizes the known work in this field.

One of the first efforts to achieve aircraft recognition by radar was made during World War II at the Radiation Laboratory, M.I.T., under the name "Project Sambo" (3). This project attempted to recognize aircraft by the character of the propeller modulation present in the echo. Spectral analyses of received envelope waveforms were made to determine the fundamental blade

[REDACTED]

[REDACTED]

frequency and the presence of significant harmonics. An essential difference between project Sambo and the present research is that the former looked only for those spectral components generated by propeller rotation, while the latter is interested in the complete spectrum produced by reflections from all parts of the aircraft surface. It will be shown subsequently that when the target is illuminated by a conventional radar the spectral components of propeller modulation may mask those produced by highlight reflections from the remainder of the aircraft. For our purposes, therefore, propeller modulation is detrimental.

Among more recent studies are two that attempt to recognize different types of terrain by airborne radar. One, undertaken by Philco (4), performed an autocorrelation analysis on echoes from sandy, rocky, and wooded terrains. It was found that no outstanding differences between terrain types were uncovered by this analysis. The other, which is being carried out by the Franklin Institute Laboratories (5), plans to subject terrain echoes to spectral, autocorrelation, and probability distribution analyses. In its theoretical approach the latter group has derived a Fourier transform relation between the received echo and a hypothesized "terrain reflectivity" function which it is hoped will exhibit distinctive characteristics for different terrains. At the time of writing, the experimental findings of this group were not available.

Another approach to aircraft recognition, carried out at the Lincoln Laboratory, M.I.T. (6), involves aural monitoring of echoes. This work indicates that the ear is able to recognize

[REDACTED]



[REDACTED]

characteristics of echo fluctuations that may not be readily detectable by other means, particularly propeller modulation characteristics. In a slightly different field, several projects have been or are being conducted (7) (8) (9) for the purpose of an accurate evaluation of radar cross sections of aircraft at various aspects. In the course of these studies a large amount of echo waveform data has been accumulated, and a careful examination of these data may reveal distinctive features.

Finally, a number of theoretical analyses of "glint" or "wander" noise in aircraft tracking radar systems have been made (2)(10), primarily for the purpose of predicting spectra of the received waveforms. The usual type of aircraft model which is postulated in this theory consists of a very large number (ideally an infinite number) of independent scatterers. In addition, a two-point scattering model has been analyzed (2). The approach bears some similarity to ours, since we are concerned with a model consisting of discrete highlight areas. However, their procedure, which prescribes the number of scatterers in advance, is an unacceptable basis for our approach, in which this number is one of the unknown quantities to be determined by the analysis.

In summary, it may be said that none of the aircraft studies mentioned above have considered the problem of determining highlight configurations. The theoretical treatment which is most similar to ours is that of the Franklin Research Institute. Their terrain reflectivity function, although continuous rather than discrete, is closely analogous to our highlight distribution. Also, they show that the reflectivity function is related to the echo field by a Fourier integral transform, which is basic to our studies

[REDACTED]

[REDACTED]

as well.

### 1.3 Approach to the Highlight Concept Through the Theory of Diffraction

The highlight concept has been briefly introduced, but a better understanding of it is required, since it plays the key role in the research. For example, we wish to know under what conditions the concept is valid, and to find methods of determining the amplitude and phase of the field returned from each highlight. Since the definition of highlight areas results from an approximate treatment the electromagnetic diffraction problem we shall briefly discuss the theory of diffraction as applied to back scattering\* from aircraft.

From the viewpoint of electromagnetic theory, the radar echo is identified with the back scattered field generated by a distribution of currents on the aircraft surface, the latter being induced by the incident field from the radar transmitter. The exact relation between the scattered field and the induced current distribution may be expressed as a vector integral equation\*<sup>†</sup>; which however cannot be solved under general conditions since the current distribution is unknown. Under restricted conditions the vector equation reduces to a much simpler scalar equation, namely the Kirchhoff-Huygens diffraction formula of physical optics. The conditions which validate the scalar formula permit the surface current distribution to be specified in terms of the incident field,

-----  
\* The back scattered field is that part of the scattered field which returns to the radar.

\*\* Reference (1) , section 6.2, equation (31).

[REDACTED]

thus making its solution possible. The validating conditions are:

(i) The radii of curvature of the aircraft surfaces are greater than approximately one wavelength.

(ii) The distance from the radar to the aircraft is very large compared to the aircraft dimensions.

For the case of back scattering, the Kirchhoff-Huygens formula is\*

$$H_S = \frac{jkH_0}{2\pi R} \int_S (\bar{n}_0 \cdot \bar{n}) e^{-j2kr} dS \quad (1)$$

where  $H_S$  is the complex scattered field at point P,  $H_0$  is the amplitude of the incident field, S is the scattering surface, O is an origin in the scatterer,  $\bar{n}_0$  is a unit vector along PO,  $\bar{n}$  is the unit normal to the surface element dS, k is  $= \frac{2\pi}{\lambda}$ , and r is the distance from P to dS, as shown in Fig. 1.

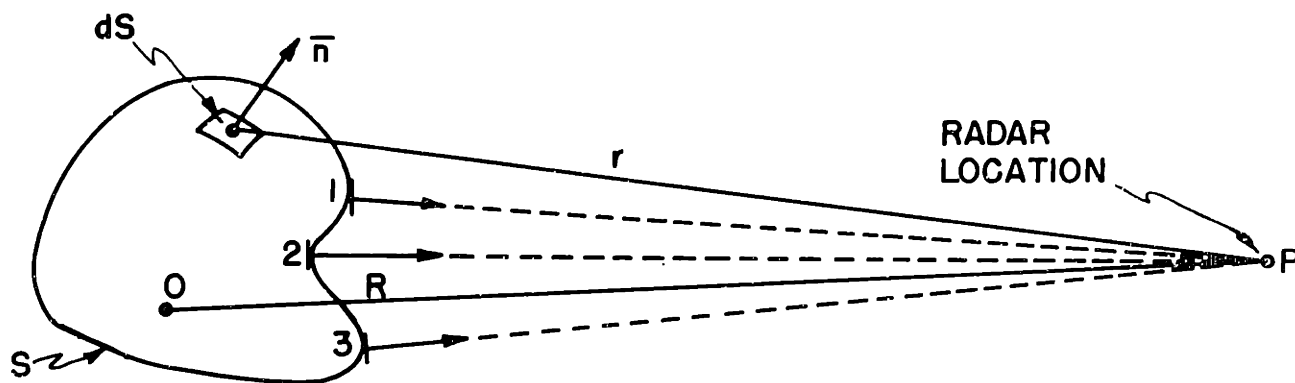


FIGURE 1

Geometry Illustrating the Kirchhoff-Huygens  
Formula for Back Scattering

\* Reference (1), section 6.2, equation (55).

[REDACTED]

Although Eq. (1) is simple in appearance, it is not easy to integrate except for elementary geometries such as planes and quadric surfaces.

When the wavelength is very much shorter than the radii of curvature of the surface, a further approximation can be made which allows Eq. (1) to be reduced to a very simple form. The reduction is achieved by applying the principle of stationary phase\*, as follows. In the immediate neighborhood of those points on the surface whose normals are in the direction of the radar, the distance  $r$  (see Fig. 1) is nearly constant. Hence the integrand of (1) assumes essentially stationary values in these neighborhoods, while on the remainder of the surface both its real and imaginary parts oscillate rapidly about zero (provided the wavelength is short enough), due to the presence of the phase term  $\exp(j2kr)$ . The oscillating integrand makes the net value of the integral zero over these regions. Thus the back scattered field is determined by the contributions from the neighborhoods of the stationary points only. These points will be called highlight points hereafter, because their neighborhoods are the highlight areas already discussed. The points numbered 1, 2 and 3 in Fig. 1 are highlight points with respect to P.

Upon applying the principle of stationary phase, Eq. (1) reduces to

$$H_S = \sum_m K_m e^{-j2kr_m} \quad (2)$$

---

\* Reference (11) , section 4.7.

[REDACTED]

where  $K_m$  is the amplitude of the field returned from the  $m$ th highlight point,  $r_m$  is the distance from this point to the radar, and the summation is over all the highlights. Note that (2) specifies both the phases and the amplitudes of the component fields arriving at the radar receiver. Furthermore, the stationary phase computation shows that  $K_m$  is proportional to

$$\left[ \frac{r_{1m} r_{2m}}{(r_{1m} + R)(r_{2m} + R)} \right]^{1/2} \quad (3)$$

where  $R$  is defined in Fig. 1, and  $r_{1m}$  and  $r_{2m}$  are the principal radii of curvature of the surface at the  $m$ th highlight point.

Normally  $R$  is  $\gg r_{1m}, r_{2m}$ , so that (3) reduces approximately to  $\frac{1}{R} [r_{1m} r_{2m}]^{1/2}$ .

Note that at wavelengths which are short enough to justify the stationary phase approximation it is also permissible to use the ray-tracing methods of geometrical optics to compute the amplitude returned from each highlight area\*. In fact, one can arrive at formula (3) by ray-tracing methods more readily than by the stationary phase analysis. The amplitudes of multiple reflections can also be computed by ray-tracing. It is probable that the most complicated multiple reflections encountered in aircraft illumination are double reflections, which can occur at the junctions of component surfaces, such as the wing and fuselage.

We observe that formula (3) is independent of wavelength, and is rigorously applicable only in the limit of zero wavelength. It

-----  
\* Reference (11) , section 4.4.

would be useful to have at least a crude criterion for determining when (3) becomes untenable at some specified (finite) wavelength. Such a criterion is forthcoming through the concept of Fresnel Zones, which clarifies the manner in which the back-scattered waves from regions outside the highlight areas cancel each other. The concept also provides an approximate means of specifying the shape and size of each highlight area. From assumption (ii), it follows that the incident and back-scattered fields are essentially planar in the vicinity of the scattering surface, the planes of constant phase being parallel to the tangent plane at any highlight point Q, as shown in Fig. 2. The annular surface regions between adjacent planes whose spacing is  $\lambda/4$  are called Fresnel half-wave zones,

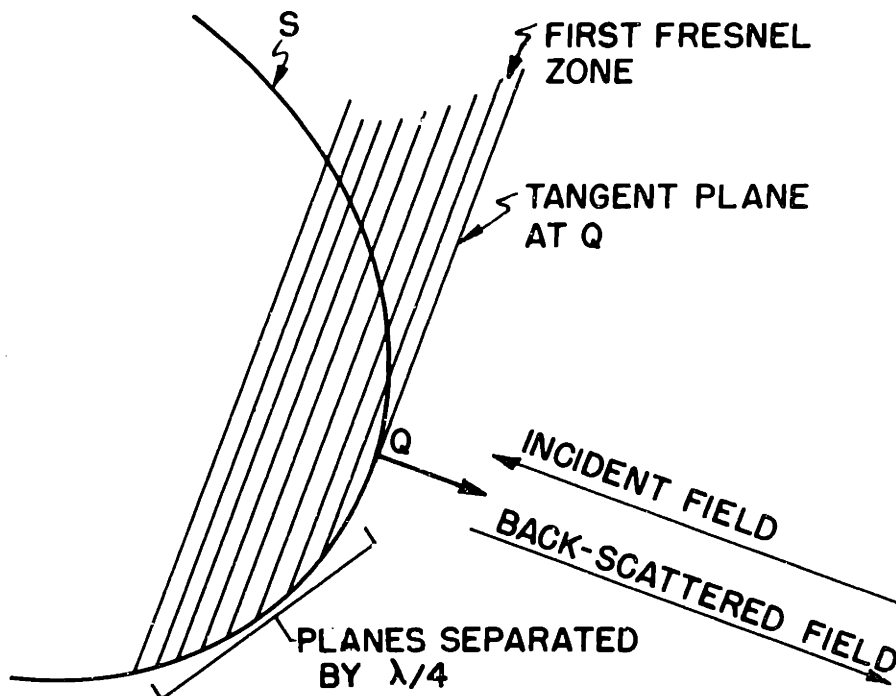


FIGURE 2  
Fresnel Zones in the Neighborhood of a  
Highlight Point

[REDACTED]

because the length of the two-way path traversed by a back-scattered wave changes by  $\lambda/2$  from one zone to the next. Hence the contributions to the back-scattered field from adjacent zones, which are approximately equal in amplitude, are opposite in phase and therefore almost exactly cancel. If a total of  $n$  zones is illuminated, it can be shown\* that the resulting back-scattered field is approximately  $(\frac{s_1 + s_n}{2})$ , where  $s_1$  and  $s_n$  are the contributions of the first and  $n$ th zones. Generally,  $s_n$  is very much smaller than  $s_1$ , and so can be ignored. Thus the back-scattered field is determined almost completely by the energy returned from the first Fresnel zone, and we may think of its boundary as defining the highlight area in question. Obviously, this is an artificial boundary because the cancellation process does not suddenly begin there; but it provides the best available definition of the shape and size of a highlight area.

It is evident from Fig. 2 that the size of the first Fresnel zone varies monotonically with the flatness of the surface in the vicinity of the highlight point. We would therefore expect the intensity of the highlight reflection to be proportional to the radii of curvature at the highlight point, and this is confirmed by formula (3). In cases where one or both of the principal radii of curvature approach infinity, such as for almost planar or cylindrical surfaces, the zones will become very extended in one or more directions, and only one or two of them may be present in their entirety. The cancellation of waves from adjacent zones will

-----  
\* Reference (12) , Chapter XIII, section 3.

then be incomplete and formula (3) becomes invalid. Of course, it also breaks down when the radii of curvature become small, such as at sharp points and edges. In the extreme cases of large and small curvatures it is generally necessary to resort to Eq. (1) for computing the scattered field accurately.

However, as the wavelength is decreased formula (3) applies with increasing accuracy in the regions of extreme curvature, as well as for the intermediate regions. At millimeter wavelengths, to which the theory of this thesis most usefully applies, it is believed that the stationary phase concept holds with acceptable accuracy for most viewing aspects of typical modern aircraft. Accordingly, we shall use Eq. (2) as the basis of the theory. To check the validity of our assumption, a comprehensive study of the surface geometry of various representative types of aircraft would be required. Other investigators (references (13) through (17) ) have considered the validity of the approximations given above for particular surface geometries, and their work lends support to our belief that the highlight point model is an adequate one for this research.

#### 1.4 Comparison of Visual and Microwave Viewing of Aircraft

Since light is electromagnetic energy whose wavelength is certainly short enough to satisfy the simplifying approximations of section 1.3, we might expect light scattering to exhibit many of the effects observed with microwave radar. However, there are four factors that assist visual observation and are partially or totally unavailable to radar. They are: atmospheric scattering, diffuse reflection, color recognition, and resolving possibilities.



[REDACTED]

We shall consider their significance in turn.

In daytime, light energy which reaches the eye from an aircraft is incident on the latter from all directions in space because of atmospheric scattering. Thus we can see the complete aircraft outline rather than just the highlight areas. This situation is in direct contrast to the radar situation, where illumination is provided from a single direction. Furthermore, aircraft surfaces are not perfectly smooth, and irregularities whose dimensions are of the order of light wavelengths, or greater, will produce diffuse rather than ideally specular reflection. Surface irregularities therefore assist in viewing complete outlines, since diffuse reflection results in a more uniform distribution of surface illumination. At microwavelengths, diffuse reflections are probably negligible because the ratio of surface roughness dimension to wavelength is small. Next, the fact that light is composed of a wide range of wavelengths permits the eye to distinguish color, a factor that may appreciably assist in visual aircraft recognition. Radar illumination, of course, does not have this facility, not only because it is essentially monochromatic, but also because the selective absorption phenomenon which causes surfaces to exhibit color effects is characteristic of light wavelengths only.

Finally, light wavelengths are so short that resolution of surface detail is possible with the use of optical systems of convenient size, even for distant objects. For example, the Rayleigh criterion of resolution which is used in physical optics states that, to resolve two points subtending an angle  $\theta$ , the required lens diameter is  $D = \frac{1.22\lambda}{\theta}$ . Thus to resolve two

[REDACTED]

points spaced five feet apart at a distance of ten miles, a lens diameter of 0.304 inches is required when yellow light is used. In comparison, at a microwavelength of five millimeters, the required lens\* diameter for the same resolution is 215 feet.

A major practical problem at millimeter wavelengths is that posed by the need of a large and complex antenna system to obtain the angular resolution cited in the preceding example (i.e., about 20 seconds of arc). Ignoring for the moment the problem of size, consider what complications are inherent in an antenna system which can resolve highlights. In a present-day radar employing a lens antenna, the resolution is not nearly adequate to separate the highlights, thus all the back-scattered energy is brought together at a single focal point in the image plane of the lens, where it is detected by a single receiving element such as a horn or dipole. When resolution is sufficient to observe individual highlights, however, the single receiving element must be replaced by a matrix of receiving elements (each with its individual receiving channel), covering a portion of the image plane. Elements of the matrix perform the same function as that of the grains of emulsion in a photographic film, or the rods and cones that comprise the retina of the eye. An additional complication is that the various types of aberrations that are present to some degree in any lens would be less tolerable in a high-resolution system than in present-day microwave lenses. To keep the aberrations within tolerable limits would place additional stringent requirements on the design of the system.

\* We are supposing here that a lens receiving antenna is used.

Thus, in view of its size and complexity, the development of a radar lens system for determining highlight configurations appears beyond the realm of practicability at present. A much simpler method of achieving the same result is proposed in this thesis. It is based on the fact that the electromagnetic field over the image plane of a lens is approximately the Fourier transform of the field over the lens aperture. This suggests the possibility of replacing the lens and its associated matrix of receivers in the image plane by a receiving matrix in the lens plane and a Fourier transform computer which operates on the output of this matrix. Actually, a one-dimensional matrix is more feasible than a two-dimensional one, although it is capable of determining only a one-dimensional projection of the highlight distribution. Details of a proposed one-dimensional system are given in Chapter 3. In Chapter 2 we shall develop the approximate Fourier transform relation in detail, in order to determine the accuracy with which it permits the computation of the highlight configuration, and to establish the design requirements which the proposed multireceiver radar must fulfill.

Chapter 4 treats the possibility of determining highlight distributions with a conventional radar, and concludes that a one-dimensional "relative projected distribution" can be obtained. Chapter 5 considers the effect of aircraft motion on highlight resolution and presents a method of determining the maximum permissible wavelength for obtaining a specified degree of resolution for a given percentage of the time. Chapters 6 and 7 are concerned with the experimental phase of the thesis. Descriptions

of the data to be analyzed, the methods of analysis, and the analyzing equipments appear in Chapter 6. The results of the experimental analysis are presented in Chapter 7. Chapter 8 includes a summary of the thesis results, and suggestions for further research. Appendices A and B present a description of equipment circuitry and a method of computing projected highlight distributions from their autocorrelation functions.




## CHAPTER 2

### Development of the Fourier Transform Relation Between the Aperture Field and the Highlight Distribution

The main objectives of this chapter are: to develop the approximate Fourier transform relation between the field over an aperture and the highlight distribution, to study the conditions that govern the accuracy of this relation, and to derive a similar relation between the square of the amplitude of the aperture field and the autocorrelation of the projected highlight distribution. In connection with this last objective, a method is presented in Appendix B for obtaining the projected highlight configuration from its autocorrelation function. The fact that this can be done under suitable circumstances is important because it will be shown in Chapter 3 that a radar system capable of evaluating the autocorrelation is a practical feasibility, while one capable of evaluating the configuration directly does not appear feasible at present. As an introduction to the Fourier transform in the radar situation, let us consider how it arises in an optical system.

#### 2.1 Fourier Transform Relation in an Optical System

We wish to show that the field over the image plane of a lens is approximately the Fourier transform of the field over the lens aperture, for distant objects subtending small angles with the optical axis of the lens. One way of showing this is based on the fact that the focussing action of a lens produces a field distribution over the image plane which is identical to the Fraunhofer (far-field) diffraction pattern of the incident light



field over the lens aperture. The Kirchhoff-Huygens formula, Eq. (1), Chapter 1, may therefore be used to evaluate the image plane field, and in this application it can be shown to reduce to a Fourier transform relation. However, we shall arrive at the result in a somewhat more heuristic manner by showing that the angular distribution of sources is the Fourier transform of the field over the lens aperture. It then follows that, since the image is ideally a replica of the source, it likewise must be related to the aperture field by a Fourier transformation.

Figure 3(a) shows an optical system in which  $(-A, A)$  is the lens aperture,  $PR$  is the optical axis of the lens, and  $(-B, B)$  is the image plane;  $Q$  is a distant point source whose principal ray,  $QPI$ , makes angle  $\delta_1$  with  $PR$ . The bundle of rays from  $Q$ , which are essentially parallel, since  $Q$  is far away, are brought to a focus at  $I$ . The surfaces of constant phase are planar above the lens and spherical below it.

Assuming the incident field to be simple harmonic in time, it follows that the spatial field distribution along  $(-A, A)$  is sinusoidal. By considering two wavefronts spaced  $\lambda$  apart, as in Fig. 3(b), it is evident that the space wavelength of the sinusoidal distribution along  $(-A, A)$  is approximately  $\lambda/\delta_1$  if  $\delta_1$  is small. The corresponding space frequency is therefore  $\delta_1/\lambda$ , so that at some particular instant of time the aperture field distribution is given by  $\sin [2\pi (\delta_1/\lambda) x]$ , where  $x$  is distance measured from the origin  $P$ . If we introduce a new length measure  $s (= x/\lambda)$ , the expression becomes  $\sin (2\pi\delta_1 s)$ , which is completely equivalent to the time domain sinusoid  $\sin (2\pi f_1 t)$ .

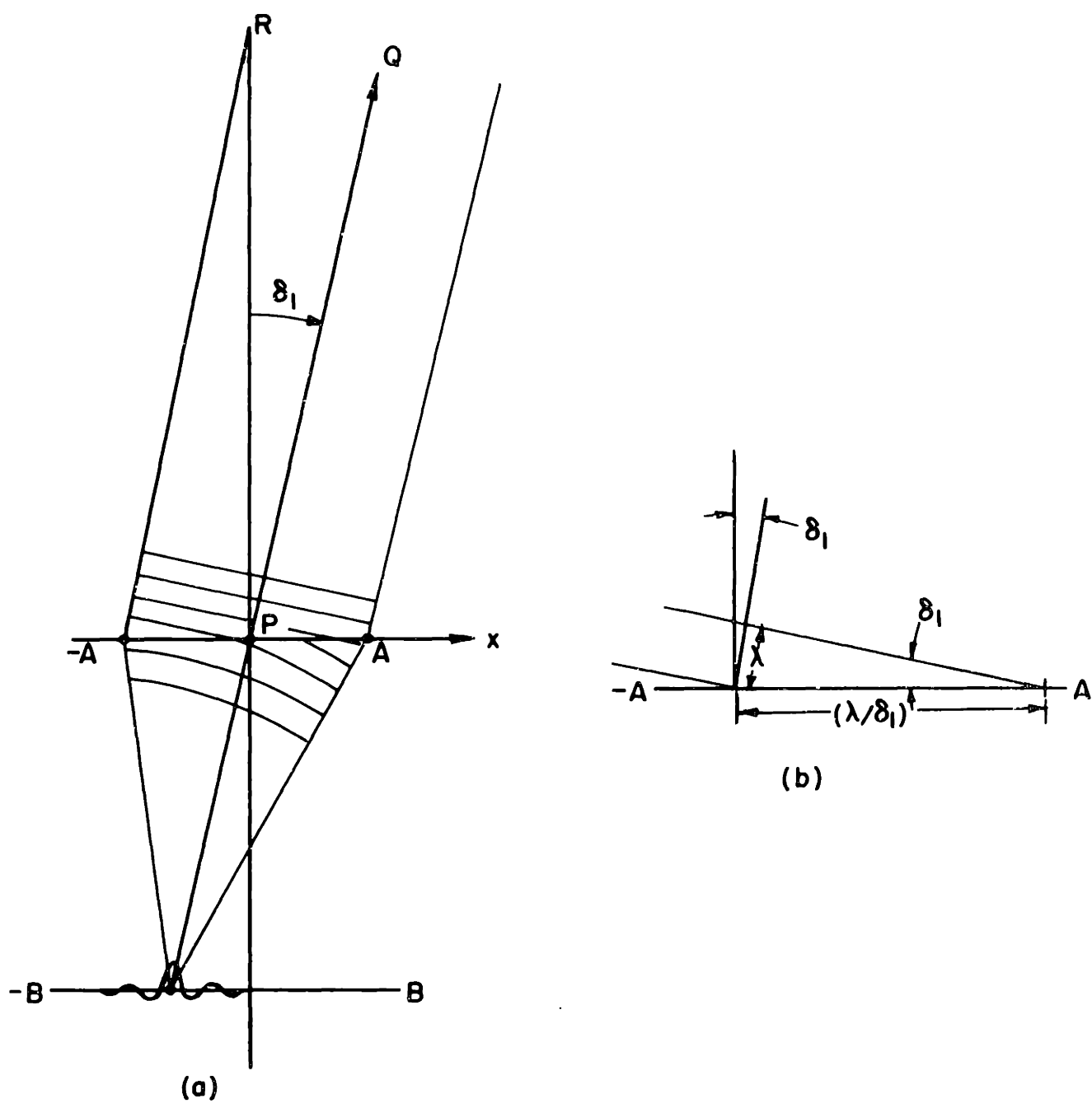


FIGURE 3

Illustration of the Fourier Transform Relation in an Optical System.

Thus  $\delta_1$  is the space frequency when the unit of length is the wavelength.

If  $\delta$  is the angle of incidence of rays arriving from distant sources, the point source in the direction of  $Q$  may be represented functionally by an impulse occurring at  $\delta = \delta_1$ . Now it is well known in Fourier transform theory that the transform of an impulse occurring at  $f_1$  in the frequency domain is the sinusoid  $\sin(2\pi f_1 t)$  in the time domain. Thus the transform of an impulse occurring at angle of incidence  $\delta_1$  is the sinusoid  $\sin(2\pi \delta_1 s)$ . But this is the aperture field distribution which was calculated above, so the desired Fourier transform relation is established.

Ideally, the image should be an exact replica of the source, except for an inversion about the optical axis. It is a familiar fact that perfect imaging is not obtainable because of the finite size of the lens aperture, which results in diffraction effects that spread the images slightly. If a rectangular lens is used, the image of a point source has  $(\sin x)/x$  distribution in the image plane. The  $(\sin x)/x$  imaging of point sources is the basis of the Rayleigh criterion of resolution which was introduced in Chapter 1. This criterion is derived in section 5.6 of reference (18). The particular image shape results from taking the Fourier transform of the aperture field, as follows. If the aperture field in complex form is represented by  $\exp(-j2\pi\delta_1 s)$ , then the angular distribution of the image field is

$$\begin{aligned}
 I(\delta) &= \frac{1}{2\pi} \int_{-A/\lambda}^{A/\lambda} \exp(-j2\pi\delta_1 s) \cdot \exp(j2\pi\delta s) ds \\
 &= \frac{A}{\pi} \frac{\sin[(\delta - \delta_1)kA]}{(\delta - \delta_1)kA} \quad (4)
 \end{aligned}$$



[REDACTED]

where  $k = 2\pi/\lambda$ . The  $(\sin x)/x$  function on the right-hand side of Eq. (4) is centered at  $\delta = \delta_1$ . It approaches an impulse function as  $kA$  approaches infinity, since the separation between its center pair of zeros is given by  $\Delta\delta = 2\pi/kA = \lambda/A$ , which approaches zero as  $A/\lambda$  approaches infinity. Obviously, resolution is improved by increasing  $A/\lambda$ , and this may be done by increasing the aperture, or decreasing the wavelength, or both. The quantity  $A/\lambda$  is called the resolving power of the lens, and perfect resolution corresponds to  $A/\lambda$  equal to infinity.

## 2.2 Fourier Transform Relation in a Radar System

The Fourier transform arises in the same manner in a radar lens system as in an optical system, and the spreading of the image due to the finite aperture is present in the radar case as well. However, an additional factor contributes to deterioration of the image shape at the wavelengths and aircraft distances that are of interest to our studies. The additional distortion arises because the aperture size required for resolution at microwavelengths is large enough to subtend an appreciable angle at the scatterer. The result is that the highlight configuration appears slightly different when observed from different points on the aperture. The effect is illustrated in an exaggerated manner in Fig. 4, where AB is the aperture, P is the radar transmitter located at its center, and S is part of a scattering surface. Consider the position of a highlight point Q as seen by receivers located at P, A, and B. They do not see the same highlight but three different ones, located at Q, Q' and Q'', respectively, the latter being located so as to satisfy Snell's law of reflection for rays emanating from P.

[REDACTED]

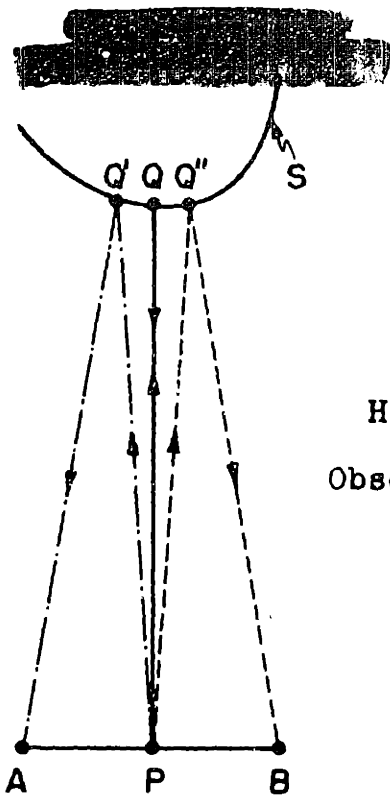


FIGURE 4  
 Highlight Point Variation  
 Observed by a Large Aperture.

Not only the position but also the amplitude returned from each highlight depends on the point of observation on the aperture because amplitude is a function of surface curvature, which varies with highlight location. Thus the aperture field distribution produced by an individual highlight is not truly sinusoidal because both its space frequency and amplitude vary over the aperture. The image of a highlight under these conditions will be more spread out than the  $(\sin x)/x$  distribution which results when the aperture is small enough so that the source appears the same at all points on it.

A further consequence of using an aperture which subtends an appreciable angle at the scatterer is that the scattered wavefronts must now be treated as spherical rather than plane. Therefore, to compute the highlight distribution as accurately as possible, the Fourier transform must be applied to the scattered field over a section of a spherical surface whose center is the scatterer, rather than over a plane as assumed in the

[REDACTED]

optical theory.

This discussion shows that at long microwavelengths, for which large apertures are required to obtain adequate resolving power, the Fourier transform of the aperture field will yield a poor replica of the highlight distribution because of significant variation in the highlight configuration when viewed from different points on the aperture. The way to eliminate this effect is to make the aperture radius small, and if we are to maintain adequate resolving power as well, the wavelength must also be made small. Both of these requirements can be met simultaneously by making  $\lambda$  approach zero at least as fast as  $A$  approaches zero.

We shall now present the analysis of this and the preceding section in a more rigorous manner, in order to bring out a number of points not made apparent in the qualitative treatment, and to introduce an adequate symbolism for quantities employed later in the thesis.

### 2.3 A More Exact Treatment of the Fourier Transform Relation

In this more rigorous treatment of the relation between the aperture field and the highlight distribution, we shall use different reference coordinates from those employed in section 2.1. Specifically, the highlight configuration will be expressed in terms of a coordinate frame whose origin is in the scatterer, and positions on the aperture will be specified by angles measured relative to one of the coordinate axes. Essentially, this means that the scattered field is expressed as a function of aircraft aspect. Equation (2), Chapter 1, will be used as the fundamental

[REDACTED]

[REDACTED]

expression for the scattered field. We shall show that it reduces to a two-dimensional Fourier transform. Following this, a one-dimensional form will be derived for the case in which the receiving aperture is a line rather than an area. In this case it will be shown that the transformation yields approximately a one-dimensional projection of the highlight configuration, and that the approximation can be made as exact as we please by letting both the aperture and the wavelength approach zero in the proper ratio.

Figure 5 (which is not drawn to scale) illustrates the geometry underlying the present analysis. Point O is the center of gravity of the scatterer, and P is the radar transmitter, whose distance from O is R. ABCD is a plane rectangle centered on P and perpendicular to OP. A'B'C'D' is a section of a spherical surface, formed by the intersection of the pyramid OABCD and the sphere having center O and radius  $R_0$ . Oxyz is a rectangular coordinate system whose x, y, and z axes are parallel to OP, BC and CD, respectively. The mth highlight point on the scatterer is  $Q_m$ , whose position vector with respect to O is  $\vec{r}_m (x_m, y_m, z_m)$ . Let an arbitrary receiving point on A'B'C'D' be denoted by S, whose position is specified by the angles  $\delta$  and  $\gamma$ , subtended between OS and the xz and xy planes, respectively. Let the boundaries of A'B'C'D' be specified by  $\delta = \pm V$ ,  $\gamma = \pm W$ .

The path length traversed by an electromagnetic wave from the transmitter to the mth highlight and back to S is  $(PQ_m + Q_m S)$ . By making a series expansion of the exact expression for this distance and retaining only the first-order terms, on the assumption

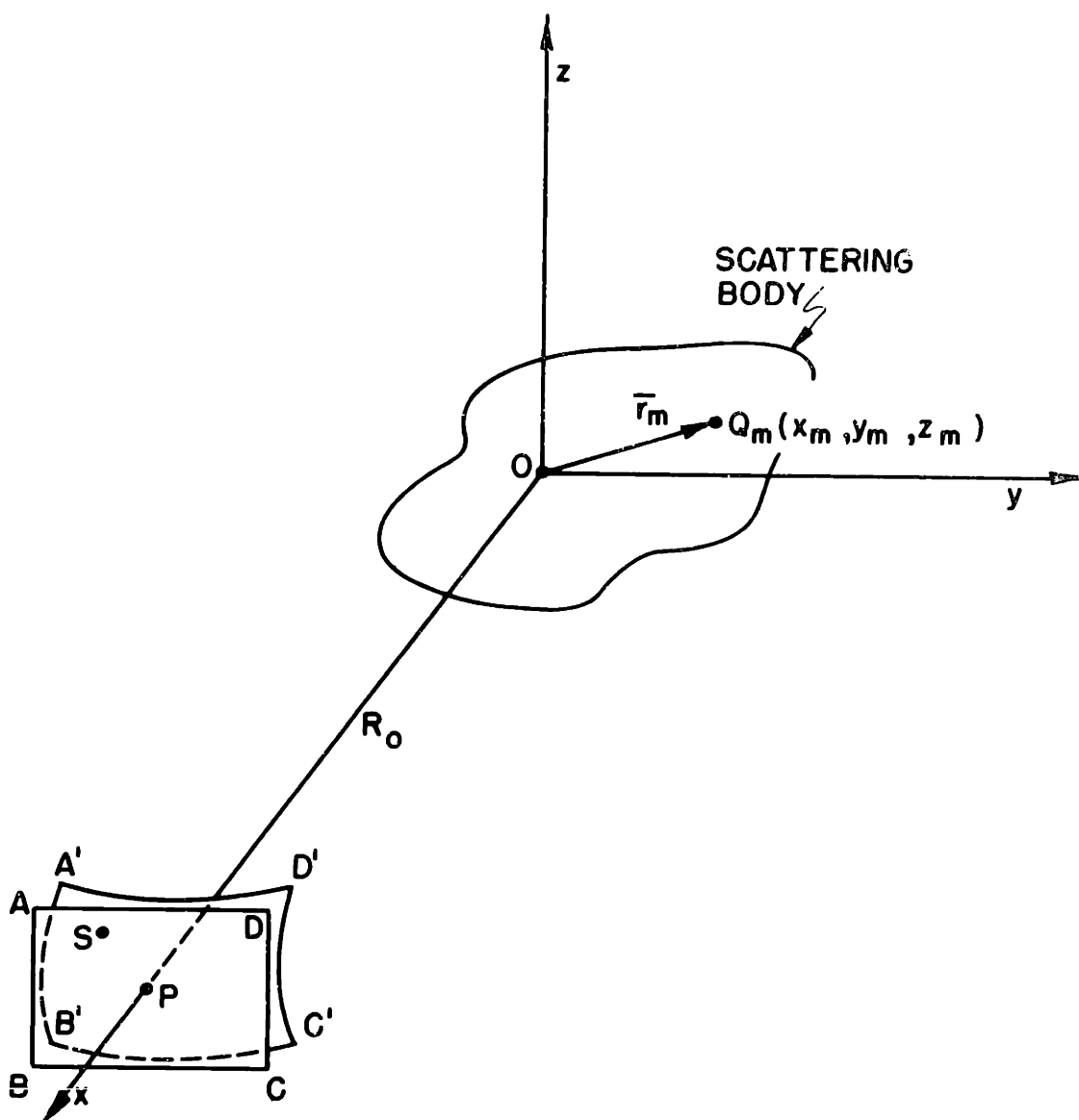


FIGURE 5

Geometry Relevant to a More Rigorous Treatment of the Fourier Transform Relation.

that  $\delta$  and  $\gamma$  are  $\ll 1$  radian, we obtain

$$(PQ_m + Q_m S) \approx [2R_0 - 2x_m - (y_m \delta + z_m \gamma)] \quad (5)$$

If expression (5) is substituted for the quantity  $2r_m$  in Eq. (1), the latter yields the field received at S, which we now denote by the symbol F:

$$F(\delta, \gamma) = \sum_{m=1}^M K_m \cdot e^{jk [2R_0 - 2x_m - (y_m \delta + z_m \gamma)]} \quad (6)$$

where M is the total number of highlight points. If we assume that the scattered field is measured instantaneously over the aperture, then all the quantities in (6) are independent of time even though the scatterer is moving. Thus the term  $e^{jk2R_0}$  represents a constant phase factor that may be omitted without loss of generality.

To make apparent the formal Fourier integral relation between the highlight distribution and the scattered field, we shall suppose temporarily that the highlights have a continuous volume density distribution rather than a discrete point character. This assumption will not jeopardize the final result because at some later point in the analysis we can allow the continuous distribution to approach a discrete distribution as closely as we like. Thus Eq. (6) becomes

$$F(\delta, \gamma) = \iiint_{-\infty}^{\infty} a(x, y, z) e^{-jk(2x + y\delta + z\gamma)} dx dy dz \quad (7)$$

where  $a(x, y, z)$  is the volume density distribution of sources. It is permissible to use infinite limits for the integration because  $a(x, y, z)$  is zero everywhere outside the volume occupied by the

scatterer.

Now we integrate (7) with respect to  $x$  and obtain

$$F(\delta, \gamma) = \iint_{-\infty}^{\infty} A(y, z) \cdot e^{-jk(y\delta + z\gamma)} dy dz \quad (8)$$

where

$$A(y, z) = \int_{-\infty}^{\infty} a(x, y, z) \cdot e^{-jk2x} dx \quad (9)$$

It is seen that (8) has the form of a two-dimensional Fourier transform, relating the complex aperture field  $F$  and the complex distribution function  $A(y, z)$ . The physical interpretation of (9) is that  $A$  represents the projection of the volume distribution of sources onto the  $yz$  plane, that is, onto the plane perpendicular to the direction of incidence.  $A(y, z)$  is complex because a phase factor,  $e^{-jk2x}$ , is associated with each element of the volume distribution of sources.

Strictly speaking, (8) cannot be inverted to yield  $A$  in terms of  $F$ , because the Fourier inverse requires integration over infinite ranges of  $\delta$  and  $\gamma$ , whereas (8) is valid only for values of  $\delta$  and  $\gamma \ll 1$ . However, by employing finite integration limits, we obtain formally an approximate inversion of (8):

$$A(y, z) \approx \frac{k^2}{4\pi^2} \int_{-V}^V d\delta \int_{-W}^W F(\delta, \gamma) \cdot e^{jk(y\delta + z\gamma)} d\gamma \quad (10)$$

A further modification to (8) and (10) is required. Note that the Fourier transform relation is not between the variable pairs  $(\delta, \gamma)$  and  $(y, z)$ , since the factor  $k (= 2\pi/\lambda)$  in the exponent of the integrand must be absorbed into one or the other of these pairs. We choose to associate  $k$  with  $(\delta, \gamma)$ , and accordingly

introduce the new variables  $\alpha = k \delta$ ,  $\beta = k \gamma$ . Equations (8) and (10) may now be rewritten in terms of  $(\alpha, \beta)$  and  $(y, z)$  as follows:

$$\bar{F}(\alpha, \beta) = \iint_{-\infty}^{\infty} A(y, z) \cdot e^{-j(y\alpha + z\beta)} dy dz \quad (11)$$

$$A(y, z) \approx \frac{1}{4\pi^2} \int_{-kV}^{kV} d\alpha \int_{-kW}^{kW} F(\alpha, \beta) \cdot e^{j(y\alpha + z\beta)} d\beta \quad (12)$$

where  $\bar{F}(\alpha, \beta) \equiv F(\delta, \gamma)$

Equations (11) and (12) represent the desired forms of the Fourier transform and its approximate inverse. We shall refer to these approximate relations that involve finite integration limits, such as (10) and (12), as "finite Fourier transforms".

The analysis given above shows that a source distribution cannot be uniquely determined from its distant scattered field because  $a(x, y, z)$  is not uniquely determinable from  $A(y, z)$ . That is, any number of functions  $a(x, y, z)$  can be found which will yield a given  $A(y, z)$  when substituted in the right-hand side of Eq. (9). This ambiguity is not serious in our situation, since we are concerned with determining a number of discrete highlight areas rather than a continuous volume distribution of sources. Considering the nature of aircraft geometry, it is impossible for two or more highlights to have the same  $x$  coordinate, hence none will be merged together by projection onto the  $yz$  plane. Therefore, the ambiguity results only in a loss of the  $x$  coordinates of the highlights; or, stated alternatively, the depth dimension of the highlight configuration is indeterminate.



[REDACTED]

By setting  $\gamma \equiv 0$  in the preceding analysis, we obtain the special case of a one-dimensional aperture, namely, the arc of the great circle through P, parallel to B'C', and terminating on A'B' and C'D', respectively (see Fig. 5). In this case Eq. (7) becomes

$$F(\delta) = \iiint_{-\infty}^{\infty} a(x,y,z) \cdot e^{-jk(2x + y\delta)} dx dy dz \quad (13)$$

Now if we integrate with respect to x and y, and at the same time replace  $k\delta$  by  $\alpha$ , we obtain

$$\bar{F}(\alpha) = \int_{-\infty}^{\infty} A(y) \cdot e^{-jy\alpha} dy \quad (14)$$

where

$$A(y) = \iint_{-\infty}^{\infty} a(x,y,z) \cdot e^{-jk2x} dx dz \quad (15)$$

and  $\bar{F}(\alpha) \equiv F(\delta)$

Equation (14) has the form of a one-dimensional Fourier transform relating  $\bar{F}(\alpha)$  and  $A(y)$ . The physical interpretation of (15) is that  $A(y)$  represents the projection of the highlight distribution onto the y axis; that is, onto a line parallel to the arc along which the scattered field is measured. The approximate inverse of (14) is

$$A(y) \approx \frac{1}{2\pi} \int_{-kV}^{kV} \bar{F}(\alpha) \cdot e^{jy\alpha} d\alpha \quad (16)$$

Equations (14) and (16) are the one-dimensional equivalents of (11) and (12). An additional degree of ambiguity has been introduced because the z coordinate of each highlight is now

[REDACTED]

unknown. Furthermore, all points with the same z coordinate will project into a single point on the y axis. However, it is expected that merging of highlight points in this manner will not occur in many situations. For example, a radar which is viewing a distant aircraft in level flight will lie near the plane of the aircraft wing. According to Fig. 5 the wing plane will then be nearly coincident with the xy plane. Since the shape of an aircraft is such that the highlight points are concentrated in the wing plane, it is unlikely that more than one point will lie on any line parallel to the z axis.

We now wish to show that the approximate equalities (12) and (16) can be made as exact as we please by simultaneously letting the aperture and the wavelength approach zero in such a way that their ratio approaches infinity. We shall derive this result for Eq. (16) only, since the same argument can be extended directly to (12). Also, we shall confine attention to a discrete source distribution, which is the case of practical interest. For a scatterer composed of M highlight points, Eq. (13) becomes

$$F(\delta) \equiv \bar{F}(\alpha) = \sum_{m=1}^M K_m \cdot e^{-j(y_m \alpha + \rho_m)} \quad (17)$$

where  $K_m$  and  $y_m$  are the amplitude and projected position of the mth highlight point and  $\rho_m = 2kx_m$ . We must take into account the phenomenon of highlight variation discussed in section 2.2. This is done by making  $K_m$ ,  $y_m$ , and  $\rho_m$  functions of  $\delta$ . If the angular aperture interval,  $2V$ , is made sufficiently small, these three functions can be represented by the first two terms

of their Taylor series expansions about  $\delta = 0$ . Thus

$$\begin{aligned} K_m(\delta) &\approx K_{m0} + K'_{m0} \delta \\ Y_m(\delta) &\approx Y_{m0} + Y'_{m0} \delta \\ \rho_m(\delta) &\approx \rho_{m0} + \rho'_{m0} \delta \end{aligned} \quad (18)$$

Here  $K_{m0}$  and  $K'_{m0}$  are abbreviations for  $K_m(0)$  and  $\left[ \frac{dK_m(\delta)}{d\delta} \right]_{\delta=0}$ , respectively; similar remarks apply to the remaining symbols.

Substituting Eq. (18) into Eq. (17), and then (17) into (16), we obtain

$$A(y) \approx \sum_{m=1}^M \frac{1}{2\pi} \int_{-kV}^{kV} (K_{m0} + K'_{m0} \delta) \cdot \exp \left\{ j \left[ (y - y_{m0} - Y'_{m0} \delta) \alpha - \rho_{m0} - \rho'_{m0} \delta \right] \right\} d\alpha \quad (19)$$

Now  $|\delta|$  is  $\leq V$  in the aperture; therefore by choosing  $V$  sufficiently small we can make  $|K'_{m0} \delta|$ ,  $|Y'_{m0} \delta|$  and  $|\rho'_{m0} \delta|$  as small as we like compared with  $K_{m0}$ ,  $y_{m0}$  and  $\rho_{m0}$ , respectively. Thus we can make the right-hand side of (19) approximate

$$\sum_{m=1}^M \frac{K_{m0}}{2\pi} \int_{-kV}^{kV} e^{j \left[ (y - y_{m0}) \alpha - \rho_{m0} \right]} d\alpha$$

as closely as we wish. Integration of the above expression yields

$$A(y) \approx \sum_{m=1}^M \left\{ \frac{K_{m0} e^{-j \rho_{m0}}}{\pi} \left[ \frac{\sin \left[ (y - y_{m0}) kV \right]}{(y - y_{m0})} \right] \right\} \quad (20)$$

If we now let  $\lambda$  and  $V$  approach zero in such a way that  $kV = 2\pi (V/\lambda)$  approaches infinity, Eq. (20) reduces to

$$\lim_{\substack{V, \lambda \rightarrow 0 \\ kV \rightarrow \infty}} [A(y)] = \sum_{m=1}^M K_{m0} \cdot u(y - y_{m0}) \cdot e^{-j\rho_{m0}} \quad (21)$$

where  $u$  is the unit impulse function.

In words, Eq. (21) states that, in the limit, the computed source distribution consists of  $M$  discrete sources, the  $m$ th source having amplitude  $K_{m0}$ , projected position  $Y_{m0}$ , and relative phase  $\rho_{m0}$ .

Thus we have shown that the projected highlight distribution can be evaluated as closely as desired by a Fourier transform of the scattered field over a finite aperture, by making both the aperture and the wavelength sufficiently small. The limiting situation corresponds to perfect resolution. Of course, we cannot reach this ideal, so it is desirable to determine the wavelength at which a satisfactory degree of resolution can be achieved. We shall take up this problem in Chapter 5, following the theory of conventional radars, so that a more unified treatment can be given.

#### 2.4 Highlight Information Derivable from the Amplitude of the Scattered Field

The analysis of section 2.3 prescribes that the Fourier transform operation is to be performed on the instantaneous scattered field distribution. It would be useful to know what can be deduced about the highlight configuration from the amplitude

(i.e., envelope) of the field only, since this is a much easier quantity to measure in practice. We shall first show that the finite Fourier transform of the square of the amplitude yields the space autocorrelation function of the projected highlight distribution. Then we shall discuss the conditions under which it is possible to derive the projected distribution from its autocorrelation function. A detailed study of the possibility of doing this is presented in Appendix B. The present analysis will be confined to a one-dimensional aperture, but its extension to two dimensions can be made without difficulty.

The amplitude of the one-dimensional field is given by  $|\bar{F}(\alpha)|$ . It is well known from time and frequency domain analysis that, if  $F(\omega)$  is the spectrum of a transient function  $f(t)$ , then  $|F(\omega)|^2$  is the spectrum of  $R(t')$ , where  $R(t')$  is the autocorrelation function of  $f(t)$ . The analogy can be carried over to the present situation, for we can interpret  $\bar{F}(\alpha)$  as the spectrum of  $A(y)$ , and therefore conclude that  $|\bar{F}(\alpha)|^2$  is the spectrum of  $R_A(y)$ , where  $R_A(y)$  is the autocorrelation of  $A(y)$ .\* To derive  $R_A(y)$  explicitly, we first take the square of the modulus of Eq. (17), obtaining

$$|\bar{F}(\alpha)|^2 = \sum_{m=1}^M \sum_{n=1}^M K_m K_n \cdot e^{-j[y_m \alpha + \rho_m]} \cdot e^{j[y_n \alpha + \rho_n]} \quad (22)$$

\* To be more precise, some symbol other than  $y$  should be used for the argument of the autocorrelation function, to distinguish it from the argument of the primitive function. No confusion should result, however.

$$|\bar{F}(\omega)|^2 = \sum_{m=1}^M K_m^2 + 2 \sum_{m=2}^M \sum_{\substack{n=1 \\ (m>n)}}^{M-1} K_m K_n \cos[(y_m - y_n)\omega + \rho_m - \rho_n] \quad (23)$$

The finite Fourier transform of (23) is

$$R_A(y) \approx \left\{ \begin{aligned} & \sum_{m=1}^M \frac{K_m^2}{2\pi} \int_{-kV}^{kV} e^{jy\omega} d\omega \\ & + \sum_{m=2}^M \sum_{\substack{n=1 \\ (m>n)}}^{M-1} \frac{K_m K_n}{\pi} \int_{-kV}^{kV} e^{jy\omega} \cos[(y_m - y_n)\omega + \rho_m - \rho_n] d\omega \end{aligned} \right\} \quad (24)$$

Upon integration and rearrangement, (24) reduces to

$$R_A(y) \approx \left\{ \begin{aligned} & \frac{\sin ykV}{\pi y} \sum_{m=1}^M K_m^2 \\ & + \sum_{m=2}^M \sum_{\substack{n=1 \\ (m>n)}}^{M-1} K_m K_n \left\{ \frac{\sin([y + (y_m - y_n)]kV)}{\pi[y + (y_m - y_n)]} \cdot e^{j(\rho_m - \rho_n)} \right. \\ & \quad \left. + \frac{\sin([y - (y_m - y_n)]kV)}{\pi[y - (y_m - y_n)]} \cdot e^{-j(\rho_m - \rho_n)} \right\} \end{aligned} \right\} \quad (25)$$

By proceeding to the limit as before, we obtain

$$\lim_{\substack{V, \lambda \rightarrow 0 \\ kV \rightarrow \infty}} [R_A(y)] = \left\{ \begin{aligned} & u(y) \cdot \sum_{m=1}^M K_m^2 \\ & + \sum_{\substack{m=2 \\ (m > n)}}^M \sum_{n=1}^{M-1} K_m K_n \left\{ u [ y + (y_m - y_n) ] \cdot \epsilon^{j(\rho_m - \rho_n)} \right. \\ & \left. + u [ y - (y_m - y_n) ] \cdot \epsilon^{-j(\rho_m - \rho_n)} \right\} \end{aligned} \right\} \quad (26)$$

The interpretation of (26) is that  $R_A(y)$  is composed of a sum of unit impulse functions, located at  $y = 0$  and at values of  $y$  corresponding to the differences between the projected positions of all pairs of highlight points. It is easy to verify that the result obtained in (26) agrees with that derivable from the familiar definition of an autocorrelation function in terms of its primitive function.

We now ask whether or not it is possible to determine the projected highlight distribution from its autocorrelation function. Essentially the problem reduces to determining the values of a set of numbers from the values of the differences between every pair of these numbers. To see this, first observe that in practice a radar system would not evaluate the complex quantities  $A(y)$  and  $R_A(y)$ , given by Eqs. (20) and (25), respectively, but might evaluate the moduli of these quantities. If we assume that the resolution is sufficiently good so that the  $(\sin x)/x$  functions in Eqs. (20) or (25) do not overlap appreciably, it can be shown that  $|A(y)|$  and  $|R_A(y)|$  are also given approximately by these equations if we merely omit the exponential factors. Since these

factors represent inconsequential phase terms, their loss is unimportant.

We note that  $|R_A(y)|$  is a symmetrical function with respect to  $y = 0$ ; thus its positive part contains all of the essential information. We shall denote it by  $|R_A(y)|_+$ , where

$$|R_A(y)|_+ \approx \sum_{m=2}^M \sum_{n=1}^{M-1} \frac{K_m K_n}{\pi} \frac{\sin [(y - (y_m - y_n)) kV]}{[y - (y_m - y_n)]} \quad (27)$$

( $m > n$ )

Dropping the zero subscripts in (20), for uniformity, we have

$$|A(y)| \approx \sum_{m=1}^M \frac{K_m}{\pi} \frac{\sin [(y - y_m) kV]}{(y - y_m)} \quad (28)$$

Equations (27) and (28) represent two sets of  $(\sin x)/x$  functions, and it is assumed that there is inappreciable overlap between adjacent functions in each set. Thus from plots of  $|R_A(y)|_+$  and  $|A(y)|$  we can determine the amplitude and the abscissa of the peak of each  $(\sin x)/x$  function. This yields two sets of number pairs

$\{K_m K_n ; (y_m - y_n)\}$  and  $\{K_m ; y_m\}$ , which we shall denote by  $\{a\}$  and  $\{b\}$ , respectively.

The problem of determining  $|A(y)|$  from  $|R_A(y)|_+$  is therefore equivalent to deriving set  $\{b\}$  from set  $\{a\}$ . Obviously the quantities  $y_m$  can be determined only to within an additive constant because only differences between pairs of these quantities are given. However, the additive constant is not



[REDACTED]

important since the  $y$  s represent projected distances from an arbitrary origin whose location is inconsequential. Thus we may choose one of the  $y$  s to be zero and evaluate the remaining ones in terms of it.

The derivation of  $\{b\}$  from  $\{a\}$  appears trivial at first sight, but is not so if we recognize that the identifying subscripts  $m$  and  $n$  which are associated with each number in set  $\{a\}$  are not present in practice. They could be specified in the preceding analysis because  $R_A(y)$  was derived from an assumed known  $A(y)$ , whereas in the present situation  $A(y)$  is the unknown to be evaluated from its autocorrelation. The solution of this problem is considered fully in Appendix B. It is concluded there that, provided all the quantities  $(y_m - y_n)$  are unequal,  $|A(y)|$  can be determined uniquely from  $|R_A(y)|_+$ , except for an indeterminacy in the sense of the derived set  $\{y_m\}$ . A graphical method for obtaining the solution is given in Appendix B. It is further conjectured that a unique solution also exists when not more than two of the quantities  $(y_m - y_n)$  are equal.

The possibility of determining the primitive function uniquely from its autocorrelation depends on having all, or nearly all, of the differences  $(y_m - y_n)$  unequal. This situation is most likely to occur when there are few highlights present (say four or less), and when these are distributed in an asymmetrical manner on the aircraft surface. It is believed that the distributions will generally be asymmetric for aircraft aspects in the vicinity of broadside. For head-on views, on the contrary, the highlights are likely to be symmetrically arranged about the center line of the aircraft, with the result that a number of the differences will be

[REDACTED]

[REDACTED]

equal. However, if it is known that a head-on aspect is being presented, this information may materially assist in estimating correctly the highlight distribution from its autocorrelation. It is therefore concluded that in many circumstances the autocorrelation of the one-dimensional projection of the highlight configuration will yield nearly as much information concerning the aircraft geometry as does the projected distribution itself. This fact is important, since the design of a radar for determining the autocorrelation is much simpler than that of a radar which evaluates the distribution directly. The practical design problems of both types of radars are dealt with in the next chapter.

[REDACTED]

[REDACTED]

CHAPTER 3

DESIGN AND PERFORMANCE OF MULTIRECEIVER RADARS

We now wish to apply the theory of Chapter 2 to the problem of designing radars which can measure respectively the projected highlight configuration and its autocorrelation function. In addition we shall consider the capabilities of such radars for counting aircraft in a formation, and for yielding information concerning random motion of the aircraft, and the character of propeller rotation and significant flexural vibrations. The design study will show that a radar for computing highlight distributions directly appears unfeasible at present, due to the requirement of accurately measuring the phase of the scattered field. However a radar which computes the autocorrelation function appears practicable. The possibility of counting aircraft in formation is also found to be good when the individual aircraft are separated in azimuth. The possibility of detecting random aircraft motion, propeller rotation and vibrations depends on the extent to which these movements produce observable changes in the sequence of instantaneous highlight configurations.

3.1 Design of a Radar to Compute Highlight Distributions Directly.

It was briefly mentioned at the end of Chapter 1 that a radar for computing highlight distributions would consist of a transmitter, a matrix of receiving elements occupying an aperture of adequate size, and a Fourier transform computer. The transmitter is assumed to be located at the center of the receiving aperture. The main design parameters which must be specified are: size and shape of

[REDACTED]

aperture, number and distribution of receiving elements, radar wavelength, tolerances in receiver locations, amplitude and phase stability of the receivers, and the nature of the Fourier transform computer. We shall consider these requirements only far enough to determine whether such a system appears feasible. A representative operational situation will be specified in order to arrive at numerical values for the design parameters.

Suppose it is desired to resolve highlights whose projected spacing is  $\geq d_{\min}$  feet, when the aircraft is R feet from the radar. Then  $d_{\min}$  subtends angle  $\delta = \left(\frac{d_{\min}}{R}\right)$  radians at the radar, and the Rayleigh criterion of resolution states that  $\delta = \frac{\lambda}{D}$ , where D is the aperture dimension. One more relation is needed to determine both  $\lambda$  and D, and it is provided by the requirement that D be small enough to make highlight variations over the aperture (a phenomenon discussed in section 2.2) inappreciable. Determination of the maximum permissible value of D for this purpose is difficult, and is discussed further in Chapter 5. Suppose the aperture must not subtend an angle greater than  $\Delta$  radians at the aircraft to satisfy this condition. Then we have the second relation:  $D = R \Delta$  which determines D, and  $\lambda$  is then found from the Rayleigh criterion. For instance if we choose the values:  $d_{\min} = 3$  feet,  $R = 12$  miles,  $\Delta = \frac{1}{4}$  degree =  $\frac{1}{229}$  radian, we obtain:  $D = \left(\frac{12 \times 5280}{229}\right) \approx 280$  feet. Thus from the Rayleigh criterion,  $\lambda = (280) \left(\frac{3}{12 \times 5280}\right) = 0.0132$  feet, or 0.4 centimeters.

The number of receiving elements in the array must be sufficient to provide an adequate sampling of the instantaneous received field, so that the entire field over the aperture can

be reconstructed from its values at the sampling points. Referring to section 2.1, the received field is seen to consist essentially of a sum of sinusoids, the space wavelength of each being determined by the incident angle of energy arriving from the associated highlight point. The smallest angle of incidence which we must design for is equal to the angle subtended between two highlights which are just resolvable, namely  $\delta$ . In section 2.1 it was shown that the corresponding space wavelength is  $\frac{\lambda}{\delta}$ , which is equal to the aperture diameter prescribed by the Rayleigh criterion for resolving power  $\delta$ .

Now suppose the axis of the radar array is pointed toward one edge of the aircraft, so that the angle between the nearest highlight to this edge and the axis is  $\delta$ . Then the highlight nearest the opposite edge subtends the largest angle of incidence and therefore generates the shortest space wavelength across the aperture. If the projected distance between the two outermost highlights is  $d_{\max}$ , then the shortest space wavelength present in the aperture is  $(\frac{d_{\min}}{d_{\max} + d_{\min}}) D$ ,  $\approx (\frac{d_{\min}}{d_{\max}}) D$ , and the number of these wavelengths across the aperture is  $\approx (\frac{d_{\max}}{d_{\min}})$ . The sampling theory of frequency limited functions tells us that the sampling points must be spaced not more than half the minimum space wavelength apart, hence there must be at least  $2(\frac{d_{\max}}{d_{\min}})$  receivers across one dimension of the aperture. If in the present example we let  $d_{\max} = 100$  feet, then  $2(\frac{100}{3}) = 67$  receivers are required across one side. The receiver separation is therefore  $\frac{280}{67} = 4$  feet.

A point of interest is that the required number of receivers depends only on the ratio  $(\frac{d_{\max}}{d_{\min}})$  and is therefore independent of aircraft distance R. Also, the receiver separation required to

resolve two points of fixed spacing  $d_{\min}$  is directly proportional to R. This suggests that an array with a fixed number of receivers, whose spacing can be varied in proportion to R, would be desirable since it would maintain a prescribed resolution  $d_{\min}$  independent of aircraft distance. Variable receiver spacing will also be found useful for counting aircraft in a formation.

We are now ready to discuss some of the practical difficulties in the design of a multireceiver system. First, to obtain a planar projection of the highlight distribution we need a two-dimensional aperture whose dimension may be of the order of hundreds of feet per side. A vertical dimension of this magnitude would be unwieldy if not prohibitive, and in addition a square matrix would require  $(67)^2 = 4500$  receivers in the example considered. We assume that it is impractical to meet these requirements, and therefore shall confine attention to a horizontal, one-dimensional aperture.

Secondly, each receiver must be capable of measuring the instantaneous value of the received field strength. This is equivalent to saying that it must measure both the amplitude and phase of the received signal. The accuracy of the phase\* measurement should be of the order of  $\frac{2\pi}{100}$  radians. Such accuracy places stringent design requirements on the linearity and phase stability of the receiver amplifiers. In addition it requires that each receiving antenna cannot be permitted to undergo

-----  
\* This is a relative phase measurement, one receiver in the array being chosen to provide a phase reference.

displacements greater than  $\frac{\lambda}{100}$  parallel to the axis of the array. At a wavelength of 0.4 centimeters this corresponds to a displacement of  $\frac{1.6}{1000}$  inches. When one considers that the array extends for hundreds of feet, the difficulties involved in obtaining the necessary structural rigidity appear formidable.

A third difficulty is that the receivers are required to lie on the arc of a circle of radius R rather than on a straight line. The reason for this is best seen by referring to Eq. (5), which expresses the length of the two way path from the transmitter P to a receiver S. This expression is based on the assumption that S lies on the surface of a sphere of radius R. If instead, S were in the tangent plane to the spherical surface at P, then the correct expression, to the first order of small quantities, would be:

$$(PQ_m + Q_m S) \approx \left[ 2R - 2x_m - (y_m \delta + z_m \gamma) + \frac{R}{2} (\delta^2 + \gamma^2) \right] \quad (29)$$

For typical parameter values it is found that the additional term,  $\frac{R}{2} (\delta^2 + \gamma^2)$ , is at least of the same order of magnitude as  $(y_m \delta + z_m \gamma)$ . But the presence of the additional term destroys the Fourier transform relation between the scattered field and the source distribution, since the kernel of the Fourier integral involves  $\delta$  and  $\gamma$  only through the linear form  $(y_m \delta + z_m \gamma)$ . One problem arising from the requirement to locate the receivers on a circular arc is that the radius of the arc changes continuously as the aircraft moves radially. It therefore appears that the receivers must be movable parallel to the array axis, so as to conform to the changing arc.

A final problem is the necessity of making the whole array

[REDACTED]

trainable, to accurately track the aircraft in azimuth. It is evident from previous discussion that if the array axis wanders off the aircraft appreciably, the space wavelengths comprising the field across the aperture will become very short, with the result that the conditions required to validate the sampling theorem are destroyed. On the other hand the array axis must not be allowed to fall between highlight points because, referring to Fig. 3 of section 2.1, there is an ambiguity in determining on which side of the axis the highlights lie. Thus a pair of highlights subtending equal angles of incidence on either side of the axis cannot be distinguished since they produce the same space wavelength in the aperture. This ambiguity can be avoided by having the radar point at one edge of the aircraft, so that all the highlights lie on the same side of the axis. This requirement, coupled with that of not pointing too far off the aircraft, means that tracking must be controlled to very close tolerances, preferably to within  $\pm 1/4$  of the azimuthal angle subtended by the aircraft at the radar. Even with this tracking accuracy it would be necessary to use approximately 50 percent more receivers than was estimated in the preceding example, in order not to violate the sampling condition.

The possibility of tracking with the above precision by physically training such a large array appears questionable, so it might be necessary to achieve steerability electronically, by the insertion of continuously variable phase shifters in each receiver. Simultaneously, the receivers could effectively be positioned on an arc of changing radius by the injection of

[REDACTED]



[REDACTED]

additional phase shifts. The total injected phase shift would be such that the array appeared to conform to a circular arc of appropriate radius and pointing direction at all times. The above discussion indicates that the requirement for precise phase measurement and phase control in the receivers, coupled with close mechanical tolerances in receiver positions will result in an extremely complex and costly equipment, assuming that the requirements can be met by present day techniques. The author's opinion is that the design problems are too formidable to render such a system feasible at present.

We have yet to discuss the design of the Fourier transform computer which operates on the receiver outputs. This will not be gone into in detail; only the operations which the computer has to perform will be outlined, since the realization of the computer appears considerably simpler than the remainder of the system. It was mentioned in section 2.4 that the modulus  $|A(y)|$  of the complex projected distribution would be a desirable function to evaluate in practice. It is obtained by taking the square root of the sum of the squares of the real and imaginary parts of  $A(y)$ . The relations between the latter quantities and the real and imaginary parts of  $\bar{F}(\alpha)$  are easily obtained if  $\bar{F}(\alpha)$  is first written in polar form:

$$\bar{F}(\alpha) = |\bar{F}(\alpha)| \cdot e^{j\varphi(\alpha)} \quad (30)$$

On substituting expression (30) into equation (16) and taking the real part of both sides, we obtain:

$$\begin{aligned} \text{Re} [A(y)] &\approx \frac{1}{2\pi} \int_{-kV}^{kV} |\bar{F}(\alpha)| \cos(y\alpha + \varphi(\alpha)) d\alpha \\ &\approx \left\{ \begin{aligned} &\frac{1}{2\pi} \int_{-kV}^{kV} \text{Re} [\bar{F}(\alpha)] \cdot \cos y\alpha d\alpha \\ &- \frac{1}{2\pi} \int_{-kV}^{kV} \text{Im} [\bar{F}(\alpha)] \cdot \sin y\alpha d\alpha \end{aligned} \right\} \quad (31) \end{aligned}$$

Equation (31) states that  $\text{Re} [A(y)]$  is the difference of the Fourier cosine transform of  $\text{Re} [\bar{F}(\alpha)]$  and the Fourier sine transform of  $\text{Im} [\bar{F}(\alpha)]$ . Similarly it can be shown that

$\text{Im} [A(y)]$  is the sum of the Fourier sine transform of  $\text{Re} [\bar{F}(\alpha)]$  and the Fourier cosine transform of  $\text{Im} [\bar{F}(\alpha)]$ .

It is therefore necessary to generate the Fourier cosine and sine transforms of both the real and imaginary parts of  $\bar{F}(\alpha)$ . To generate the latter functions we must establish a phase reference, since the phase of the scattered field is known only to an arbitrary additive constant. Suppose the i-f output signal from the receiver located at P, Fig. 5, is selected as this reference. Then it is possible to generate the desired real and imaginary parts of  $\bar{F}$  by applying simultaneously the i-f outputs from receivers located at P and at a variable point S, to two separate phase sensitive detecting circuits. The details of performing these operations are not sufficiently relevant to warrant inclusion here. In summary, it is evident that a fairly complex computing operation is required to determine the projected highlight distribution, since it necessitates the evaluation of four Fourier integral

transforms. However the operations involved appear to be realizable with fairly conventional circuits.

### 3.2 Design of a Radar to Compute the Autocorrelation of Highlight Distributions.

The design requirements for a radar which computes the autocorrelation of the projected distribution are much less stringent than those discussed in the preceding section, primarily because the need to measure phase is dispensed with. As a result the tolerance in positioning receivers is greatly relaxed, also it is no longer necessary to have the radar accurately track the aircraft. Finally, the Fourier transform computer is required to evaluate only two functions instead of four.

The following parameters are not appreciably changed however: wavelength, aperture dimension, and number of receivers in the array. This is because we still wish to obtain the same highlight resolution as before, for the same aircraft distances. Also the phenomenon of highlight variation with aspect is unchanged, therefore the aperture dimension  $D$  is evaluated on the same basis as previously. Closer study indicates that somewhat better highlight resolution may be desired in the present situation, because the autocorrelation function is comprised of differences between pairs of projected highlight positions, and it is possible for the difference between two such differences to be less than  $d_{\min}$ . This possibility is not likely to occur frequently since the number of highlight points is generally small, particularly at broadside aspects. Of course at headon aspects one can have equality of two or more differences

due to symmetry, but in this case no degree of resolution will separate them. We shall therefore assume the same resolution requirement as before, and consequently the same value for  $\left(\frac{d_{\max}}{d_{\min}}\right)$ , which determines the number of receivers. As previously we assume that only a one-dimensional array is practicable.

It is readily seen that the receivers need not now be positioned accurately with regard to motion parallel to the array axis, because only the amplitude of the received field is being measured, and this does not change significantly over several feet in the direction of the aircraft. Thus it is not necessary for the receivers to conform to a circular arc, a straight line array being satisfactory. This conclusion can be verified quantitatively by writing down the expression for  $F(\delta)$  when the receivers are on a straight line, which, from Eqs. (29) and (17) is seen to be:

$$F(\delta) = \left( e^{-jk \frac{1}{2} R \delta^2} \right) \cdot \sum_{m=1}^M K_m e^{-j(y_m k \delta + \rho_m)} \quad (32)$$

The amplitude of the received field is obtained from  $|F(\delta)|^2$ , and the latter is derived by multiplying the right hand side of Eq. (32) by its conjugate complex mate. This operation replaces the factor outside the summation sign by unity, and the resulting expression is therefore the same as that for the receivers on a circular arc.

Receiver positioning parallel to the line of receivers is not exacting either, as long as movements are confined to a

small fraction (say  $\frac{1}{50}$  th) of the inter-receiver spacing. Since the latter was 4 feet in the example of section 3.1, a movement of  $\pm 1$  inch in this direction would be permissible, and this accuracy could be maintained over the length of the array without difficulty.

Finally, close tracking of the aircraft is no longer necessary, because the autocorrelation function is composed only of differences between projected highlight positions and is independent of absolute displacements. Thus it is independent of the pointing direction of the array axis, to within limits specified below, since the pointing direction determines the absolute projected positions of the highlights. Also there is no need to include additional receivers in the array to allow for aimoff, as was necessary in the phase measuring radar, again because we are not concerned with absolute projected positions.

It will be seen that the array axis can be pointed away from the aircraft by as much as 30 degrees without affecting the radar performance appreciably. This is because the amplitude (i.e., envelope) of each receiver output is essentially equal to that which would be measured if the receiver were projected onto a line perpendicular to the direction of the aircraft. Thus if the angle between the array axis and the aircraft is  $x$ , the receiver spacing is effectively diminished by the factor  $\cos x$ , and resolution is similarly reduced. Since  $\cos x$  has decreased to only 0.87 when  $x = 30$  degrees, the loss in resolution for this amount of aimoff is not great.

The only stringent design requirement to be met is that all the receivers have a high degree of amplitude linearity, otherwise

the measured pattern shape will be distorted. A means for rapid comparative calibration of receivers is also necessary unless gain stabilities are of a high order. The same standard of amplitude performance is of course required of the phase measuring radar as well. It is believed that the amplitude requirement is within present day equipment capabilities.

Finally it is noted that the Fourier transform computer need perform only two integral transformations in the present case. Specifically, we wish to compute  $|R_A(y)|$ , whose useful portion is  $|R_A(y)|_+$  (see Eq. (27), section 2.4). The procedure is to form the square root of the sum of the squares of the real and imaginary parts of  $R_A(y)$ , and it can be shown in a straightforward manner that  $\text{Re} [R_A(y)]$  is the Fourier cosine transform of  $|\bar{F}(\alpha)|^2$ , while  $\text{Im} [R_A(y)]$  is the Fourier sine transform of  $|\bar{F}(\alpha)|^2$ .

We therefore conclude that a multireceiver radar for measuring the autocorrelation is practicable, despite the necessity of using a long array. While a trainable array is desirable, a fixed array can produce useful results for targets within  $\pm 30$  degrees of the array axis. Also, the use of variable receiver spacing to maintain a fixed resolution  $d_{\min}$  despite change in aircraft distance appears feasible in this system, due to the relaxed requirements on accurate receiver positioning. In the next section it will be shown that variable receiver spacing is particularly useful for the purpose of counting aircraft in a formation.

### 3.3 Possibility of Counting Aircraft in a Formation.

Obviously the preceding techniques for determining projected

highlight distributions are applicable to several aircraft in formation as well as to individual aircraft. If the aircraft are sufficiently separated in azimuthal angle, each would be distinguishable as a separate group of highlight points and it will be easy to count the number present. However, if the aircraft are in a radial line, or are arrayed vertically, their highlight points will tend to merge and counting will become difficult\*. To fulfill the counting application most satisfactorily, it would be desirable to make the receiver spacing variable, to permit the resolving power of the radar to be adjusted in an optimum manner to various degrees of spread of the viewed formation.

For example, suppose the formation is a loose one, so that there is appreciable azimuthal separation between individual aircraft. This implies a large spread of highlights, resulting in short space wavelengths in the receiving aperture. Hence we shall require a small receiver spacing in order to satisfy the conditions of the sampling theorem. At the same time, the resolution requirement will be relaxed because our objective is merely to count the number of aircraft and not to distinguish highlight points on the individual aircraft. Obviously only enough resolution will be required to make each aircraft appear as a resolvable point. For both reasons therefore, we wish to reduce the spread of the receiving array.

---

\* We are assuming a horizontal one-dimensional array in this discussion.

[REDACTED]

Conversely, if the aircraft are in tight formation, so that there is overlapping of the highlight points of individual aircraft, it will be possible to increase the receiver spacing because the maximum space wavelength in the aperture is reduced. At the same time we shall want to resolve highlight points on the individual aircraft, since this should assist in estimating numbers when overlap occurs. Thus we wish to increase the array length in order to improve resolution.

To summarize, when counting aircraft at a given distance, the requirement is to contract the array when the formation is spread out (in azimuth) and expand it when the formation is tight. Thus we conclude that the facility of variable receiver spacing is useful for both the applications of resolving highlights on individual aircraft and for counting numbers when several aircraft are present.

#### 3.4 Detection of Random Motion, Vibrations, and Propeller Rotation.

The possibility of detecting random motion of an aircraft in flight, as well as flexural vibrations and propeller rotation, arises from the fact that a continuous sequence of projected highlight distributions can be generated and presented for visual inspection. Since an instantaneous highlight distribution can be computed for every received radar pulse, the number of distributions computable per second can equal the pulse repetition frequency of the radar, which may be of the order of 500 to 1000 pulses per second.

The three types of motion under discussion will be observable in the sequence of highlight distributions insofar as they produce

[REDACTED]



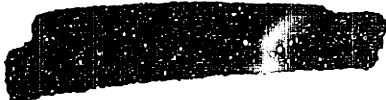
[REDACTED]

observable changes in either the reflected amplitudes or positions of the highlights. Normally, none of the motions are likely to cause highlight positions to change by more than two or three feet, so this movement may be discernible only occasionally since we have assumed that resolution will not be better than about three feet. However they may cause appreciable changes in highlight amplitudes. Propeller rotation is likely to show up best in this regard, particularly for headon views, because highlights located on engine nacelles or leading wing edges will be periodically blanked out as the propeller blades pass in front of them. If this effect is pronounced it will permit the estimation of blade frequency as well as the number of propellers.


The most pronounced random motion of an aircraft is roll, whose peak-to-peak amplitude may be 5 to 10 degrees in some aircraft types. It will be seen from the experimental results of Chapter 7 that aspect changes of this magnitude usually result in marked changes in highlight amplitudes, and so should be detectable. For most aircraft however the rms values of aspect change due to random motion are of the order of one degree or less, so we would expect to detect these motions only when atmospheric turbulence is appreciable.

Flexural vibrations are usually of small amplitude, and are not expected to be detectable in general. However, there are some aircraft types, such as the B-47, in which wing flexure can result in wing tip displacements of several feet, and so produce observable variations. Unusual characteristics such as this should therefore assist in identifying some aircraft types.

[REDACTED]






In the following two chapters, which treat the theory of highlight resolution with conventional radars, we shall see that the types of motion discussed here are more likely to be detectable in the conventional case, because angular rate of change of aspect is then a major factor in determining the shape of the computed highlight distribution. Therefore rapid motions such as vibrations and propeller rotation, which impart large rates of aspect change to some highlights, may be expected to produce clearly observable effects.

  
CHAPTER 4THE PARTIAL DETERMINATION OF HIGHLIGHT DISTRIBUTIONS BY  
CONVENTIONAL RADARS

The purpose of this chapter is to study the possibilities of determining highlight configurations with a conventional radar. By this we mean a radar consisting of a single receiver coincident in location with its transmitter. It will be shown that the received signal and the scattering sources are again related approximately by a Fourier transform. However, due to the limited capabilities of the conventional radar as compared to a multireceiver radar, it cannot determine the projected highlight distribution unambiguously. The main limitation is that it is able to measure the scattered field at only one point at any given instant, in contrast to the multireceiver system which measures the field over a finite angular interval instantaneously. For the conventional radar to obtain measurements over an angular interval, the aircraft must change aspect relative to it. Alternatively the radar may move around the aircraft, but this is not the usual situation and we shall assume in what follows that only the aircraft moves.

Thus an ambiguity arises, because the sequence of aspects presented by the aircraft is not precisely known. Stated in another way, the conventional radar measures the scattered field as a function of time, and the relation between time and aircraft aspect is unknown. Therefore at best, only a "relative" projected distribution is obtainable and the absolute projected spacing of the highlights remains unknown. With the conventional radar





only a one-dimensional projection can be determined, and the direction of projection changes continuously since it depends on the instantaneous angular velocity of the aircraft. Flexural vibrations of the aircraft may drastically reduce the ability to resolve highlight points, and may even distort the computed highlight distribution beyond recognition. In contrast, vibrations neither affect resolution nor introduce distortion in a multireceiver system, because the latter determines the distribution from an instantaneous spatial measurement, so that the aircraft is effectively frozen in position during the measurement.

To make the above statements more precise and meaningful, we need to study the kinematics of aircraft motion, and this is done in section 4.1. In section 4.2 the approximate Fourier transform is derived; it is a "short-time" transform rather than a finite space transform. Next, practical problems in evaluating the relative projected distribution are discussed. In the concluding section the possibilities of counting aircraft, and of detecting random motions, vibrations and propeller rotation, are considered.

#### 4.1 The Kinematics of Aircraft Motion Pertinent to Conventional Radar Measurements.

The kinematical framework will be made sufficiently broad to take into account flexural vibrations. Although this materially complicates the analysis, it appears necessary to include vibration effects because the spread of the computed highlight distribution is proportional to the rate of change of aircraft aspect. Aircraft

[REDACTED]

surfaces which vibrate rapidly, even though the vibration amplitude is not large, may impart significant rates of aspect change to their associated highlights. This results in both smearing of the highlights and their displacement relative to one another, with a consequent deterioration of the computed configuration.

The motion of an aircraft in flight is a combination of the following factors: (a) purposeful flight maneuvers; (b) random yaw, roll and pitch; (c) non-rigid vibrations. For the purpose of analyzing highlight point behavior, it is more useful to consider the motion to be composed of the following two components, as is customarily done in kinematical studies.

(1) A pure translational motion, specified by the trajectory of the center of gravity.

(2) A rotational motion about the center of gravity.

Component (1) may be divided into two subcomponents:

(1.1) The component parallel to the line joining the radar and the scatterer, commonly called the radial component.

(1.2) The component perpendicular to (1.1), commonly called the transverse component.

Components (1.2) and (2) produce variation of the aircraft aspect relative to the radar, whereas component (1.1) does not. Since aspect change is necessary in order for the receiver to record a finite portion of the scattered pattern, components (1.2) and (2) are of primary interest to us. Component (1.1) is of secondary interest, as it determines only the doppler frequency of the returned signal.

In kinematical studies of rigid body motion, component (2)

[REDACTED]

is specified by a single angular velocity vector. In our case we must account for change of aspect caused by component (1.2) as well. Therefore we shall specify an angular velocity vector,

$\bar{w}_r$ , which is not the usual one of kinematics but also accounts for aspect changes produced by (1.2). In addition, we must take into account the effects of non-rigid vibrations. Since these may cause different parts of the aircraft frame to be displaced in different directions, an additional set of angular velocity vectors must be specified, one corresponding to each part of the aircraft which generates a highlight point. Let  $\bar{w}'_m$  be the vector which accounts for the flexural motion of the  $m$ th highlight. The total rotational motion of this point relative to the radar is therefore completely specified by a vector  $\bar{w}_m = (\bar{w}_r + \bar{w}'_m)$ .

Figure 6, which is not to scale, illustrates the geometry pertinent to the problem. The rectangular coordinate system  $Oxyz$  is fixed relative to the scatterer\*, whose center of gravity is  $O$ . Let  $\bar{r}_m$  be the position vector of the  $m$ th highlight point  $Q_m$ . Let the rectangular components of  $\bar{w}_m$  be  $(w_{mx}, w_{my}, w_{mz})$ , and let  $\bar{a}_1$  be the unit vector along the  $x$  axis.

To simplify the discussion, assume temporarily that  $O$  is fixed in space. This implies that the aircraft has zero translational velocity, and merely rotates about its center of gravity. Since relative motion only is significant, let us now interpret

-----

\* Note that this differs from the coordinate frame in Fig. 5, where the axes were not fixed either with respect to the scatterer or the ground.

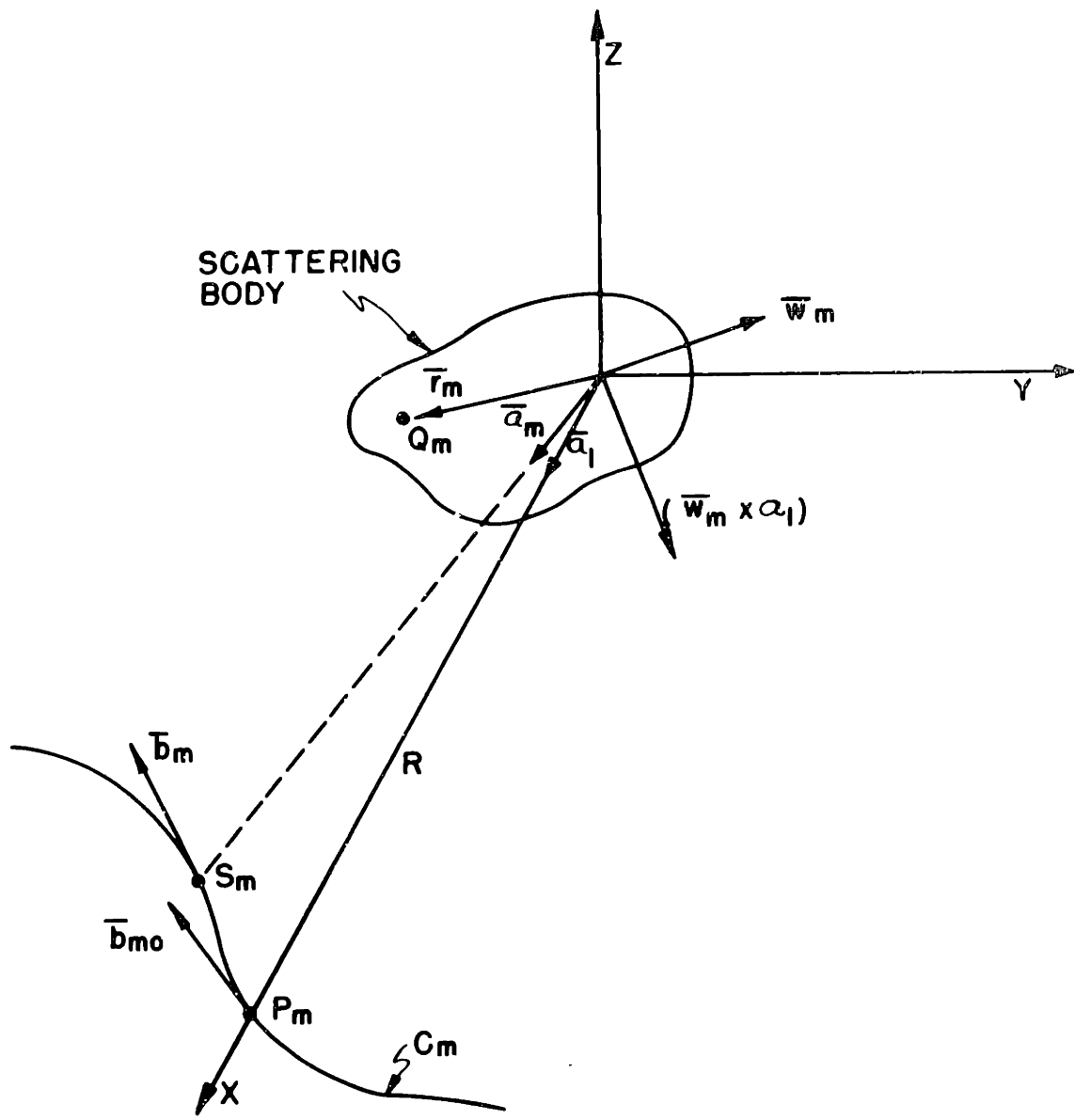


FIGURE 6

Geometry Pertaining to the Equivalent Trajectory  
of a Conventional Radar.

[REDACTED]

the aircraft rotation as an equivalent motion of the radar while the aircraft remains stationary. With this interpretation, the radar appears to move along a curve on a spherical surface of radius  $R$  and center  $O$ . Strictly speaking, the equivalent radar trajectory is not a single curve but a set of curves, one corresponding to each angular velocity vector  $\bar{\omega}_m$ . These paths all oscillate about a mean path, namely that corresponding to  $\bar{\omega}_r$ , which is the hypothetical path travelled by the radar if non-rigid vibrations were entirely absent. Let  $C_m$  denote the curve corresponding to  $\bar{\omega}_m$ , and let  $S_m$  be the position of the radar on this curve at time  $t$ . Let  $P_m$  be the position at time  $t = 0$ . We shall suppose, without loss of generality, that the  $x$  axis of the coordinate system passes through  $P_m^*$ . Finally, let  $\bar{b}_m$  be the unit vector tangent to  $C_m$  at point  $S_m$ , and let  $\bar{a}_m$  be the unit vector along  $OS_m$ . From the laws of kinematics it follows that the vector velocity of  $S_m$  is:

$$\bar{v}_m = - (\bar{\omega}_m \times \overline{OS}_m) = - R (\bar{\omega}_m \times \bar{a}_m)$$

Since  $\bar{v}_m$  is tangent to  $C_m$ , it is parallel to  $\bar{b}_m$ , so we may write alternatively:

$$\bar{v}_m = - R \left| \bar{\omega}_m \times \bar{a}_m \right| \bar{b}_m = - R \dot{\theta}_m \bar{b}_m \quad (33)$$

where  $\dot{\theta}_m = \left| \bar{\omega}_m \times \bar{a}_m \right|$ , is the angular rate of rotation of the line  $OS_m$  about  $O$ . Thus  $\dot{\theta}_m$  is seen to be the instantaneous rate of change of aspect of the  $m$  th highlight surface relative

-----

\* It is implied here that  $M$  different coordinate systems are used, one for each highlight surface; and the  $x$  axis of the  $m$  th coordinate system passes through  $P_m$ . The center of gravity of the aircraft is common to all  $M$  systems.



to the radar.

Next it is necessary to evaluate the path length traversed by the radar signal returned from  $Q_m$  at time  $t$ , namely  $2 S_m Q_m$ . By expanding the exact expression for length  $S_m Q_m$  in a series and retaining only the first order terms, we obtain:

$$S_m Q_m = [ R - x_m - (y_m \delta_m + z_m \gamma_m) ] \quad (34)$$

where  $R = OS_m$ , and  $\delta_m$  and  $\gamma_m$  are the angles which  $OS_m$  makes with the  $xz$  and  $yz$  planes respectively. In deriving Eq. (34) it is assumed that  $\delta_m$  and  $\gamma_m$  are  $\ll 1$  radian. Because of highlight variation with aspect, as discussed in section 2.2,  $x_m$ ,  $y_m$  and  $z_m$  are functions of  $\delta_m$  and  $\gamma_m$ , which in turn are functions of  $t$ . The restriction that  $R$  is constant is now removed, so that  $R$  is also a function of  $t$ . For small values of  $t$  we may expand (34) in a Taylor series about  $t = 0$ , and retain the first few terms only. The result is:

$$S_m Q_m \approx (p_{m0} + p_{m1} t + p_{m2} \frac{t^2}{2} + \dots) \quad (35)$$

where:

$$\begin{aligned} p_{m0} &= R_0 - x_{m0} \\ p_{m1} &= \dot{R}_0 - (y_{m0} \dot{\delta}_{m0} + z_{m0} \dot{\gamma}_{m0}) \\ p_{m2} &= \ddot{R}_0 - (x_{m0} \ddot{\delta}_{m0} + 2y_{m0} \dot{\delta}_{m0} \dot{\gamma}_{m0} \\ &\quad + 2(y_{m0} \dot{\gamma}_{m0} + z_{m0} \dot{\delta}_{m0}) \dot{\delta}_{m0} \dot{\gamma}_{m0} \\ &\quad + (x_{m0} \dot{\gamma}_{m0}^2 + 2z_{m0} \dot{\gamma}_{m0} \dot{\delta}_{m0}) \dot{\gamma}_{m0}^2 \\ &\quad + (y_{m0} \ddot{\delta}_{m0} + z_{m0} \ddot{\gamma}_{m0}) \end{aligned} \quad (36)$$

The zero subscripts in Eq. (36) indicate that the associated quantities are to be evaluated at  $t = 0$ . The superscript dots denote differentiation with respect to  $t$ , while  $\delta$  and  $\gamma$  superscripts denote partial differentiation with respect to these variables. For example,  $x_{m0}^{\delta\delta} = \left[ \frac{\partial^2(x_m)}{\partial \delta_m^2} \right]_{t=0}$ .

In deriving expression (36), we made use of the relations:  $\delta_{m0} = \gamma_{m0} = 0$ , and  $x_{m0}^{\delta} = x_{m0}^{\gamma} = 0$ . The first two are obvious since  $S_m$  lies on the  $x$  axis when  $t = 0$ . The second two imply that when the angle between  $OS_m$  and  $OP_m$  is differentially small, the  $x$  coordinate of the  $m$ th highlight point does not change for an incremental change in  $\delta_m$  or  $\gamma_m$ . This conclusion is reached by noting that, since the scatterer is very far from the radar, the directions of both the incident and reflected energy are nearly parallel to the  $x$  axis. Therefore to satisfy Snell's law, the  $m$ th highlight must be located so that its tangent plane is perpendicular to the  $x$  axis. Since an incremental change in aspect causes the highlight to move parallel to its tangent plane, there is no resulting change in its  $x$  coordinate.

It is important to give a physical interpretation to  $p_{m1}$  in (36), since this quantity will form the kernel of the desired Fourier transform. The term  $\dot{R}_0$  is the radial velocity of the center of gravity of the aircraft at  $t = 0$ , and when multiplied by  $2k = \frac{4\pi}{\lambda}$ , yields the doppler frequency of the aircraft. With regard to the term  $-(y_{m0}\dot{\delta}_{m0} + z_{m0}\dot{\gamma}_{m0})$ , we note that

$$\dot{\delta}_m = w_{mz}$$

$$\dot{\gamma}_m = -w_{my}$$

(37)

so this term becomes  $-\left[ y_{m0} (w_{mz})_0 - z_{m0} (w_{my})_0 \right]$ , which can readily be shown to equal the mixed triple product  $-\left[ \bar{r}_{m0} \cdot (\bar{w}_{m0} \times \bar{a}_1) \right]$ . The latter can be interpreted as the product of  $\dot{\theta}_{m0}$  and the projection of  $\bar{r}_{m0}$  on  $\bar{b}_{m0}$ . If this projection is denoted by  $(r_{m0})_{bm}$ , then:

$$p_{m1} = \dot{R}_0 - \dot{\theta}_{m0} (r_{m0})_{bm} \quad (38)$$

Expression (38) for  $p_{m1}$  will be useful when we come to interpret the physical significance of the short-time Fourier transform.

#### 4.2 Derivation and Interpretation of the Short-Time Fourier Transform in the Conventional Case.

The analysis of this section is analogous to that presented in section 2.3. Its main purpose is to show that the short-time Fourier transform of the received signal yields approximately a relative projected distribution of the highlights, and that the approximation can be made as exact as we please by letting both the time interval of integration  $T$ , and the wavelength, approach zero. In addition we shall show that the short-time transform of the square of the envelope of the received signal gives approximately the autocorrelation of the relative projected distribution.

We begin by writing down the complex expression for the received signal, analogous to Eq. (6). It is:

$$F(\delta_1, \dots, \delta_m, \gamma_1, \dots, \gamma_m) = \bar{F}(t) = \sum_{m=1}^M k_m e^{j2k(s_m Q_m)} \quad (39)$$

[REDACTED]

where  $S_m Q_m$  is given in terms of  $\delta_m \gamma_m$  by Eq. (34), or as a Taylor series expansion in time by Eq. (35). We shall use the latter expression because a conventional radar measures the received signal as a function of time only, the aspect angles being unknown. At the same time we replace  $K_m$  by its Taylor expansion, and (39) becomes:

$$\bar{F}(t) = \sum_{m=1}^M \left\{ \left( K_{m0} + \dot{K}_{m0} t + \frac{\ddot{K}_{m0}}{2} t^2 + \dots \right) \cdot e^{j2k(p_{m0} + p_{m1} t + \frac{1}{2} p_{m2} t^2 + \dots)} \right\} \quad (40)$$

Now let us decompose each of the quantities  $p_{m0}$ ,  $p_{m1}$ , into two parts as follows:

$$\left. \begin{aligned} p_{m0} &= R_0 - p_{m0}^* \\ p_{m1} &= \dot{R}_0 - p_{m1}^* \\ p_{m2} &= \ddot{R}_0 - p_{m2}^* \end{aligned} \right\} \quad (41)$$

where the starred symbols are defined by relations (36). The purpose of the above decomposition is to separate the contributions produced by the radial motion of the aircraft center of gravity from those produced by rotation of the aircraft relative to the radar. By using relation (41), Eq. (40) may be written:

$$\bar{F}(t) = \left\{ e^{j2k(R_0 + \dot{R}_0 t + \frac{1}{2} \ddot{R}_0 t^2 + \dots)} \right\} \times \quad (42)$$

$$\left\{ \sum_{m=1}^M \left[ \left( K_{m0} + \dot{K}_{m0} t + \frac{1}{2} \ddot{K}_{m0} t^2 + \dots \right) \cdot e^{-j2k(p_{m0}^* + p_{m1}^* t + \frac{1}{2} p_{m2}^* t^2 + \dots)} \right] \right\}$$

[REDACTED]

We may drop the constant phase factor  $e^{j2kR_0}$  without loss of generality, and the remaining term outside the summation sign may be written  $e^{j\omega_d t}$ , where  $\omega_d = 2k(\dot{R}_0 t + \frac{1}{2} \ddot{R}_0 t^2 + \dots)$  is the instantaneous doppler frequency of the center of gravity of the aircraft at time  $t$ .  $\omega_d$  will be referred to frequently as the mean doppler frequency of the received signal. Now define a derived signal  $F^*(t)$  by:

$$F^*(t) = F(t) \cdot e^{-j\omega_d t} \tag{43}$$

Equations (42) and (43) yield:

$$F^*(t) = \sum_{m=1}^M \left[ (K_{m0} + \dot{K}_{m0} t + \dots) \cdot e^{-j2k(p_{m0}^* t + p_{m1}^* t + \frac{1}{2} p_{m2}^* t^2 + \dots)} \right] \tag{44}$$

Next denote  $2k p_{m1}^*$  by  $\omega_{m0}$ , and the short-time Fourier transform of  $F^*(t)$  by  $\bar{A}(\omega_1, \dots, \omega_M)$ . The transform of Eq. (44) is then:

$$\bar{A}(\omega_1, \dots, \omega_M) \approx \frac{1}{2T} \sum_{m=1}^M \left\{ e^{-j2kp_{m0}^* t} \int_{-\frac{T}{2}}^{\frac{T}{2}} (K_{m0} + \dot{K}_{m0} t + \dots) \cdot e^{j[(\omega_m - \omega_{m0})t - kp_{m2}^* t^2 + \dots]} dt \right\} \tag{45}$$

where:

$$\omega_m = 2k(y\dot{\delta}_{m0} + z\dot{\gamma}_{m0}); \quad m = 1, 2, \dots, M. \tag{46}$$

The quantities  $\omega_{m0}$  and  $\omega_m$  are seen to have the dimensions of frequency. Consequently the function  $\bar{A}$ , which has previously been termed the relative projected highlight distribution, may

[REDACTED]

be more appropriately referred to as the short-time spectrum of the received signal. The significance of the  $M$  independent frequency variables in the argument of  $\bar{A}$  will be clarified shortly.

Now as  $T$  approaches zero, the terms  $\dot{K}_{m0} T$  and  $k_{p_{m2}}^* T^2$  become  $\ll K_{m0}$  and  $(\omega_m - \omega_{m0}) T$  respectively. Hence the right hand side of equation (45) approaches:

$$\frac{1}{2\pi} \sum_{m=1}^M \left\{ e^{-j2k_{p_{m0}}^*} \int_{-\frac{T}{2}}^{\frac{T}{2}} K_{m0} e^{j(\omega_m - \omega_{m0})t} dt \right\} \quad (47)$$

Integration of (47) yields:

$$\bar{A}(\omega_1, \dots, \omega_M) \approx \sum_{m=1}^M \left\{ K_{m0} e^{-j2k_{p_{m0}}^*} \frac{\sin\left[(\omega_m - \omega_{m0}) \frac{T}{2}\right]}{\pi \left[(\omega_m - \omega_{m0}) \frac{T}{2}\right]} \right\} \quad (48)$$

The right hand side of Eq. (48) comprises a sum of  $\frac{\sin x}{x}$  functions, the center frequency of the  $m$ th function being  $\omega_{m0}$ . All these functions have the same half power bandwidth given by:

$$\Delta\omega = \frac{2\pi}{T} \quad (49)$$

An apparent inconsistency is observed in connection with result (49), because the half-power bandwidth becomes infinite as  $T$  approaches zero, thus making it appear that resolution will deteriorate rather than improve as  $T$  is decreased. This conclusion is superficial however, because resolution is determined by the ratio of bandwidth to center frequency rather than by bandwidth

[REDACTED]

[REDACTED]

alone, and the resolution is increased by decreasing this ratio. To ensure a decrease it is necessary that the center frequencies grow faster than the bandwidth as T approaches zero. In terms of  $\lambda$  and T, the ratio is:

$$\left(\frac{\Delta\omega}{\omega_{m0}}\right) = \left[ \frac{\frac{2\pi}{T}}{\frac{4\pi}{\lambda} p_{m1}} \right] = \left(\frac{\lambda}{T}\right) \left(\frac{1}{2p_{m1}}\right) \quad (50)$$

Hence any desired degree of resolution can be obtained by letting  $\lambda$  approach zero more rapidly than T. A similar situation arose in the analysis of Chapter 2, where  $\lambda$  was required to approach zero more rapidly than V. (See remarks immediately following Eq. (20).) In the present case the effect of the limiting operation is to make the frequency spread of the short-time spectrum  $\bar{A}(\omega_1, \dots, \omega_M)$  infinitely great. Obviously practical limitations will set an upper bound on the spectral spread which computing equipment can accommodate.

The appearance of the M independent frequency variables in  $\bar{A}(\omega_1, \dots, \omega_M)$  results because we have assumed that each highlight surface can move independently due to flexural vibration. Hence the transformation of Eq. (45) is actually performed with respect to M different coordinate systems, one corresponding to each highlight surface. To be absolutely precise, identifying superscripts should be appended to the variables y, z, appearing in Eq. (46), to show that they are associated with the m th coordinate frame. They were omitted to avoid overcomplicating the notation.

Now consider the special case where flexural vibrations

[REDACTED]

are absent. All angular velocity vectors  $\bar{\omega}_m$  reduce to  $\bar{\omega}_r$ , and all curves  $C_m$  reduce to a common curve  $C$ , on which the radar has position  $S$  at time  $t$ , the tangent vector to  $S$  being  $\bar{b}$ . Furthermore, the angular rate of change of aspect,  $\dot{\theta}_m$ , reduces to  $\dot{\theta}$ , so the equation:

$$\omega_{m0} = 2k\dot{\theta}_{m0} (r_{m0})_{bm} \quad (51)$$

which is derived from Eqs. (38), (41), and the definition of  $\omega_{m0}$ , reduces to:

$$\omega_{m0} = 2k\dot{\theta}_0 (r_{m0})_b \quad (52)$$

Finally  $\delta_m$  and  $\gamma_m$  reduce to  $\delta$  and  $\gamma$  respectively and the  $M$  frequency variables ( $\omega_1, \dots, \omega_M$ ) become replaced by a common variable  $\omega$ ,  $= 2k(y\dot{\delta}_0 + z\dot{\gamma}_0)$ . Therefore Eq. (48) becomes:

$$\bar{A}(\omega) = \sum_{m=1}^M K_{m0} \epsilon^{-j2kp_{m0}^*} \cdot \frac{\sin \left[ (\omega - \omega_{m0}) \frac{T}{2} \right]}{\pi \left[ (\omega - \omega_{m0}) \frac{T}{2} \right]} \quad (53)$$

Equation (52) indicates that the center frequency  $\omega_{m0}$  of the  $m$ th  $\frac{\sin x}{x}$  function is proportional to the projected distance  $(r_{m0})_b$  of the  $m$ th highlight point from the aircraft center of gravity, the projection being onto a line through the center of gravity and parallel to  $\bar{b}$ .  $\omega_{m0}$  is also proportional to the angular rate of change of aspect  $\dot{\theta}_0$ . Provided  $\bar{\omega}_r$  remains constant in magnitude and direction both  $\dot{\theta}_0$  and  $(r_{m0})_b$  will be constant, and the center frequencies of the  $\frac{\sin x}{x}$  functions will remain stationary. However their spacing cannot yield the



[REDACTED]

absolute projected positions of the highlights because both  $\dot{\theta}_0$  and the direction of  $\bar{b}$  are unknown. At most we can only say that the center frequencies are spaced proportionately to the projected positions of the highlights. In the more general case where vibrations are present, each highlight can move independently, with a resulting significant motion of the  $\frac{\sin x}{x}$  humps relative to one another. Consequently the short-time frequency spectrum may not even provide an accurate measure of the relative projected positions in this situation.

The above discussion indicates that there may be considerably less highlight information obtainable from a conventional radar than from a multireceiver radar. In particular if the aircraft rate of change of aspect becomes zero, the short-time spectrum collapses into the origin. This may occur for radial flight courses when random yaw and roll is negligible. The optimum type of flight maneuver for purposes of highlight resolution is one in which the aircraft rotates at a constant rate about a fixed axis. This type of motion will be referred to subsequently as ideal target motion.

We conclude this section with a brief discussion of the highlight information obtainable from the amplitude of the received signal in the conventional case. Analogous to the result in section 2.4, the short-time Fourier transform of the amplitude squared yields the autocorrelation of the short-time spectrum. Denoting the autocorrelation of  $\bar{A}(\omega_m)^*$  by

-----  
\*  $\bar{A}(\omega_m)$  is an abbreviation for  $\bar{A}(\omega_1, \dots, \omega_M)$ .

$\bar{R}_A(\omega_m)$ , the following result may be derived:

$$\bar{R}_A(\omega_m) \approx \left\{ \begin{aligned} & \sum_{m=1}^M \left\{ K_{m0}^2 \cdot \frac{\sin \omega_m \frac{T}{2}}{\omega_m} \right\} \\ & + \sum_{m=2}^M \sum_{n=1}^{M-1} \left\{ K_{m0} K_{n0} \left[ \frac{\sin \left[ (\omega_m + (\omega_{m0} - \omega_{n0})) \frac{T}{2} \right]}{(\omega_m + (\omega_{m0} - \omega_{n0}))} \cdot e^{j(\rho_m - \rho_n)} \right. \right. \\ & \quad \left. \left. + \frac{\sin \left[ (\omega_m - (\omega_{m0} - \omega_{n0})) \frac{T}{2} \right]}{(\omega_m - (\omega_{m0} - \omega_{n0}))} \cdot e^{-j(\rho_m - \rho_n)} \right] \right\} \end{aligned} \right. \quad (54)$$

Equation (54) is identical in form to Eq. (25) for  $R_A(y)$ , and is again obtained on the assumption that there is no appreciable overlap of the  $\frac{\sin x}{x}$  functions. It also assumes that no two of the difference frequencies  $(\omega_{m0} - \omega_{n0})$  are equal.

The possibility of computing the short-time spectrum from its autocorrelation, which was discussed in section 2.4, exists in the present case as well, and the computation procedure is the same as in the previous case. That is, we would form  $|R_A(\omega_m)|_+$ , which yields the set  $\{K_m K_n; (\omega_m - \omega_n)\}$ , and from it derive the set  $\{K_m; \omega_m\}$ , which in turn yields  $|\bar{A}(\omega_m)|$ . This possibility is again useful, because in the next section we shall see that operational limitations may prevent us from obtaining  $|\bar{A}(\omega_m)|$  directly, whereas there is no operational limitation in obtaining  $|R_A(\omega_m)|$ .

#### 4.3 Practical Problems in Obtaining the Relative Projected Distribution.

In this section we discuss the evaluation of  $|\bar{A}(\omega_m)|$  and



$|R_A(\omega_m)|$  in practice. It will be shown that the latter function can be readily determined under essentially all operational conditions, but not the former. The difficulty is that  $\bar{A}(\omega_m)$  is the short-time transform of the received signal after removal of the mean doppler frequency, and under some operational conditions it is not possible to extract the mean doppler without partially destroying the information-bearing portion of the signal.

To be more explicit,  $\bar{F}(t)$  represents the received signal with only the r-f carrier removed, but with the mean doppler frequency  $\omega_d$  still included. However  $\bar{A}(\omega_m)$  was obtained from  $f^*(t)$ , which in turn was derived from  $\bar{F}(t)$  by removal of the doppler term. (See Eq. (43).)  $\bar{F}(t)$  is commonly referred to as the doppler signal, and to obtain it a doppler radar\* is required.

The conditions under which  $F^*(t)$  cannot be successfully extracted from  $\bar{F}(t)$  are seen upon examining the spectral character of the latter function. In general it consists of a continuous spectrum centered approximately on the mean doppler frequency. The spectral sidebands are produced in part by the random rotational motion of the highlight points about the center of gravity. However even if rotational motion were completely absent, residual sidebands would remain if the radial velocity of the aircraft is not constant. If velocity variations are

\* A doppler radar is simply one in which facility is provided for removing the transmitter carrier frequency from the received signal, thus yielding  $\bar{F}(t)$ .



[REDACTED]

sufficiently violent in nature, the spectral bandwidth due to these variations may be an appreciable percentage of the spectral spread caused by rotational motion.

In practice, the only method of separating the components due to radial and rotational motion is by frequency discrimination. Obviously, if the two spectra overlap appreciably, it will not be possible to separate them in terms of frequency without partially destroying both. The radial component can be successfully removed from  $\bar{F}(t)$  only when its spectrum is much narrower than the spectrum due to rotational motion. This implies that  $F^*(t)$  is determinable only under operational conditions for which the aircraft acceleration and its higher derivatives are not excessive.

An additional complication is that the center frequencies of the  $\frac{\sin x}{x}$  functions in  $\bar{A}(\omega_m)$ , namely  $(\omega_{10}, \dots, \omega_{M0})$  may not all be positive. Consider for example a two-engined aircraft approaching at a constant radial velocity, and at the same time rotating with a constant angular velocity about a vertical axis. The highlight on one nacelle will have a greater radial velocity than the center of gravity, while that on the other nacelle will have a smaller velocity. Hence the two spectral humps in  $\bar{F}(t)$  due to reflections from the nacelles are symmetrically located above and below the mean doppler frequency. Upon forming  $F^*(t)$  by removal of the mean doppler, the low frequency hump will be folded back into the positive frequency region by mirror imaging about the zero frequency axis. This is undesirable because it destroys the spatial ordering of the highlights and also impairs resolution.

[REDACTED]

The way to avoid the folding effect is translate  $F^*(t)$  in frequency, onto a fixed frequency carrier. This effectively changes each  $\omega_{m0}$  to  $(\omega_{m0} + \omega_0)$ , where the carrier  $\omega_0$  must be large enough to make every  $(\omega_{m0} + \omega_0)$  positive. It is interesting to note that this folding effect is precisely analogous to a phenomenon observed in section 3.1 in connection with multireceiver radars. There an ambiguity arose as to which side of the array axis the highlights were on when the axis pointed between them, and it was possible to eliminate the ambiguity by having the axis always point to one side of the highlight distribution. Analogously the present ambiguity is eliminated by ensuring that the frequencies  $(\omega_{10} + \omega_0, \dots, \omega_{M0} + \omega_0)$  all lie to one side of the frequency origin.

The necessity of removing the mean doppler when computing  $\bar{A}(\omega_m)$  does not arise when  $R_A(\omega_m)$  is to be computed, since we use only the envelope of the received signal in the latter case. The truth of this statement can be seen by observing, from Eq. (43), that  $|\bar{F}(t)| = |F^*(t)|$ . This means that the envelope is independent of the mean doppler frequency, so  $\bar{R}_A(\omega_m)$  can be determined without restriction on the type of aircraft motion.

Finally it is observed that the short-time Fourier transforms are computed in the same manner as for a multireceiver system. Thus, in the case of a doppler radar,  $|\bar{A}(\omega_m)|$  is formed by taking the square root of the sum of the squares of  $\text{Re} [\bar{A}(\omega_m)]$  and  $\text{Im} [\bar{A}(\omega_m)]$ . These in turn are derived from  $\text{Re} [F^*(t)]$  and  $\text{Im} [F^*(t)]$  in the same way that  $\text{Re} [A(y)]$  and  $\text{Im} [A(y)]$  were derived from  $\text{Re} [\bar{F}(\omega)]$  and  $\text{Im} [\bar{F}(\omega)]$  in section 3.1.

Thus four Fourier transforms are involved. Similarly  $|\bar{R}_A(\omega_m)|$  is formed by taking the square root of the sum of the squares of  $\text{Re} [\bar{R}_A(\omega_m)]$  and  $\text{Im} [\bar{R}_A(\omega_m)]$ , the latter being equal respectively to the Fourier cosine and Fourier sine transforms of  $|F(t)|^2$ . Hence only two transformations are involved, as was the case in deriving  $|R_A(y)|$  in section 3.2.

#### 4.4 Counting Aircraft, and the Effects of Random Motion, Vibrations, and Propeller Rotation.

The possibility of counting aircraft in a formation is generally not as good for a conventional radar as for a multi-receiver radar, because the former can resolve individual aircraft only on the basis of frequency. Specifically, the spectrum of the doppler signal  $\bar{F}(t)$  from a single aircraft centers about the doppler frequency of its center of gravity. Hence if a number of aircraft in formation all have precisely the same radial velocities, their spectra will be nearly coincident and resolution will be virtually impossible. It is only when the aircraft are maneuvering relative to each other that the mean dopplers are likely to differ enough to separate the spectra and permit counting. This is in contrast to the multireceiver case, where resolution is carried out with respect to azimuth angle and is independent of the aircraft motion.

The experimental data of Chapter 8 include an example of two aircraft flying in close formation. The return signal indicates that their spectra overlapped most of the time, but occasionally one maneuvered relative to the other sufficiently to separate them in frequency and reveal the presence of two

[REDACTED]

aircraft. Thus one can expect to achieve counting occasionally with a conventional radar, particularly if the number of aircraft is small.

The random motion of a single aircraft will generally be most clearly revealed when the mean rate of change of aspect is zero and the roll and yaw motions are appreciable. For example, when an aircraft is on a radial course and is yawing, the entire spectrum will expand and contract along the frequency axis in rhythm with the yaw rate. Since rates will vary from zero up to several degrees per second, the effect on the spectrum should be plainly visible, and in fact should permit the measurement of instantaneous yaw rates. In contrast we recall that rates have no effect on the measurements of a multireceiver radar, therefore we expect random motions to show up much more clearly in the conventional case. We would also expect flexural vibrations to be readily apparent in the latter case, because angular rates imparted to highlights by vibrations are likely to be appreciable. Furthermore, since vibrations cause the spectral humps to move relative to each other, they should be clearly distinguishable from yawing and rolling, in which the aircraft acts as a rigid body and causes all the humps to move in synchronism.

Finally, vibrations may produce such large highlight accelerations as to result in broadening of the spectral humps, to the extent that their humplike appearance is destroyed.\* Since

-----

\* See Chapter 5 for a detailed description of the broadening effect.

[REDACTED]


marked vibrations are likely to occur occasionally rather than continuously, it should be possible to observe their appearances by either the sudden spreading or the relative movement of the affected spectral humps.

Propeller rotation may be considered as an extreme case of non-rigid vibrations. However, highlights may be affected by propellers in two distinct ways. First, highlights on the blades are rotated at blade frequency. Secondly, highlights on the fuselage near the blades may be obscured periodically as the blades pass in front of them. Both categories of highlights can be expected to undergo rapid amplitude modulation, since the fundamental blade frequency is 40 c/sec or higher, thus causing appreciable broadening of the corresponding spectral humps. In addition the highlights on the blades impart violent frequency modulation to their reflected signals, which probably results in total deterioration of the spectral humps. That is, the spectrum of the blade reflections is expected to resemble that of broadband random noise.

Therefore we conclude that propeller rotation will markedly reduce the possibility of resolving highlights, particularly at head-on aspects. The experimental work shows that within about 30 degrees of broadside, highlight points are essentially free of propeller modulation, so that highlight resolution is possible at these aspects. It is again remarked that the resolving ability of multireceiver radars is unaffected by propeller rotation, due to their ability to compute the highlight distribution from an instantaneous measurement.


[REDACTED]



  
CHAPTER 5DERIVATION OF MAXIMUM ALLOWABLE WAVELENGTHS FOR PRESCRIBED  
RESOLUTION

The theory of Chapters 2 and 4 has shown that the finite and short-time Fourier transforms of the received field are sums of  $\frac{\sin x}{x}$  functions, provided the aperture dimension and integrating time respectively are short enough so that highlight amplitudes and positions are nearly constant over these intervals. In particular our use of the Rayleigh criterion of resolution has been based on the assumption of negligible highlight variation. We now wish to determine the way in which highlight variations over the integrating interval modify the ideal  $\frac{\sin x}{x}$  response, in order to evaluate their deteriorating effect on highlight resolution. By adapting the Rayleigh criterion to the modified response shapes, we may obtain realistic estimates of the degree of resolution obtainable at millimeter and centimeter wavelengths.

Specifically we wish to evaluate the maximum permissible wavelength for which highlights having a projected spacing  $d_{\min}$  can be resolved a given percentage of the time, taking into account both highlight variations and aircraft motion. The problem must be treated on a statistical basis, because the character of highlight variations and aircraft motion, which are the factors governing the instantaneous resolution, can only be specified statistically. In the case of a multireceiver radar, highlight variation is the only effect to be considered, whereas



[REDACTED]

for a conventional radar aircraft motion must be taken into account as well. In the special case of ideal aircraft motion, that is, a constant rate of rotation about a fixed axis in the absence of vibrations, the resolving capabilities of a conventional radar become about as good as those of a multireceiver radar. Therefore we shall initially derive a formula for the maximum permissible wavelength which includes the effects of aircraft motion and vibrations, and this will adequately cover the conventional case. Subsequently the multireceiver radar will be treated as a special case of this formula, in which the random motion of the aircraft is replaced by the ideal motion.

We shall make one restricting theoretical assumption, namely that the highlight amplitude variations cause inappreciable deterioration of the  $\frac{\sin x}{x}$  responses compared with that caused by position variations. This assumption turns out to be a reasonable one in the case of a conventional radar, but is somewhat inadequate in the case of a multireceiver radar. It is made for convenience, since the requisite theory applicable to position variations alone has been treated in the literature, but has not been worked out when amplitude changes occur simultaneously, and we do not wish to embark upon such an analysis here.

#### 5.1 Derivation of a General Formula for the Maximum Permissible Wavelength.

The maximum wavelength,  $\lambda_{\max}$ , for which the probability is  $q$  that a pair of highlight points having projected spacing  $d_{\min}$  can be resolved, depends on the following factors: the value of

[REDACTED]

[REDACTED]

$d_{\min}$ , the resolution criterion adopted, the statistics of the aircraft motion, and the statistics of the highlight variations as a function of aspect. The resolution criterion will again be the Rayleigh criterion, which states that two highlights are just resolvable when the corresponding spectral humps (which in general will have degenerate  $\frac{\sin x}{x}$  shapes) intersect at their half power points. The statistics of aircraft motion refer specifically to the statistics of the aspect angles  $\delta_m$ ,  $\gamma_m$  and their derivatives, these angles being defined in section 4.1. The statistics of the highlight variations refer to those of  $K_m$ ,  $y_m$  and  $z_m$ , considered as functions of  $\delta_m$  and  $\gamma_m$ .

The first task is to determine how the spectral humps depart from the  $\frac{\sin x}{x}$  shape when the interval of integration in Eq. (45), section 4.2, is not small enough to make expression (47) an adequate approximation. The latter expression represents the integral of a sine wave over the interval T, but in the more exact expression (Eq. (45)), the sine wave has both amplitude and frequency modulation superimposed, due to the presence of the additional terms  $\dot{K}_{m0} t$ ,  $kp_{m2}^* t$ , and higher order terms. These additional terms are produced by the combined effects of highlight variation as a function of aspect, and aspect variation as a function of time.

Consider the signal received from a representative highlight point. On dropping the identifying subscript m, the component of the real part of  $F^*(t)$  generated by this highlight is (see Eq. (44):

$$f(t) = (K_0 + \dot{K}_0 t + \dots) \cdot \cos \left[ \frac{4\pi}{\lambda} (p_0^* + p_1^* t + \frac{1}{2} p_2^* t^2 + \dots) \right] \quad (55)$$

[REDACTED]

[REDACTED]

Upon introducing the concept of instantaneous frequency, Eq. (55) may be written:

$$f(t) = (K_0 + \dot{K}_0 t + \dots) \cdot \cos \left[ \frac{4\pi}{\lambda} p_0^* + 2\pi f_{10} t + \frac{2\pi}{2} \dot{f}_{10} t^2 + \dots \right] \quad (56)$$

where  $f_{10} = \frac{2}{\lambda} p_1^*$  is the instantaneous frequency at  $t = 0$ , and  $\dot{f}_{10} = \frac{2}{\lambda} p_2^*$  is the rate of change of frequency at  $t = 0$ , and so forth.

Next consider how the short-time transform of Eq. (56) would be generated in practice. The basic procedure is to apply  $f(t)$  to either a single tunable filter or to a bank of identical fixed-frequency filters whose center frequencies are uniformly spaced so that their responses intersect at their half-power points. The filter response shape is ideally a  $\frac{\sin x}{x}$  function whose bandwidth  $\Delta f$  is related to the integrating time  $T$  by:

$$\Delta f = \frac{1}{T} \quad (57)$$

We shall assume that a bank of filters is employed, so that the complete short-time spectrum is generated simultaneously. It follows from sampling theory that half-power point spacing of  $\frac{\sin x}{x}$  filters is just close enough to permit reconstruction of the entire spectrum from the sampled values. A spectrum analyzer of this type is functionally similar to the "sound spectrograph" which has been used for analyzing speech sounds in acoustical research (19).

Although  $f(t)$  contains all higher derivatives of the instantaneous frequency, it can be shown that for short enough  $T$ , the instantaneous rate of change of frequency,  $\dot{f}_1$ , (also called the frequency sweep rate) is the major one in determining

[REDACTED]

[REDACTED]

the deterioration of the  $\frac{\sin x}{x}$  responses. A formal proof of this fact is omitted. Therefore consider the nature of the spectrum analyzer response when a linearly frequency-modulated signal is applied. If the frequency sweep rate is very slow, the filter responses can be predicted from quasi-static considerations, that is, the shape of the spectrum will closely approximate the static filter shape, and the height of its peak will be proportional to the amplitude of the f-m input signal. Thus the output of the spectrum analyzer will appear as a  $\frac{\sin x}{x}$  hump which slides along the frequency axis in synchronism with the instantaneous applied frequency.

However, as the frequency sweep rate is increased the spectral hump will become broader and reduced in amplitude, and will lag behind the instantaneous applied frequency. Finally when the sweep rate is sufficiently high, the response departs from the static shape entirely and becomes highly extended and oscillatory. Under these conditions the Rayleigh criterion of resolution breakd down, since the distinctive humplike nature is lost and the half-power points cannot be defined. It will therefore be necessary to specify a limiting departure from the  $\frac{\sin x}{x}$  shape beyond which we shall consider resolution to be virtually impossible.

In the following quantitative analysis we shall assume that the response of a  $\frac{\sin x}{x}$  filter to an f-m input is essentially the same as that of a simple RLC filter. The theory of the latter case is presented in detail in reference (20), which includes curves showing the filter response for various values

[REDACTED]

of the applied sweep rate. Let the instantaneous bandwidth of the broadened spectral humps be denoted by  $\Delta f_a$ , and let  $\beta$  denote the limiting degree of broadening for which resolution is considered just possible. That is, the limiting bandwidth is given by:

$$(\Delta f_a)_{\max} = \beta \cdot \Delta f \quad (58)$$

where  $\Delta f$  is the static filter bandwidth. For the simple RLC filter, reference (20) indicates that  $\beta$  is approximately equal to two. A further result for the RLC circuit is that the rate of frequency sweep required to obtain a specified degree of broadening is proportional to the square of the static bandwidth. For instance, if the specified degree of broadening is the limiting value  $\beta$ , then the relation is:

$$(\dot{f}_1)_{\beta} = \alpha (\Delta f)^2 \quad (59)$$

where  $\alpha$  is a constant, and  $(\dot{f}_1)_{\beta}$  denotes the frequency sweep rate required to produce broadening  $\beta$ . This result can be shown to hold for any tuned filter; the value of  $\alpha$  depends on the particular type of filter. For an RLC circuit is found (20) that when  $\beta = 2$ ,  $\alpha \approx 3$ .

Let  $\Delta f_1$  be the instantaneous frequency separation between spectral humps corresponding to highlight points whose projected spacing is  $d_{\min}$ . It is evident that these two points can be resolved when  $\Delta f_1$  is greater than the hump bandwidth  $\Delta f_a$ , provided that  $\Delta f_a$  is not greater than  $\beta \cdot \Delta f$ . (For otherwise resolution is essentially impossible.) The problem therefore reduces to finding the value of  $\lambda_{\max}$ , and the corresponding value

[REDACTED]

of T, such that the probability of simultaneously having  $\Delta f_a \leq \Delta f_1$  and  $\Delta f_a \leq \beta \cdot \Delta f$ , is q. It will be convenient in what follows to denote the ratio  $(\frac{\lambda}{T})$  by L. Therefore, in more concise notation, the requirement is to determine  $\lambda_{\max}$  and L such that:

$$q = \text{Prob.} \left[ \Delta f_a \leq \Delta f_1 ; \Delta f \leq \Delta f_a \leq \beta \cdot \Delta f \right] \quad (60)$$

For brevity we introduce the variables, u, v and w, defined by:

$$u = \lambda \dot{f}_1 ; \quad v = \lambda \cdot \Delta f_1 ; \quad w = \lambda \cdot \Delta f_a \quad (61)$$

In terms of the new variables, (60) may be written:

$$q = \text{Prob.} \left[ w \leq v ; L \leq w \leq \beta L \right] \quad (62)$$

In Eq. (62) we used the result that:

$$\lambda \cdot \Delta f = L \quad (63)$$

which follows directly from Eq. (57) and the definition of L.

It can be deduced from Eq. (59) that the ratio  $(\frac{\Delta f_a}{\Delta f})$  is constant whenever the ratio  $\left[ \frac{\dot{f}_1}{(\Delta f)^2} \right]$  is constant. Hence we conclude that a functional relation of the form

$$\frac{\Delta f_a}{\Delta f} = g \left[ \frac{\dot{f}_1}{(\Delta f)^2} \right] \quad (64)$$

exists, where the form of the function g depends on the type of filter. By inserting  $\lambda$  in appropriate places on both sides of Eq. (64), we obtain

$$w = L \cdot g \left[ \left( \frac{\lambda u}{L} \right)^2 \right] \quad (65)$$

[REDACTED]

It can be shown that  $g$  is a monotonic function of its argument. Therefore (65) has a single-valued inverse, namely:

$$u = \frac{L^2}{\lambda} \cdot h\left(\frac{w}{L}\right) \quad (66)$$

where  $h$  is a monotonic function.

Now let  $W(v, w)$  denote the joint probability density distribution of  $v$  and  $w$ . Then Eq. (60) can be expressed in the integral form:

$$q = \int_L^{\beta L} dw \int_w^{\infty} W(v, w) dv \quad (67)$$

By making use of the functional relation between  $u$  and  $w$ , as expressed by (65) and (66), we may write (67) as:

$$q = \int_0^{\frac{L^2}{\lambda} \cdot h(\beta)} du \int_{L \cdot g\left(\frac{\lambda u}{L^2}\right)}^{\infty} W(u, v) dv \quad (68)$$

where  $W(u, v)$  is the joint probability distribution of  $u$  and  $v$ . Upon integration, (67) yields a relation of the form:

$$q = G(\lambda, L, \beta) \quad (69)$$

which, for prescribed values of  $q$  and  $\beta$ , represents a curve in the  $(\lambda, L)$  plane. This means that there is more than one pair of values  $(\lambda, L)$  which satisfy Eq. (60). The maximum admissible value of  $\lambda$ , and the corresponding  $L$  value, are determined by the point on this curve which maximizes  $\lambda$ .



It should be noted that Eq. (60) actually ensures that the probability of resolution is at least  $q$ . This is because it does not take into account those occasions when the condition:  $(\Delta f_a \leq \Delta f_1; \Delta f_a \geq \beta \cdot \Delta f)$  holds. On at least some of these occasions resolution will be possible in practice. Hence the value of  $\lambda_{\max}$  as determined by (60) should be slightly pessimistic. That is, we shall expect to achieve a slightly higher value of  $q$  in practice than that specified in the calculation. In the next section we shall apply the preceding theory to obtain representative values of  $\lambda_{\max}$  for various values of  $q$ .

## 5.2 Calculation of Permissible Wavelengths for a Conventional Radar.

The purpose of this section is to derive quantitative estimates of  $\lambda_{\max}$  and  $L$  for various values of  $q$ , for the case of a conventional radar, when hypothetical statistics are prescribed for the aircraft motion and highlight point behavior. The results will be highly approximate because there is not nearly enough empirical data available from which to determine the required statistics.

Specifically, the problem is to integrate the right hand side of Eq. (68). Thus we require explicit expressions for the functions  $W(u, v)$ ,  $g(\frac{\lambda u}{L^2})$  and  $h(\beta)$ . In order to obtain a solution of (68) in closed form, we shall arbitrarily assume that  $u$  and  $v$  are statistically independent, and that their individual probability distributions are given by the following simple functions.

$$\left. \begin{aligned} W(u) &= k_1 \epsilon^{-k_1 u} \\ W(v) &= k_2 \epsilon^{-k_2 v} \end{aligned} \right\} u, v \geq 0 \quad (70)$$

where  $k_1$  and  $k_2$  are constants to be selected later. The data which are presented in reference (20) indicate that, for an RLC filter,  $g$  is closely approximated by the following linear relation:

$$L \cdot g\left(\frac{\lambda u}{L^2}\right) = L + \frac{\lambda u}{6L} \quad (71)$$

The inverse solution of (71) yields:

$$h(\beta) = 6(\beta - 1) \quad (72)$$

We shall assume that the results for an RLC filter apply satisfactorily to a  $\frac{\sin x}{x}$  filter. As stated previously, the RLC results indicate that an appropriate value of  $\beta$  is two. On substituting the above quantities into Eq. (68) and integrating, we obtain:

$$q \left(1 + \frac{k_2 \lambda}{6k_1 L}\right) = \left(\epsilon^{-k_2 L}\right) \left(1 - \epsilon^{-k_2 L} \cdot \epsilon^{-\frac{6k_1 L^2}{\lambda}}\right) \quad (73)$$

For a given value of  $q$ , Eq. (73) represents a curve in the  $(\lambda, L)$  plane, whose general shape is shown in Figure 7.

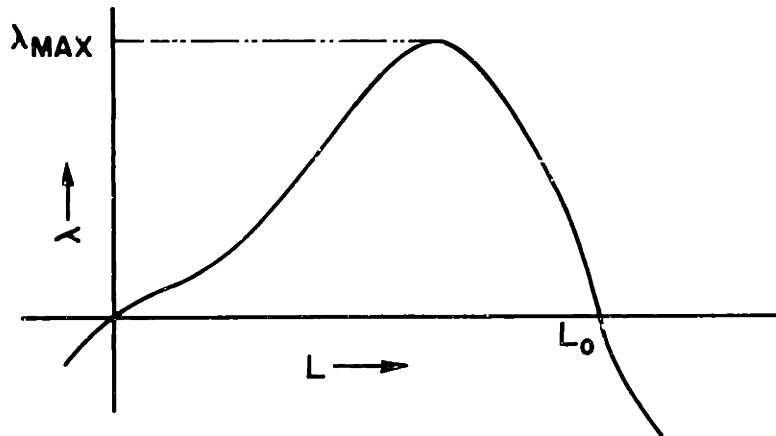


FIGURE 7

General Shape of the  $(\lambda, L)$  Curve for a Given  $q$ .

It intersects the  $L$  axis at  $L = 0$  and at  $L = L_0 = \frac{1}{k_2} \cdot \ln\left(\frac{1}{q}\right)$ . An accurate plot of the above curve for representative values of  $k_1$  and  $k_2$  shows that the abscissa of the maximum point is given approximately by  $L = \frac{2}{3} L_0$ . On substituting this value into (73), we obtain the following equation for  $\lambda_{\max}$ .

$$(q)^{\frac{1}{3}} \cdot \left(1 + \frac{p \lambda_{\max}}{4 \ln\left(\frac{1}{q}\right)}\right) = \left[1 - (q)^{\frac{2}{3}} \cdot e^{-\frac{8 \ln\left(\frac{1}{q}\right)^2}{3p \lambda_{\max}}}\right] \quad (74)$$

$$\text{where } p = \left[\frac{k_2}{k_1}\right]^2. \quad (75)$$

Since  $p$  and  $\lambda_{\max}$  appear only in the combination  $(p\lambda_{\max})$  in (74), it is useful to solve for this quantity as a function of  $q$ . The results are plotted in Figure 8. This graph permits the evaluation of  $\lambda_{\max}$  for specified values of  $q$  and  $p$ , but only for

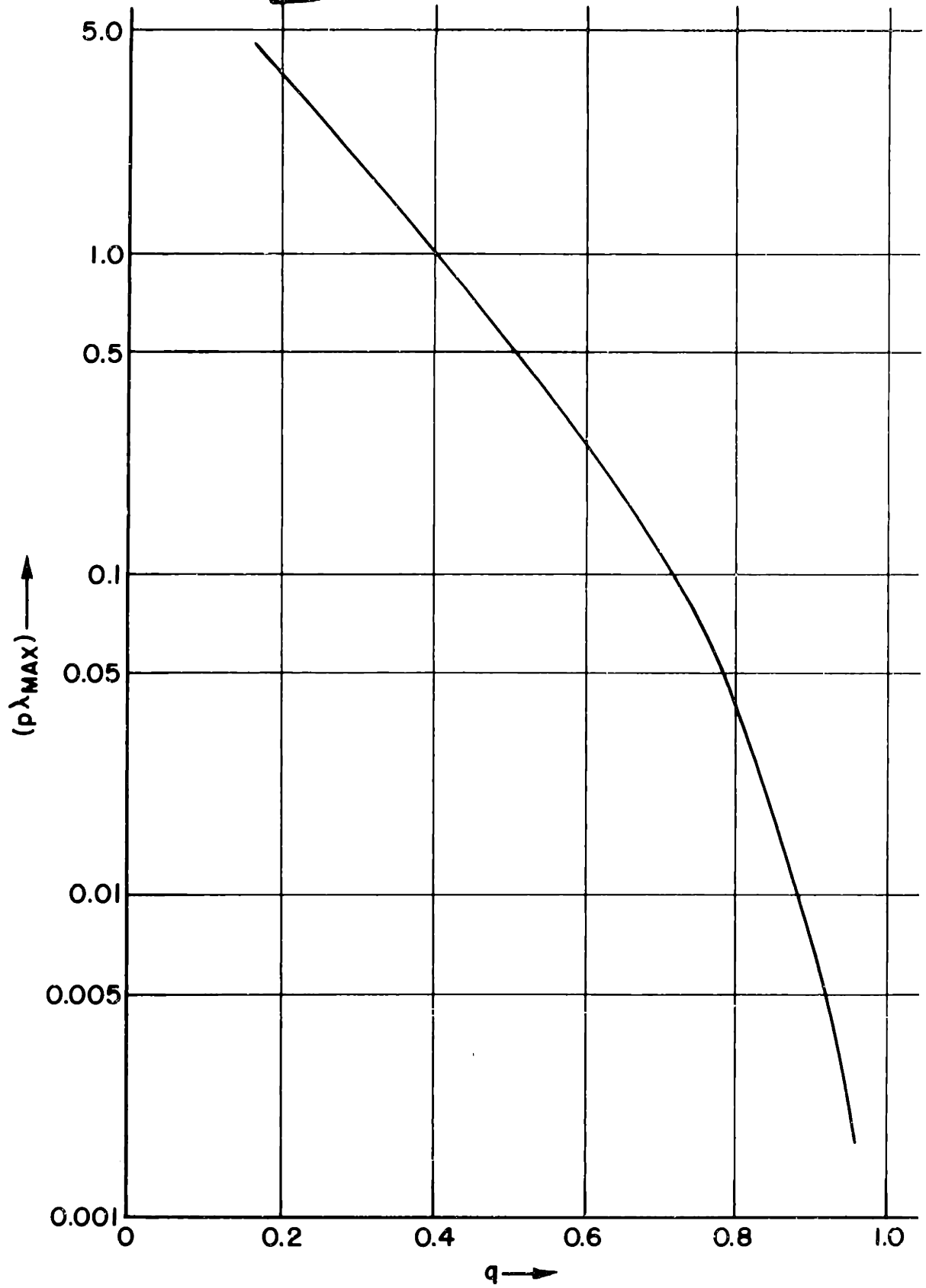


FIGURE 8.

Graph of  $(p\lambda_{\max})$  Versus  $q$ .

[REDACTED]

the exponential statistics hypothesized in Eq. (70). Numerical values may be obtained as soon as we specify  $k_1$  and  $k_2$ . To choose realistic values for the latter quantities, it is necessary to attach a physical significance to them. It is readily shown from (70) that:

$$\text{Prob. } (u \leq \frac{1}{k_1}) = \text{Prob. } (v \leq \frac{1}{k_2}) = (1 - \frac{1}{\epsilon}) = 0.63 \quad (76)$$

Thus the reciprocals of  $k_1$  and  $k_2$  respectively represent the values of  $u$  and  $v$  for which the probability that the variables are less than these values is 0.63.

Next, we must express  $u$  and  $v$  in terms of the highlight point positions and the parameters specifying the aircraft motion. From Eqs. (61), (56), (41), and (36), it follows that:

$$\left. \begin{aligned} u = \lambda \dot{f}_1 = 2p_2^* &= 2 \left\{ (x^{\delta\delta} + 2y^{\delta}) \dot{\delta}^2 + 2(y^\gamma + z^{\delta}) \dot{\delta}\dot{\gamma} \right. \\ &\quad \left. + (x^{\gamma\gamma} + 2z^\gamma) \dot{\gamma}^2 + (y\ddot{\delta} + z\ddot{\gamma}) \right\} \\ v = \lambda \cdot \Delta f_1 = 2 \Delta p_1^* &= 2 (\Delta y \cdot \dot{\delta} + \Delta z \cdot \dot{\gamma}) \end{aligned} \right\} \quad (77)$$

The identifying subscript  $m$ , and the time subscript  $o$ , have been omitted throughout (77), since we are now focussing attention on the average behavior of a representative highlight point having coordinates  $(x, y, z)$ . Also  $\Delta y$  and  $\Delta z$  respectively represent the differences in the  $y$  and  $z$  coordinates of two representative points whose projected separation is  $d_{\min}$ .

[REDACTED]

[REDACTED]

It may be worth remarking here that it is theoretically possible to compute  $W(u, v)$  from relations (77), provided the joint distribution of all the variables appearing on the right hand sides in (77) is known. This set of variables will be referred to as the "primary variables". At present the empirical data necessary to construct the primary distribution are virtually nonexistent, and it would be a major project to obtain them. The ancillary problem of computing  $W(u, v)$  from the primary joint distribution would no doubt require a large digital computer, since it could not be performed analytically. Consequently the best we can do here is to choose values of the primary variables which seem to be in accord with the meager information available. We shall then assume that the values so selected, when substituted into (77), will yield values of  $u$  and  $v$  which are equal to  $\frac{1}{k_1}$  and  $\frac{1}{k_2}$  respectively. It is evident that the proposed method for evaluating  $k_1$  and  $k_2$  is very crude, therefore the resulting estimates of  $\lambda_{\max}$  cannot be considered too significant.

The values of the angular rate and acceleration variables which are quoted below are based on measurements of random aircraft motion supplied by the Instrumentation Laboratory, M.I.T., and the National Advisory Committee for Aeronautics. The numbers are representative of situations in which aspect change is caused primarily by yaw and roll rather than by purposeful flight maneuvers. The variables associated with the motions of the highlight points as a function of aspect were estimated from the geometry of typical aircraft surfaces. The following set of values has been selected as typical.

$$\dot{\delta} = \dot{\gamma} = \frac{1}{30} \text{ radian/second}$$

$$\ddot{\delta} = \ddot{\gamma} = \frac{1}{8} \text{ radian/(second)}^2$$

$$\Delta y = \Delta z = 3 \text{ feet} \quad (78)$$

$$y = z = 40 \text{ feet}$$

$$y^{\delta} = y^{\gamma} = z^{\delta} = z^{\gamma} = 50 \text{ feet/radian}$$

$$x^{\delta\delta} = x^{\gamma\gamma} = 30 \text{ feet/(radian)}^2$$

On substituting these values into (77), we obtain:  $\frac{1}{k_1} \approx 21$ ;  $\frac{1}{k_2} \approx \frac{2}{5}$ . Hence  $p \approx 120$ . For the above value of  $p$  we obtain the following table of values of  $\lambda_{\max}$  for three values of  $q$ , by reading points from the curve in Fig. 8. We also include the corresponding values of  $L$  and  $T$ .

$q$	$\lambda_{\max}$	$L(\frac{2}{5} L_0)$	$T(= \frac{\lambda_{\max}}{L})$
0.20	0.033 feet $\approx$ 1.0 cm.	0.43	0.078 sec.
0.50	0.0045 " $\approx$ 1.3 mm.	0.184	0.024 "
0.80	0.00033 " $\approx$ 0.1 mm.	0.059	0.0056 "

TABLE I

The table indicates that the wavelength decreases very rapidly as the probability of resolution is increased. It also indicates that wavelengths of not more than a few millimeters are required for reasonably good resolution.

It is useful to have a more intuitive idea of how the important parameters contribute in determining the value of  $\lambda_{\max}$ .

In this regard it is easily shown from the above equations that, for fixed  $q$ ,  $\lambda_{\max}$  depends on the minimum resolving distance, the rate of change of aspect and the aspect acceleration, approximately as follows.

$$\lambda_{\max} \propto \left[ \frac{d_{\min}^2 \dot{\theta}^2}{\ddot{\theta}} \right] \quad (79)$$

Thus, doubling either the minimum resolving distance, or the rate of change of aspect, increases  $\lambda_{\max}$  by a factor of four. Equation (79) is true only when the aspect acceleration is appreciable. This is so when yaw, roll and pitch are the principal contributors to aspect change, but not true when the aircraft is turning at a constant rate which is large compared with yaw and roll rates. In such cases  $\ddot{\theta}$  may be appreciably smaller than  $\dot{\theta}$  and we must resort to the exact formulae, given by Eq. (77).

In closing this section, some remarks are in order concerning the effect of non-rigid vibrations on the value of  $\lambda_{\max}$ . The preceding calculations have been based tacitly on the assumption of rigid body motion. The effect of vibrations can be partially accounted for by choosing appropriate values for the angular rate and acceleration variables in (77). For example, if two highlight points whose projected separation is  $d_{\min}$  undergo a common sinusoidal vibration of angular amplitude  $A$  and angular frequency  $\omega$ , the average rate of change of aspect imparted to them is  $\frac{1}{2}A\omega$ , and the average aspect acceleration is  $\frac{1}{2}A\omega^2$ . Suppose the angular motion of this pair of points is confined to the plane of the variable  $\delta$ , so that:  $\dot{\delta} = \frac{1}{2}A\omega$ ,  $\ddot{\delta} = \frac{1}{2}A\omega^2$ , and  $\dot{\gamma} = \ddot{\gamma} = 0$ .



Consider two specific cases:

$$(i) \quad A = \frac{1}{100} \text{ radian} \approx 0.57^\circ; \quad \omega = 10 \text{ rad./sec.} \approx 1.6 \text{ cps.}$$

$$(ii) \quad A = \frac{1}{400} \text{ radian} \approx 0.14^\circ; \quad \omega = 40 \text{ rad./sec.} \approx 6.4 \text{ cps.}$$

Case (i) may be representative of a wing vibration and case (ii) of a body vibration. The associated values of  $\dot{\delta}$  and  $\ddot{\delta}$  are:

$$(i) \quad \dot{\delta} = \frac{1}{20}; \quad \ddot{\delta} = \frac{1}{2}$$

$$(ii) \quad \dot{\delta} = \frac{1}{20}; \quad \ddot{\delta} = 2$$

Substitution of these values, along with those of the remaining parameters as specified in (78), into (77), we obtain the following values of  $p$ :

$$\text{Case (i): } p = 450; \quad \text{Case (ii): } p = 1780.$$

Hence the computed values of  $\lambda_{\max}$  will be respectively 3.7 and 14.8 times smaller than those given in Table I, for corresponding values of  $q$ . The above analysis therefore indicates that vibrations can produce a marked deterioration in resolution when using a conventional radar. As pointed out previously, they cause no deterioration in multireceiver systems.

### 5.3 Calculation of Permissible Wavelengths for a Multireceiver Radar.

Equation (74) will yield approximate results in the case of a multireceiver radar if the aircraft motion is taken to be ideal. This is true because ideal motion is equivalent to holding the aircraft fixed and moving the radar receiver around it on a great circle segment of radius  $R$ , at a constant angular rate. During time  $T$  the receiver will trace out an arc which we can identify with the arc occupied by a one-dimensional multireceiver array.

Furthermore, successive samples of the received field recorded by the moving radar can be identified with the fields measured by the individual receivers of the multireceiver radar.

The only difference between the two cases is that in the conventional case the transmitter moves along the arc coincidentally with the receiver while in the multireceiver case the transmitter remains at the center of the arc. This results in somewhat less highlight variation across the arc in the latter case, hence the specialization of the preceding theory to the multireceiver radar should predict permissible wavelengths which are somewhat low. However this is not a serious error in view of the other shortcomings of the theory.

When the aircraft motion is ideal, the variables  $\dot{\gamma}$ ,  $\ddot{\gamma}$  and  $\ddot{\delta}$  in Eqs. (77) become zero. We have assumed here that the aircraft axis of rotation is oriented so that only the angle  $\delta$  changes while  $\gamma$  is identically zero. Equations (77) therefore reduce to:

$$\begin{aligned} u &= 2 (x^{\delta\delta} + 2 y^{\delta}) \dot{\delta}^2 \\ v &= 2 \Delta y \cdot \dot{\delta} \end{aligned} \tag{80}$$

and  $p$  is given by  $\left[ \frac{x^{\delta\delta} + 2 y^{\delta}}{2 (\Delta y)^2} \right]$ , which is independent of  $\dot{\delta}$  as

it should be. Using the parameter values given in (78), we obtain:

$$\frac{1}{k_1} = 0.29 ; \quad \frac{1}{k_2} = 0.20 , \text{ which yields } p = 7. \text{ In this case}$$

the values of  $\lambda_{\max}$  are 17 times greater than those in Table I,

for corresponding  $q$  values. Consequently it appears that

reasonable highlight resolution should be obtained with 3 centimeter wavelengths when the aircraft motion is the ideal type. This

conclusion must be heavily qualified however, for we recall that the theory of this and the previous section is based on the assumption that the amplitude variations of the highlight reflections are negligible. We shall now show, in a rather qualitative manner, that the effect of amplitude variation is to produce smaller values of  $\lambda_{\max}$  than those predicted here, provided the integration time is long enough.

The reasoning will be clarified by further consideration of the preceding numerical examples. In the example of this section, the computed value of T is 0.83 seconds when  $q = 0.5$ . Also, the rate of change of aspect was specified to be  $\frac{1}{30}$  radian/sec., therefore the aircraft changes its aspect about 1.6 degrees during the integration time. In the first example, Table I indicates that  $T = 0.024$  seconds for  $q = 0.5$ , corresponding to an aspect change of less than  $\frac{1}{20}$ th degree. Experimental data which are exhibited in Chapter 8 show that highlight point amplitudes can change markedly over a degree or two of aspect, but inappreciably in  $\frac{1}{20}$ th degree. Therefore when the integrating time is short enough, it is justifiable to ignore amplitude variations. This implies that the foregoing theory is reasonably adequate when predicting values of  $\lambda_{\max}$  of not more than a few millimeters, but cannot be relied upon when the predicted values are of the order of a centimeter or more.

To summarize, it is concluded that at wavelengths of less than 2 or 3 millimeters, highlight resolution with a conventional radar should be adequate in a large number of operational situations, and the same quality of resolution should be obtainable with a multireceiver radar for wavelengths as long as 5 or 6 milli-

[REDACTED]

meters. The reader should of course keep in mind the tentative nature of these estimates, due both to the approximate nature of the theory and to the glaring deficiency of experimental data, upon which the reliability of numerical results largely depends. A truly satisfactory check on the above wavelength estimates can be provided only by radar measurements made at wavelengths of a few millimeters. Since the experimental results to be described in Chapter 8 were obtained from 3 centimeter data, they do not provide a conclusive test of the theory. However, some significance may be attributed to these experimental results.


## CHAPTER 6

### DESCRIPTIONS OF EXPERIMENTAL DATA, METHODS OF ANALYSIS, AND EQUIPMENT

The experimental phase of the research had two objectives. The first was to obtain a check on the theoretical conclusions of the preceding chapters, and was directed specifically toward determining the degree of resolvability of highlight points at a particular radar wavelength, using a conventional radar. The second was to search for other characteristics of the radar signal which may have been overlooked in the theoretical treatment, and which may assist in distinguishing physical characteristics of aircraft.

The radar data which were subjected to experimental analysis consisted of a considerable quantity of 3 centimeter measurements taken by J. B. Angell (2), formerly of this laboratory. It would have been desirable to perform the experimental work on data taken at millimeter wavelengths, in order to obtain a more adequate test of the theory. However the 3 centimeter records were the only ones at hand having the requisite quality, and the acquisition of shorter wavelength data would have been a major undertaking, particularly since the necessary radar equipment was not immediately available.

In the following two sections we shall discuss the characteristics of the experimental data, the methods of analysis, and the results which we expect to obtain by applying these methods. The final section briefly describes the design of the analyzing equipments. A more detailed description of the associated



circuitry is deferred to Appendix A.

### 6.1 Description of the Experimental Data.

For convenience a brief description of the Angell records is given here; complete details will be found in section 3.12 of reference (2). They were obtained using a conventional pulse radar, which however incorporated two receivers fed by separate horn antennas, rigidly mounted with a five foot spacing. The received signals were recorded on magnetic tape, in the form of wide-band frequency modulation. Two types of signals were recorded simultaneously during each aircraft run, namely the envelope of the detected pulses at the output of one of the receivers, and the instantaneous phase difference between the i-f outputs of the two receiving channels, multiplied by target range. The latter quantity is a measure of the instantaneous position of an equivalent single point reflector replacing the actual highlight configuration, and is therefore referred to as "wander of the apparent radar center", or more briefly as "wander".

Both types of data were recorded for three standard flight courses and for various types of aircraft. These courses were:

(a) A radial course, with flights both toward and away from the radar. The maximum and minimum ranges were approximately 4 and  $1\frac{1}{2}$  miles.

(b) A circular course of radius 1 mile, whose center was approximately  $2\frac{1}{2}$  miles from the radar.

(c) A passing course whose point of nearest approach to radar was  $1\frac{3}{4}$  miles.

The aircraft altitudes ranged between 1500 and 2500 feet, and


speeds between 130 and 170 knots for propeller driven aircraft. In addition radial runs were taken on a jet aircraft, and finally, recordings were taken for two navy T.B.M. aircraft in formation, for both the radial and passing courses. The aircraft types which were employed in the single aircraft flights were: AT-6, AT-11 (S.N.B.), C-46, B-26, B-29 and F-84.

During the recording of these data, slow acting (4 second time constant) automatic gain control circuits were operative in both receivers. In addition, capacitive coupling was used in the recording amplifiers, thus establishing a lower half power point for the overall recording equipment of between  $\frac{1}{10}$  and  $\frac{1}{5}$  cps. The upper half power point of the equipment was around 80 cps., with a sharp fall-off in response above this frequency. Due to the fact that the d-c and low frequency components were removed from the data, it was impossible to generate the square of the envelope of the received signal from the envelope records.

About midway through the thesis research the desirability of analyzing doppler signal data (in order to compute the relative projected distribution directly) was recognized. A doppler c-w radar was available at the laboratory for the purpose, however certain ancillary equipment was also required. The development and construction of the ancillary equipment was not completed in time to provide doppler records for the experimental program.

## 6.2 Methods of Analysis.

The two major types of analyses which were performed on the recorded data were a short-time spectral analysis and a short-time probability distribution analysis. The desirability of



[REDACTED]

short-time, as opposed to long-time, analysis, has already been made clear in the theoretical treatment. Although the study of the short-time spectra and probability distributions provided information concerning the structure of the data which was not immediately evident in the unprocessed waveforms, it was found that visual inspection of the latter was in general the most effective means of detecting the presence highlight points. Accordingly, the photographs of the analyzed data which appear in Chapter 7 are accompanied by photographs of the corresponding unprocessed waveforms.

Assistance in the search for multi-point character was provided by a target simulator equipment, built by J. W. Graham of this Laboratory. The target simulator included facilities for generating idealized multi-point target signals, the number of points being adjustable from two to six. By an ideal multi-point target we mean one which is turning at a constant rate about a fixed axis, and whose highlight points have fixed amplitudes and positions, at least over several integrating intervals  $T$ . The simulator also generated the envelope, envelope squared and wander waveforms of the ideal multi-point signal. Comparison of the waveforms generated by the simulator with those appearing in the recorded data materially assisted in the search for multi-point character in the latter.

It has been shown that the short-time spectrum of the square of the envelope is the autocorrelation of the relative projected highlight distribution. Since envelope squared waveforms were not available, we would like to know what can be determined

[REDACTED]



[REDACTED]

concerning the highlight distribution from the available records, namely the envelope and wander waveforms. To do this we must study the functional expressions for these quantities. The wander waveforms obtained by Angell are represented by the function  $R \sin \varphi$ , where  $\varphi$  is the instantaneous phase difference between the two receiving channels and  $R$  is the target range. The conditions of measurement ensured that  $\varphi$  was  $\ll 1$  radian most of the time, so the above quantity closely approximated  $R\varphi$ .

In terms of reflections from the individual highlights, the expressions for the envelope and wander functions are immediately obtainable from the theory of Chapter 4. For example, the real doppler signal received at point  $O$ , midway between the two receiving horns is:

$$\text{Re} \left[ \bar{F}_O(t) \right] = \sum_{m=1}^M K_m \cos (\omega_d t - \mu_m) \quad (81)$$

where  $\omega_d$  is the doppler frequency, and, referring to Eqs. (36) and (31),

$$\mu_m = - 2k (x_m + y_m \delta_m + z_m \gamma_m)$$

To a close approximation the doppler signals received in the two channels, which we denote by  $a$  and  $b$ , are:

$$\left. \begin{aligned} \text{Re} \left[ \bar{F}_a(t) \right] &= \sum_{m=1}^M K_m \cos (\omega_d t + \mu_m + \frac{1}{2} \theta_m) \\ \text{Re} \left[ \bar{F}_b(t) \right] &= \sum_{m=1}^M K_m \cos (\omega_d t + \mu_m - \frac{1}{2} \theta_m) \end{aligned} \right\} \quad (82)$$

where  $\theta_m \approx \frac{2\pi y_m}{\lambda R}$ . As before,  $y_m$  is the projected position of the  $m$ th highlight point, the line of projection being parallel to the line joining the receiving horns. It can be shown readily that the envelopes of the signals received in channels a and b are:

$$\begin{aligned}
 |\bar{F}_a(t)| &= \left[ \sum_{m=1}^M K_m^2 + 2 \sum_{m=2}^M \sum_{\substack{n=1 \\ (m>n)}}^{M-1} K_m K_n \cos \left( \mu_m - \mu_n + \frac{\theta_m - \theta_n}{2} \right) \right]^{\frac{1}{2}} \\
 |\bar{F}_b(t)| &= \left[ \sum_{m=1}^M K_m^2 + 2 \sum_{m=2}^M \sum_{\substack{n=1 \\ (m>n)}}^{M-1} K_m K_n \cos \left( \mu_m - \mu_n - \frac{\theta_m - \theta_n}{2} \right) \right]^{\frac{1}{2}}
 \end{aligned} \tag{83}$$

and further, that the expression for wander is:

$$R \sin \varphi = R \cdot \left[ \frac{1}{|\bar{F}_a| \cdot |\bar{F}_b|} \right] \tag{84}$$

$$\left[ - \sum_{m=1}^M K_m^2 \sin \theta_m + 2 \sum_{m=2}^M \sum_{\substack{n=1 \\ (m>n)}}^{M-1} K_m K_n \sin \left( \mu_m - \mu_n - \frac{\theta_m + \theta_n}{2} \right) \right]$$

Now consider the spectra of these functions for the case of the ideal multipoint target defined above. In this case both  $K_m$  and  $\theta_m$  are constants, while  $\mu_m$  is a linear function of time, hence the doppler signals and the squares of the envelopes are seen to be sums of sine waves. The envelope has a more complicated spectrum however, since the square root operation introduces harmonics of all orders, and these tend to obscure the fundamental components.

[REDACTED]

To determine what the deteriorating effect is likely to be, consider an ideal target consisting of two points with equal amplitudes. The corresponding envelope squared has the form  $(1 + \cos \mu)$ , and the Fourier series for its square root is:

$$\left[1 + \cos \mu\right]^{\frac{1}{2}} = \frac{2\sqrt{2}}{\pi} \left(1 + \frac{2}{3} \cos \mu - \frac{2}{15} \cos 2\mu + \frac{2}{35} \cos 3\mu + \dots\right) \quad (85)$$

The amplitude of the second harmonic is  $\frac{1}{5}$ th of the fundamental amplitude, hence its energy is only  $\frac{1}{25}$ th of that of the fundamental. Since our spectrum analyzer generates the energy spectrum (i.e. - the magnitude squared of the short-time Fourier transform), it follows that the extraneous harmonic content resulting from operating on the envelope instead of its square is almost negligible. Consequently highlight resolution should not be markedly impaired thereby.

Next consider what useful information the wander waveform can yield. Referring to Eq. (84), the last bracket on the right hand side contains a sum of sine waves whose spectrum is of the desired type. However the preceding bracket contains the reciprocal of the product of two envelopes. The Fourier series expansion of the reciprocal is difficult to derive, but approximate calculations show that its harmonic content is high. The Fourier series of the product of the two brackets includes, in addition, all the harmonics produced by cross product terms of the Fourier series of the individual brackets. Consequently the possibility of resolving highlight points by spectral analysis of wander waveforms is expected to be small. This expectation is verified by the experimental analysis.

[REDACTED]

[REDACTED]

The physical interpretation of wander, namely that it represents the instantaneous apparent center of reflection of the aircraft, suggested at an early stage of the thesis that the probability distribution of the wander waveform might yield information concerning the complexity of the aircraft geometry. It was also thought that the probability distribution of the envelope would provide an estimate of the number of highlight points present, even under conditions where a spectral analysis failed to resolve them. Accordingly a theoretical study of the probability distributions of envelope, envelope squared, and wander was undertaken. The details are not important enough to record here, hence only the general conclusions are mentioned.

It should be noted that there is no satisfactory theory for determining the short-time probability distributions, which are of primary interest to us. On the assumption of a stationary process however, the long-time statistics of the envelope and its square have been evaluated in the case where the phases of the signals from the individual highlight points are uniformly and randomly distributed, and the amplitudes are constant. It is in fact the classical random walk problem in two dimensions (21). The most detailed treatment of this problem which has come to the author's attention is reference (22), where a probability distribution of amplitudes as well as phases is postulated. The results of these works show that the probability distribution of envelope approaches a Rayleigh distribution as the number of points,  $M$ , increases, and is very closely Rayleigh when  $M = 6$ . Indeed the shape of the distribution does not vary

[REDACTED]

markedly with M when the latter is greater than four.

The derivation of the probability distribution of wander is much more complicated than that of envelope, and has not been solved. One must therefore resort to experimental means to obtain it, and for this purpose the wander waveforms generated by the Target Simulator were applied to the Distribution Analyzer. The results indicate that the probability distributions of wander rapidly approach a limiting form when the number of points is increased beyond three. Hence the wander distributions are slightly less useful than those of the envelope as far as counting highlights is concerned. It is concluded that the short-time probability distributions might be of value in counting highlights when not more than four are present, however it does not appear that they will yield information concerning relative highlight positions or amplitudes.

### 6.3 Description of the Analyzing Equipments.

A primary objective which governed the design of the two short-time analyzers was that they should be capable of generating the complete short-time spectra and probability distributions of the input waveforms as continuous functions of time. This requirement necessitated the design of somewhat more complex equipment than those needed to perform the more customary long-time analyses. The author was greatly assisted in the development of these equipments by B. Easter and S. Margolis, who were jointly responsible for the design of the distribution analyzer. Brief descriptions of the overall design and functioning of both analyzers will now be presented. Detailed block diagrams, and descriptions of various circuits, are relegated to Appendix A.

### 6.31 Short-Time Spectrum Analyzer.

A photograph of the short-time spectrum analyzer appears in Fig. 20, Appendix A. A partial block diagram is shown in Fig. 9. Since this equipment consists of ten identical channels, only one channel is detailed in Fig. 9. Each channel has a transfer function similar to that of a symmetrical band-pass filter. The center frequencies of these filters can be adjusted stepwise, with increments as small as  $\frac{1}{2}$  cps., anywhere in the range from 1 to 80 cps., and filter bandwidths can be set to any one of the following four values: 1, 2, 4 and 6 cps. The center frequencies and bandwidths are set so that the skirts of adjacent filters intersect at their half power points.

The waveform to be analyzed is applied simultaneously to the ten filter inputs. The ten outputs then give a measure of the instantaneous magnitude of the energy in the input waveform which is centered respectively at each of the ten center frequencies. The output from each channel is passed through an RC filter, which permits further integration if desired. The time constant of these integrators is adjustable from  $\frac{1}{24}$  second to several seconds in ten steps. Normally this unit was used to "clean up" noise on the output waveforms from the filter channels, rather than to provide purposeful integration. It was therefore left on the minimum integrating time setting for practically all measurements.

The outputs are then presented simultaneously on an oscilloscope, by means of a sequential sampling circuit. This device takes a 90 microsecond pulse sample of each of the ten

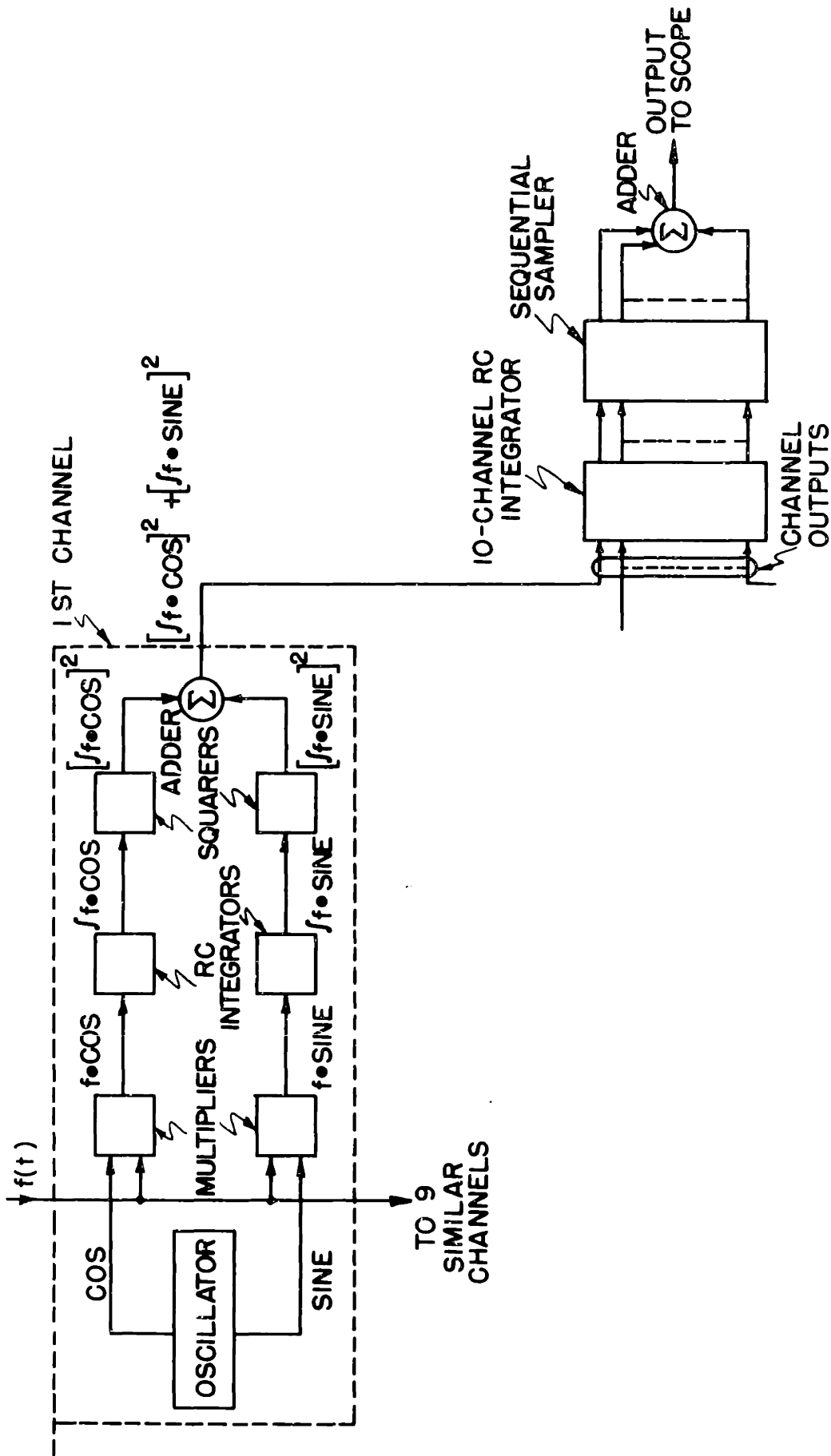


FIGURE 9.

Overall (Partial) Block Diagram of Short-Time Spectrum Analyzer.

channels in a fixed order, at a repetition rate of about 600 cps. The sampled data are added and applied to the vertical plates of the scope, while the horizontal scope sweep is synchronized to the sampler sweep. The scope presentation thus shows ten pulses side by side. The abscissa of the center of each pulse represents the center frequency of the corresponding filter.

It is evident that only a portion of the total frequency spectrum of the random waveform can be displayed at any one time. For example, a bandwidth of 40 cps. can be displayed if the filter center frequencies are spaced 4 cps. apart. This corresponds to a frequency resolution of 4 cps. If a resolution of 1 cps is desired, then a bandwidth of only 10 cps can be analyzed at once. In this regard, the equipment fails to fulfill the original design requirement of permitting the complete spectrum to be analyzed at one time. An additional ten channels would be necessary in order to cover the major part of the spectrum for the filter bandwidths usually employed, namely 2 cps and 4 cps. This would have required four additional racks of equipment however, thus resulting in prohibitive size and complexity.

Referring again to Fig. 9, the method of achieving a band-pass filter response may be explained as follows. The input waveform, denoted by  $f(t)$ , is multiplied with the quadrature outputs of an oscillator, whose frequency determines the center frequency of the equivalent filter. The two products thus obtained are passed through identical RC integrators, whose time constant determines the equivalent filter bandwidth of the channel. The outputs of the integrators are actually exponentially weighted integrals of the input products, and closely resemble



[REDACTED]

sine and cosine Fourier transforms of  $f(t)$ . These quantities are then squared and added, the sum function representing the instantaneous magnitude of the energy components in  $f(t)$  which are centered about the oscillator frequency.

### 6.32 Short-Time Distribution Analyzer.

A photograph of the probability distribution analyzer appears in Fig. 22, Appendix A. An overall block diagram is shown in Fig. 10. This equipment consists of 24 channels, thus permitting the peak-to-peak amplitude of the input waveform to be divided into 23 horizontal slices. The slicing process is carried out by flip-flops acting as fixed level selectors. The output of any one channel is a sequence of pulses of fixed amplitude, but irregular width and spacing, a pulse being present whenever the input waveform lies in the slice in question. The 23 channel outputs are then passed through RC filters, sampled sequentially, added, and displayed on a scope in the same manner as for the spectrum analyzer. The presentation is a histogram of 23 pulses, the abscissa of each pulse representing the center of the corresponding amplitude slice of the input waveform. The height of each pulse is proportional to the average time which the waveform spends in the corresponding slice. The averaging time can be varied in steps from  $\frac{1}{2}$  second to 8 seconds.

### 6.33 Remarks Concerning Short-Time Integration.

It should be noted that in both the analyzers the short-time integration is performed by simple RC filters. It is well known that this type of integration produces an exponentially

[REDACTED]

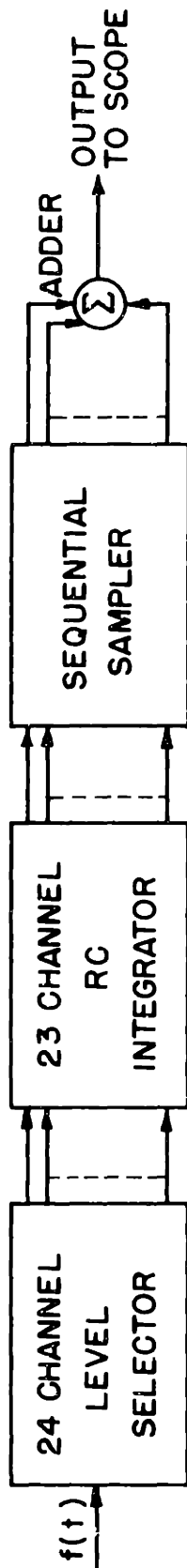



FIGURE 10.


Overall Block Diagram of Short-Time Probability Distribution Analyzer.

weighted time average of the input function over all past time. All the preceding theoretical work has assumed that ideal short-time integration was employed, that is, a uniformly weighted time average of the input function was taken over a finite interval T. The static filter response shape corresponding to ideal short-time integration is a  $\frac{\sin x}{x}$  function. It is probable that RC integration is inferior to ideal integration, as far as the resolution of highlight points is concerned. This is because the highlight configuration may change appreciably from one second to the next, due to aspect changes of the aircraft. Hence one wishes to avoid an averaging process which tails off gradually into past time, hence tending to intermix the characteristics of successive highlight arrangements. The result of intermixing will be to partially submerge the nature of any particular configuration of highlights.

The use of RC rather than ideal integration in the analyzers was dictated largely by necessity, since the synthesis of an ideal integrator involves relatively complex circuits. Specifically, the transfer function of the ideal integrator cannot be realized exactly, and the synthesis of a reasonably adequate approximation involves at least three pole pairs and three zero pairs. In addition, since we are interested in integrating times of the order of a second, it is almost mandatory to carry out the synthesis using active RC circuits with feedback. The synthesis of such circuits is at present a largely unexplored field. Some effort was devoted to the development of an ideal integrator during the course of the




research, but a satisfactory circuit was not achieved in time  
to be incorporated in the equipment.

  
CHAPTER 7EXPERIMENTAL RESULTS

We may briefly summarize the main results of the experimental work as follows. First, the prediction made in Chapter 5 that highlight resolution is possible for only a small percentage of the time at 3 centimeters is confirmed. However, the experimental finding that highlights are resolvable on at least some occasions at this wavelength leads to the conclusion that 3 centimeters lies on the upper edge of the region for which resolution is a practical reality. This result is sufficiently encouraging to warrant further experimental research in the millimeter band when the necessary radar equipment becomes available.

Secondly, the experimental studies did not reveal any significant new procedures for determining distinctive physical characteristics of aircraft beyond those covered by the theory. However it was found that the best single method for distinguishing between aircraft types was through a visual study of the unprocessed, or "raw", envelope waveforms. The probable reason that the raw waveforms yielded more information than did the short-time analyses is that the wavelength was not short enough to bring out the full potentialities of the latter. In particular the unprocessed envelope waveforms of broadside aspects of the various aircraft showed sufficient differences to permit distinction between some aircraft types. Although these distinguishing characteristics undoubtedly resulted from differences in highlight point configurations and behavior, it is to be noted that the



[REDACTED]

differences were evident even though the highlights were not generally resolvable by spectral analysis.

Before discussing the results of analysis of the Angell data, it will be useful to consider some short-time probability distribution analyses of ideal target waveforms generated by the target simulator.

### 7.1 Probability Distributions of Target Simulator Waveforms.

The target simulator was capable of simulating two types of aircraft motion. The first is the ideal motion consisting of a constant rate of change of aspect with no additional random motions or vibrations superimposed. The second is a more realistic type, consisting of random yawing about a constant mean aspect. For our purpose it is more useful to examine the ideal motion, since the theory has indicated that only under ideal conditions are we likely to obtain significant highlight resolution at 3 centimeters.

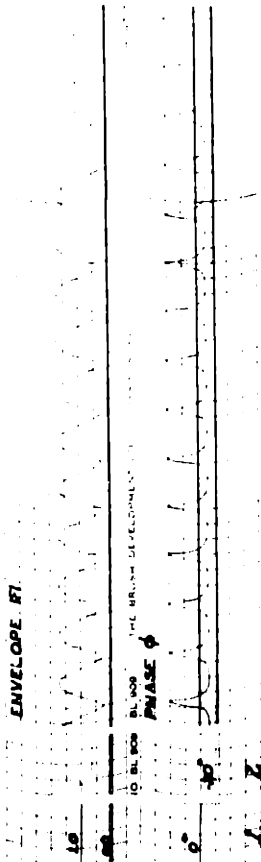
A number of pictures of ideal target data are presented in Figs. 11 and 12. They include pictures of both the raw waveforms and the corresponding probability distributions generated by the short-time distribution analyzer. Short-time spectra are not exhibited since they are not particularly significant in the ideal target case. Figure 11, which is a reprint from another report, shows samples of two, three and four point target waveforms, for both envelope and wander signals, and their corresponding probability distributions. In this case the integrating time of the distribution analyzer was 8 seconds, so that the distributions are essentially long-time, or stationary

[REDACTED]

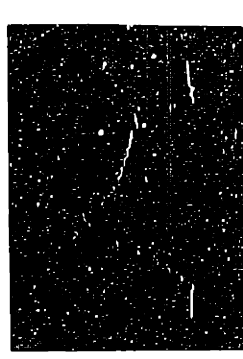


$W(\phi)$

$W(IF1)$

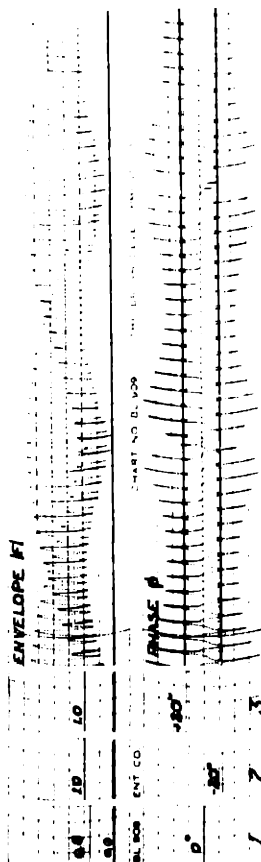


c. TWO POINT TARGET, FIXED AMPLITUDE, UNIFORM ROTATION

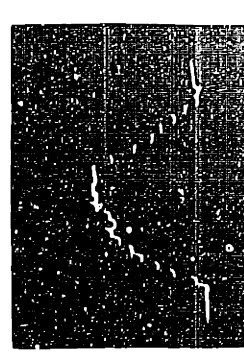


$W(\phi)$

$W(IF1)$



d. THREE POINT TARGET, FIXED AMPLITUDE, UNIFORM ROTATION



$W(\phi)$

$W(IF1)$

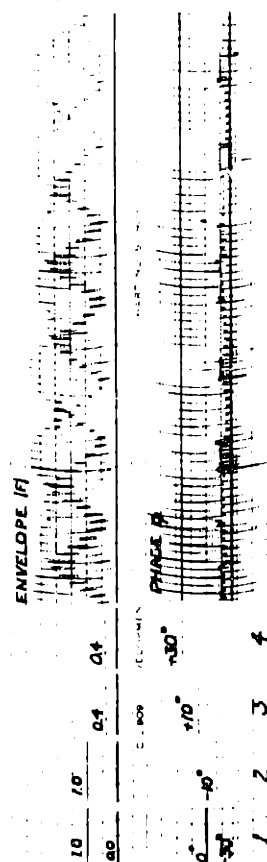


FIGURE 11. SIMULATED ENVELOPE AND WANDER DATA

[REDACTED]

ones. The raw waveforms were recorded by a dual head Brush pen recorder. The upper pen record is the envelope waveform and the lower is the wander, in each of the three examples. The relative amplitudes and spacings of the highlight points are indicated on the pen recordings. For instance, the amplitudes in the four point example are in the ratio 1 - 1 - 0.4 - 0.4. The right hand edges of the probability distributions correspond to the upper edges of the waveforms. The distributions of wander appear to the left of the envelope distributions.

It will be noted that the shapes of the envelope distributions are significantly different for the three cases shown. It will be seen later (Fig. 12) that differences are not so marked when more than four points are present. The distributions of wander are seen to approach a narrow, symmetrical peak as the number of points is increased. The wander distributions for more than four points are almost identical to that for four points. The wander waveforms are obviously more spikelike than the envelope waveforms, which indicates that their spectra have relatively higher harmonic content. This fact was previously noted in section 6.2.

It is useful to recall the nature of the spectral content of these waveforms, which was discussed in Chapter 6. It was shown, for example, that the spectrum of the envelope squared consists of the difference frequencies between all pairs of highlight points. There are therefore  $\frac{1}{2}(M)(M-1)$  frequencies for an M point target. As was mentioned in section 6.2, the harmonic content which is introduced by generating the envelope

[REDACTED]



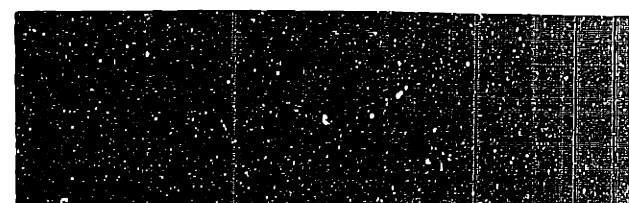
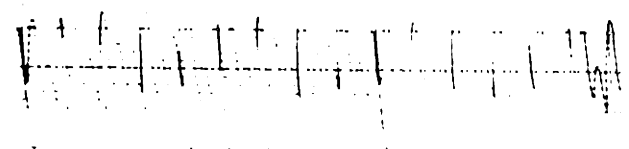
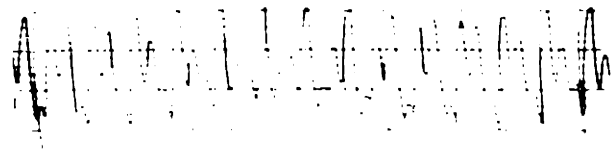
[REDACTED]

from its square is not great. Referring to the envelope waveforms in Fig. 11, the single difference frequency is readily apparent in the two point example, and the three difference frequencies can be discerned in the three point example. It is generally impossible to distinguish six separate frequencies in the four point example however.

Six more examples of simulated envelope data are exhibited in Fig. 12. Here the integrating time of the distribution analyzer was two seconds, which was the most commonly used value for the short-time distributions. The photographs of the distributions were taken on 35 mm. film, at a rate of one a second. The film speed was not the same for all examples. It ranged from  $\frac{5}{8}$  inch per second in the two lower examples to one inch per second in one of the middle examples. The paper speed of the pen recorder was one inch per second, so that the time scales of the waveforms and the distributions are in rough correspondence. The lower edges of the distributions correspond to the lower edges of the waveforms. The top two examples are envelopes of ideal three point targets, the middle two are four point, while the bottom two are envelopes of a six point target and Gaussian noise respectively. The half power bandwidth of the Gaussian noise before detection was approximately 25 cps. The upper line of figures under each picture indicates the ratio of amplitudes of the highlight points, while the lower line indicates their frequencies, one being arbitrarily designated as zero frequency. The differences between frequencies are proportional to the projected separations of the highlight points.

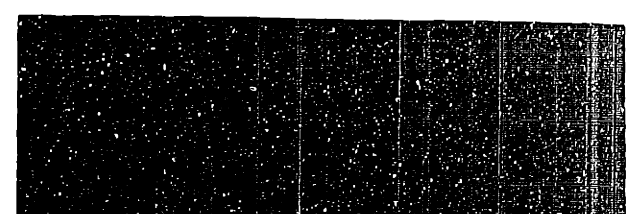
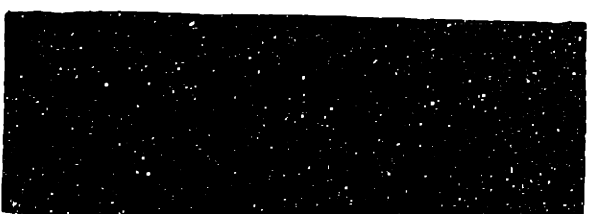
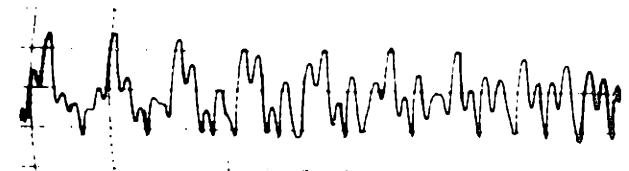
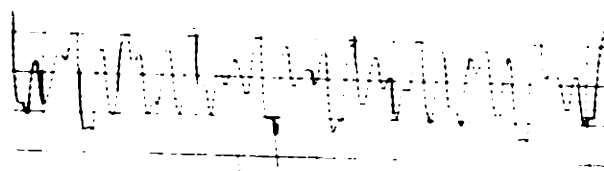
[REDACTED]

[REDACTED]



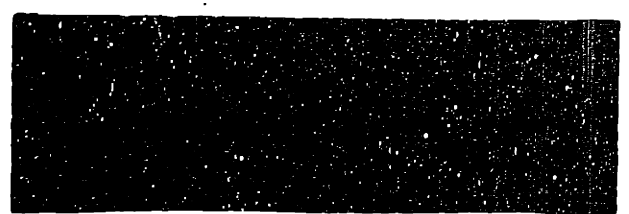
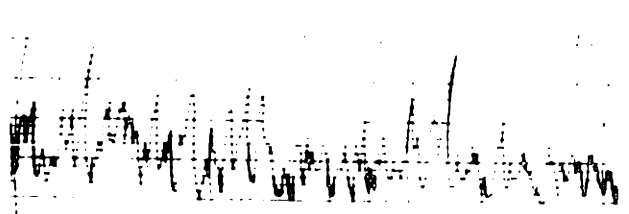
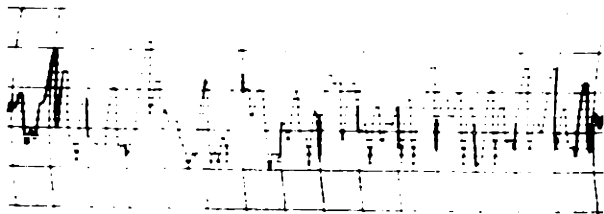
3-POINT  
| - | - |  
0 - 5.2 - 14 C/SEC

3-POINT  
| - 1/2 - |  
0 - 5.2 - 14 C/SEC



4-POINT  
| - | - 2 - |  
0 - 2.8 - 6.2 - 15 C/SEC

4-POINT  
| - | - | - |  
0 - 2.8 - 6.2 - 15 C/SEC



6-POINT  
| - | - | - | - | - |  
0 - 2 - 4 - 6.2 - 12.2 - 19 C/SEC

NARROW BAND GAUSSIAN  
NOISE

FIGURE 12. FURTHER SIMULATED WAVEFORMS AND SHORT-TIME  
PROBABILITY DISTRIBUTIONS.

Specifically, the frequency difference between two highlights is  $\Delta f = \frac{2}{\lambda} \cdot \Delta y \cdot \dot{\theta}$ , where  $\Delta y$  is their projected separation and  $\dot{\theta}$  is the rate of change of aspect, which in the ideal case is the same for every point. The frequencies used in the simulated data are representative of operational conditions at 3 centimeters. For example letting  $y = 20$  feet and  $\dot{\theta} = \frac{1}{40}$  radian/sec., then  $\Delta f = \left(\frac{2}{0.1}\right) \left(\frac{20}{40}\right) = 10$  cps.

Certain features of the probability distributions and waveforms of Fig. 12 are of interest. First it is seen that an alteration in the amplitude ratios changes the shape of the three point distribution significantly, but has much less effect on the four point distributions. Also, for a given number of points, the appearance of the waveform is markedly influenced by a change in the amplitude ratios, and, although not illustrated here, by a change in relative frequencies as well. This means that it is not always a simple matter to identify the number of points present from the distributions or the waveforms themselves. Next, it is noted that the shape of the probability distribution of a six point envelope<sup>is very similar to that</sup> of narrow-band Gaussian noise. The latter is ideally a Rayleigh distribution. The distribution of five point data is intermediate between that of four and six point, so is not shown. The final fact to note is that there are noticeable variations between consecutive probability distribution pictures corresponding to a particular waveform. These variations are even more marked when the frequency differences are nearly integral multiples of one another. Such shape variations are to be expected, because we are dealing with short-time rather than long-time

[REDACTED]

averages here.

The above brief picture of results obtained by the simulator will be sufficient to indicate its value as an aid to identifying multi-point character in the real data. We shall turn next to a discussion of the general characteristics of the recorded data, and shall later present some typical examples of multi-point behavior.

## 7.2 General Characteristics of the Experimental Data.

The purpose of this section is to discuss the main features of the recorded waveforms. It will be pointed out that certain portions of the data are of much greater value than others in revealing multi-point character. It will also be shown that, under restricted conditions, the unprocessed envelope waveforms are sufficiently distinctive to permit one to distinguish between different aircraft types.

Previously we concluded that resolution possibilities are best when aircraft motion approximates the ideal motion referred to previously, and when propeller modulation is absent. We also concluded that envelope data are of more value than wander data in revealing multi-point character. These conclusions are borne out by the experimental studies. Envelope and wander waveforms for all of the three types of flight courses described in section 6.1 were recorded on paper for visual inspection, and were also processed by the two analyzers. It was found that the return signals for the radial course were nondescript in appearance, and heavily masked by propeller modulation. In contrast, the circular courses were expected to yield fairly


[REDACTED]

[REDACTED]

ideal data over that portion of the course for which the aircraft were nearest to the radar, thus presenting a "turning broadside" aspect. This expectancy was based on the fact that the average rate of change of aspect for this portion of the circular course was about five degrees per second, which is appreciably higher than the expected average rates of yaw and roll. Unfortunately the quality of the recorded signals for the circular courses was too poor to be usable, in all except one case. Consequently these waveforms could not be used for comparative purposes.

The data for the passing courses were all of good quality however, so attention was focussed on a comparative study of these. Since propeller modulation was generally negligible within  $\pm 25$  degrees of broadside, only data within these limits were analyzed. As it is customary to measure azimuthal angles starting from the nose of the aircraft, the region of interest is therefore the interval 65 to 115 degrees. Calculations show that the maximum rate of change of aspect on the passing courses was about  $1\frac{1}{2}$  degrees per second, which occurred when the aircraft aspect was 90 degrees. This rate is of the same order as the expected average roll rate. Consequently roll (and yaw) caused greater departures from ideal motion on the passing courses than on the circular courses, indicating that the latter data were to be preferred, had they been of acceptable quality.

Figure 13 exhibits the envelope waveform of a typical passing run for each of the five propeller driven aircraft. The waveforms are ordered in the figure so that the top one corresponds to the largest aircraft measured, the aircraft size decreasing as one proceeds to the bottom of the figure. A time



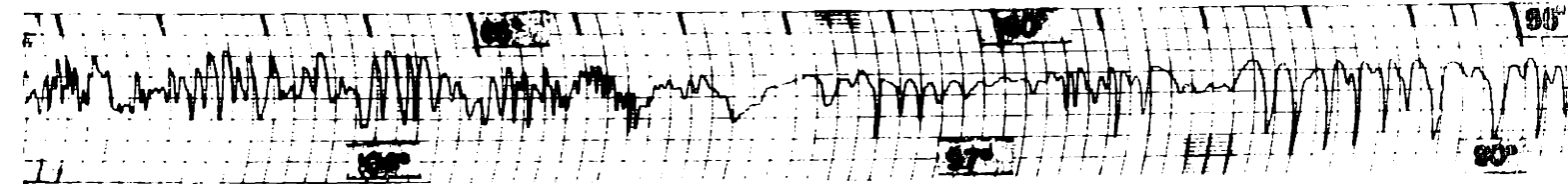
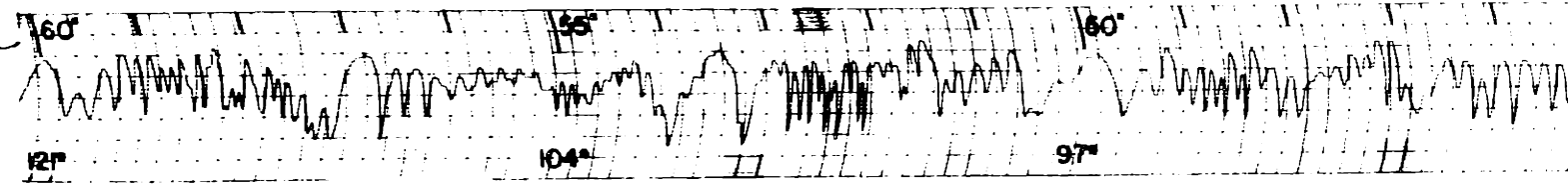
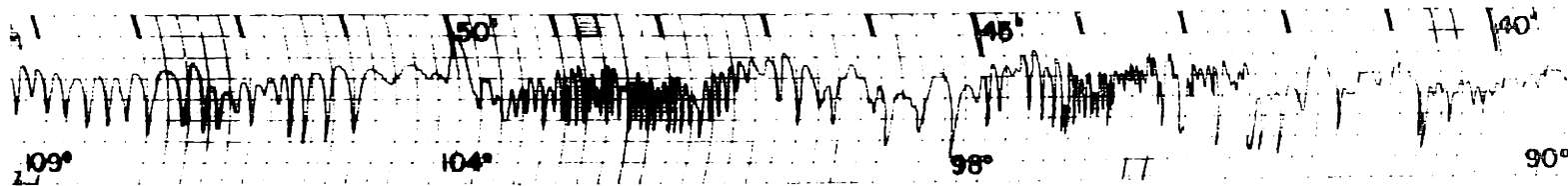
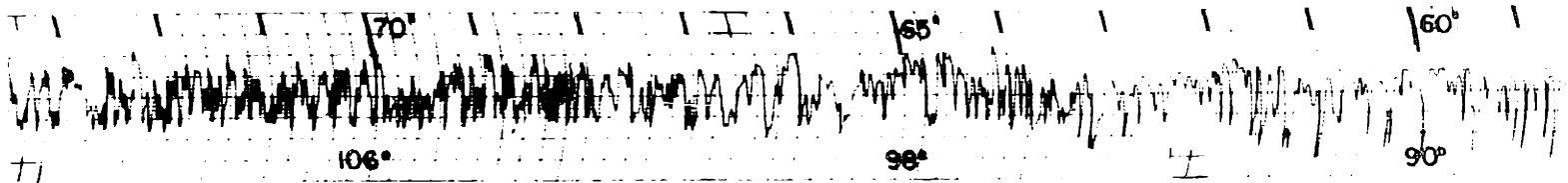
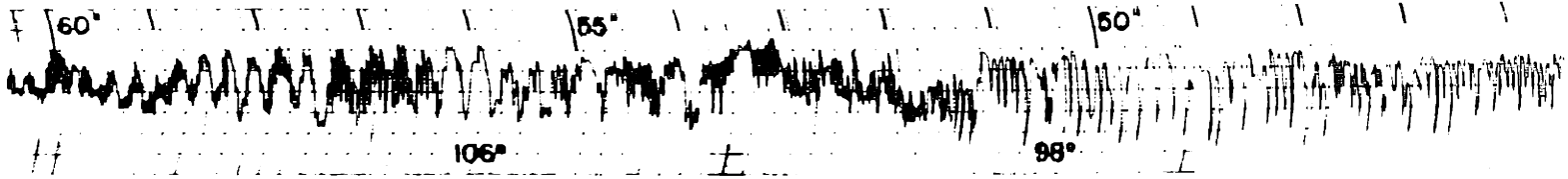
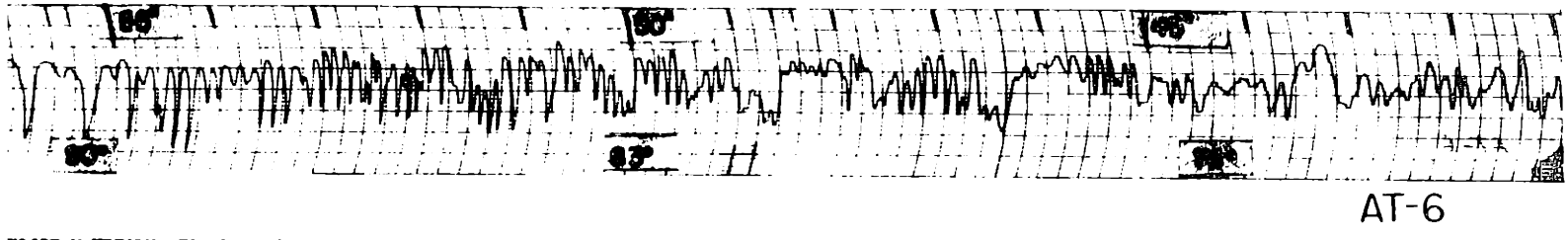
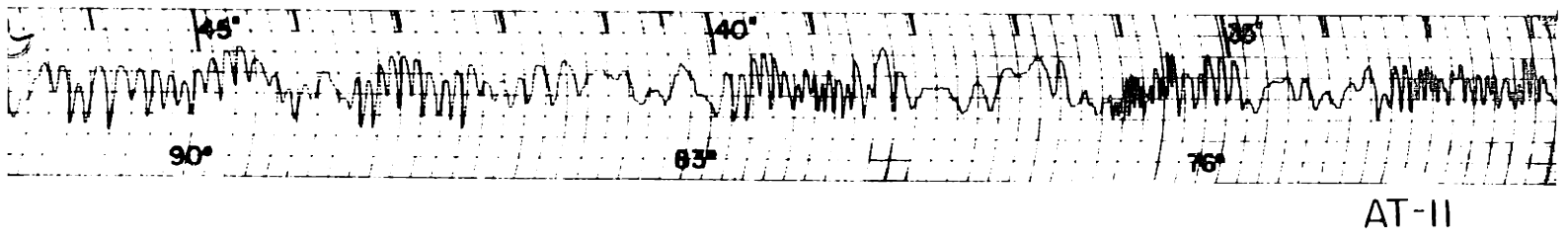
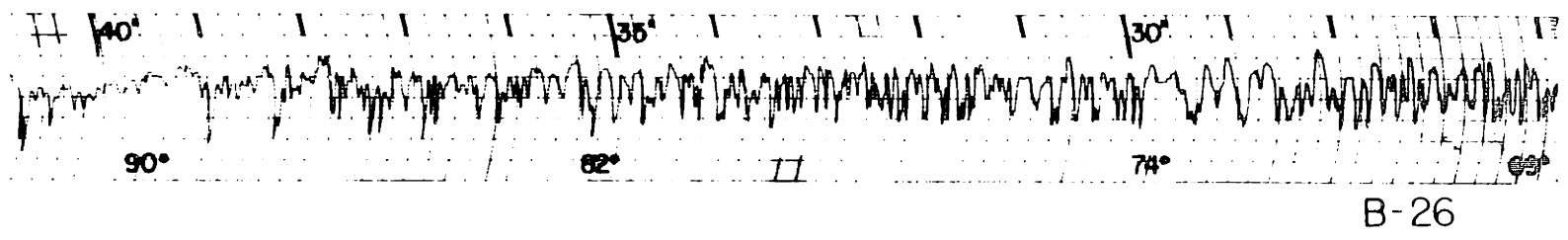
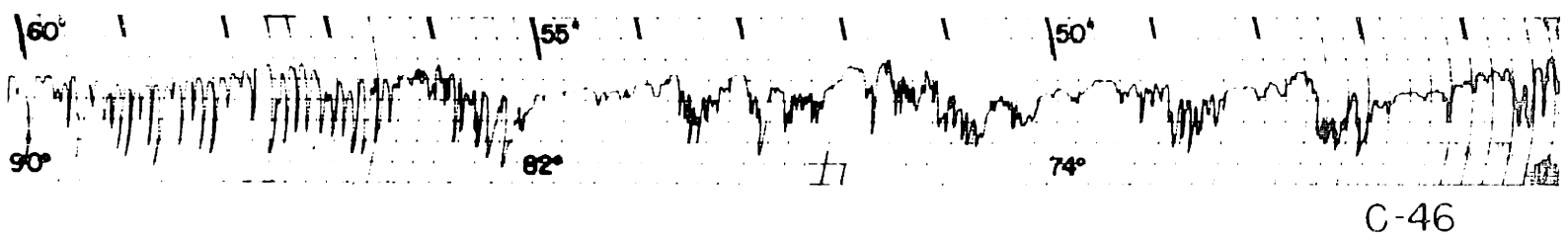
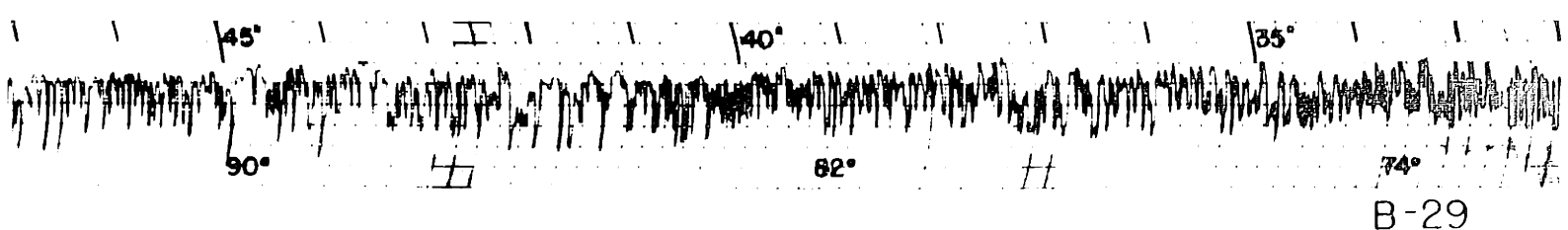
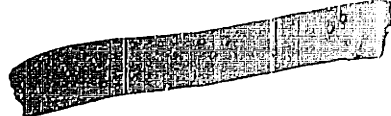


FIGURE 13. TYPICAL ENVELOPE WAVEFORM.





WAVEFORMS FOR PASSING RUNS.



scale in seconds is recorded above each waveform, while a scale of azimuth angle is recorded below each. The azimuth scale is extremely crude because careful records of instantaneous aspect were not kept. Consequently the aspect had to be reconstructed from meager records of aircraft range versus time. Moreover, the pilots were not asked to fly precise straight line courses, so that heading corrections of as much as ten degrees may have been made during flight. For these reasons the probable error in the azimuth figure is of the order of ± five degrees.

The distinctive characteristics in these waveforms which are pointed out below were found to appear consistently in every one of the six or eight passing runs which were recorded for each aircraft. The outstanding characteristics are as follows.

(1) B-29. The envelope waveform of this aircraft contains the most variations per unit aspect angle for two reasons. It is the largest of the five aircraft, and it has the most complex geometry. (It is the only four engined one of the group.) In the azimuth interval 70 to 90 degrees its waveform appears to exhibit primarily four point character. This is followed by two point character in the region 95 to 98 degrees, and later by three point character in the interval 103 to 107 degrees.

(11) C-46. One of the distinctive characters of the return from this aircraft is the appearance of quiescent regions in the interval 70 to 90 degrees. These are probably produced by the predominance of a single highlight point, whose envelope would be ideally a constant if its amplitude were constant.



The region from 90 to 100 degrees is characterized by rather degenerate two point behavior, and this is followed by a marked increase in waveform complexity between 102 and 108 degrees, considered to be mainly four point behavior. None of the other aircraft exhibited this complex waveform at aspects beyond 90 degrees.

(iii) B-26. This waveform exhibits predominantly two point behavior throughout, but particularly in the interval 93 to 115 degrees. There is also a short interval which is dominated by a single point, at about 90 degrees.

(iv) AT-11 and AT-6. These two waveforms are the most alike of the five, and are therefore considered together. The AT-11 waveform exhibits predominantly two point character, mixed with three point from 70 to 110 degrees. The AT-6 waveform is also mainly two and three point, but of a more degenerate character. In addition, the AT-6 shows a marked predominance of single point behavior between 92 and 100 degrees. This feature provides the primary means of distinguishing it from the AT-11.

Upon first inspecting the waveforms of Fig. 13, the reader's reaction may be that the point character delineated above is not immediately obvious. It is undoubtedly true that an extended study of the waveforms is necessary in order to readily perceive the essential multi-point characteristics. It is also true that the ability to distinguish between the aircraft types from these waveforms is in large measure due to the fact that the flights of all five aircraft were essentially identical with respect to speed, height and course relative to the radar. Thus

approximately the same interval of aspect was presented by each type, and approximately on the same time scale. Another assisting factor was that a large aspect interval, namely 50 degrees, was compared in each case. If a much smaller interval had been available for comparison, the distinctive characteristics of each aircraft type would not be so evident. In view of the above remarks, undue significance should not be attached to the identification possibilities noted here. However the essential conclusion is that distinctive differences in highlight configurations do exist, and can be observed under favorable flight conditions. The distinctiveness should of course be enhanced as the radar wavelength is decreased and the highlight character becomes more clearly delineated.

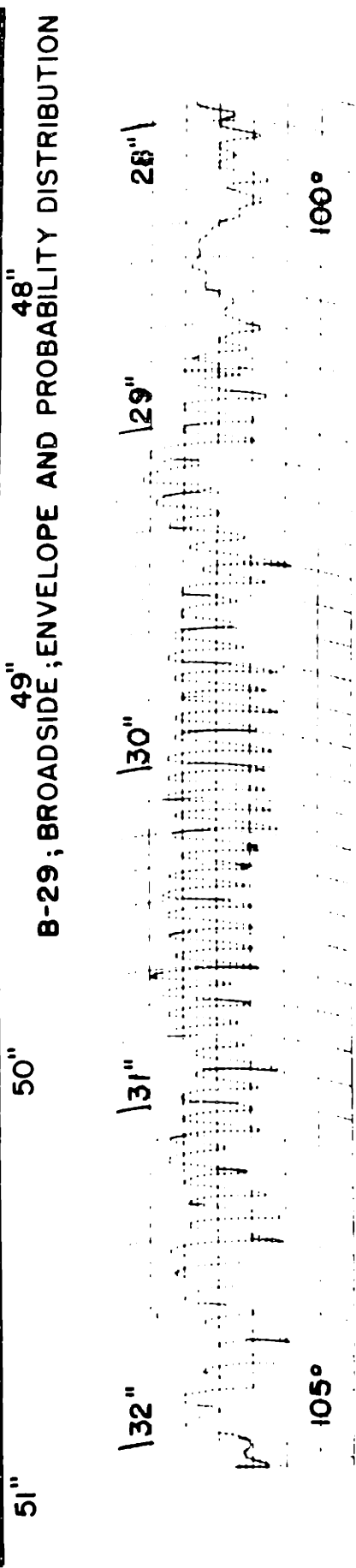
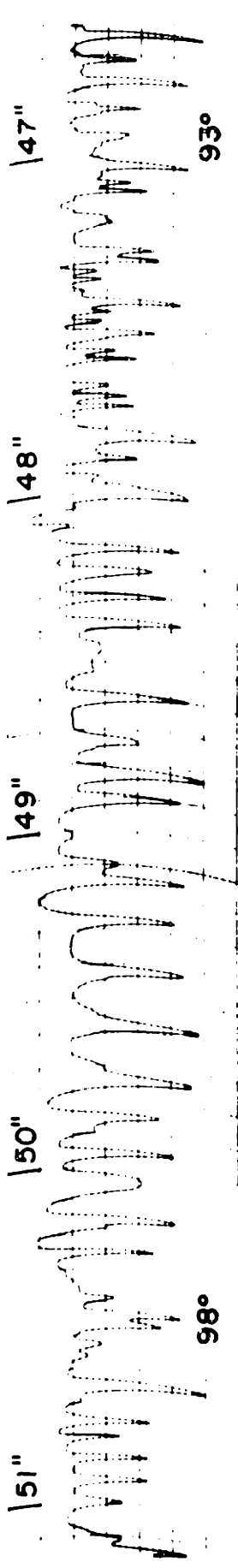
### 7.3 Examples of Multi-Point Behavior, and Other Results.

We now consider specific waveform samples which exhibit multi-point character, in order to evaluate the effectiveness of the short-time spectral and probability distribution analyses in aiding highlight identification. In addition, some miscellaneous results of interest are discussed.

Five examples of multi-point waveforms are shown in Fig. 14 to 17 inclusive. Two cases of two point behavior are shown in Fig. 14, a three point example appears in Fig. 15, while Figs. 16 and 17 are cases of predominantly four point behavior. In all these figures, time scales in seconds are included so that specific features in the unprocessed waveforms may be identified with those of the short-time spectra and probability distributions.

Figure 14 shows two point data from a B-29 and a B-26. The integrating time of the distribution analyzer for the B-29 example was one second, and the pictures were taken at a rate of two per second. The shape of the distributions should be compared with that of the simulated two point sample in Fig. 11. The main difference is that the B-29 distributions tend to approach zero rather than a finite level on the low amplitude side of the envelope. This is because the valleys in the B-29 waveforms are not all in line as they are in the simulated two point envelope. The B-26 example is included in order to illustrate the single spike in the short-time spectrum, corresponding to the difference frequency between the two highlight points. In this example the spectrum analyzer was set up to cover the frequency band 4 to 22 cps, in two cps steps. The pictures were taken at a rate of three per second. The low frequency end of the spectra occurs at the upper edge of the photographs. The reversed sense of the spectra is due to the fact that the output of the spectrum analyzer produced downward deflections on the oscilloscope which was photographed. It is seen from the spectra that, at time 30 seconds, the frequency spike is centered at about 16 cps. A count of the number of valleys in the waveform, over a one second time interval (from  $29\frac{1}{2}$  to  $30\frac{1}{2}$  seconds) confirms the analyzer's frequency measurements.

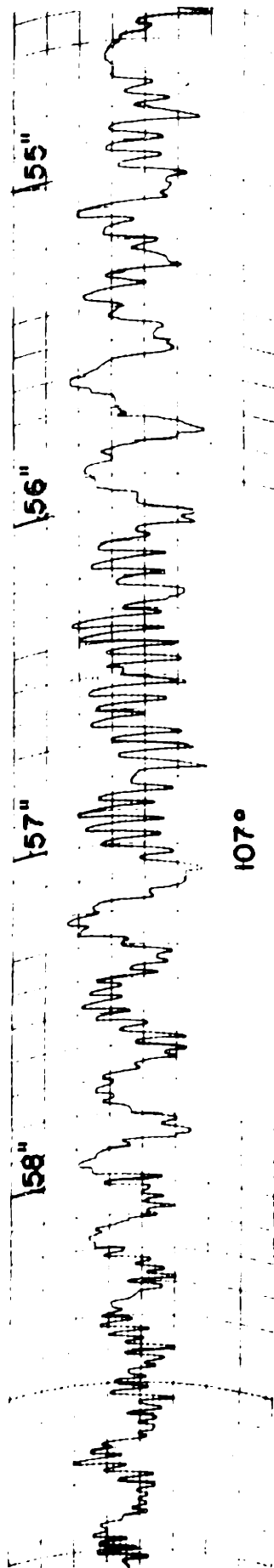
The three point example from Fig. 15 is also taken from a B-29 flight. The integrating time of the distribution analyzer was one second, as before. The spectrum analyzer was set to cover the band 10 to 46 cps in four cps steps. The pictures were



B-29; BROADSIDE; ENVELOPE AND PROBABILITY DISTRIBUTION

B-26; BROADSIDE; ENVELOPE AND SPECTRUM

FIGURE 14. TWO EXAMPLES OF TWO POINT BEHAVIOR.

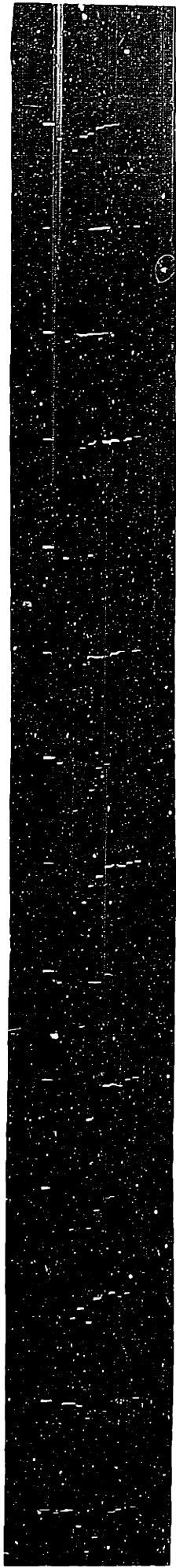


B-29, BROADSIDE ENVELOPE



58'' 57'' 56'' 55''

PROBABILITY DISTRIBUTION



57 1/2'' 57'' 56 1/2'' 56'' 55 1/2''

SPECTRUM

FIGURE 15. AN EXAMPLE OF THREE POINT BEHAVIOR.

taken at rates of two and six per second for the probability distributions and spectra respectively. As in the previous figure, the low frequency end of the spectra is uppermost. Although the waveform exhibits crude three point behavior throughout its entire length, the clearest three point behavior occurs between times 56 and 57 seconds. The probability distributions corresponding to this portion are the fourth and fifth pictures from the beginning of the strip. These are very similar in shape to the distributions appearing in the upper right hand photograph in Fig. 12. The corresponding simulated and real waveforms are also quite similar.

From a visual inspection of the waveform of Fig. 15, coupled with an application of the theory of Chapter 4, it is deduced that the three fundamental difference frequencies in the section 56 to 57 seconds are 4, 16 and 20 cps. These values are arrived at as follows. There are seen to be 4 slow beats and 20 fast beats in this one second time interval. The amplitude of the fast beat is almost three times that of the slow beat. These facts fit in with the assumption that the highlight points have relative amplitudes  $1 - \frac{1}{3} - 1$ , and relative frequencies  $0 - 4 - 20$  cps. The corresponding difference frequencies are therefore  $(4 - 0) = 4$  cps,  $(20 - 4) = 16$  cps, and  $(20 - 0) = 20$  cps., and the corresponding spectral amplitudes are  $(1 \times \frac{1}{3}) = \frac{1}{3}$ ,  $(1 \times \frac{1}{3}) = \frac{1}{3}$  and  $(1 \times 1) = 1$ .

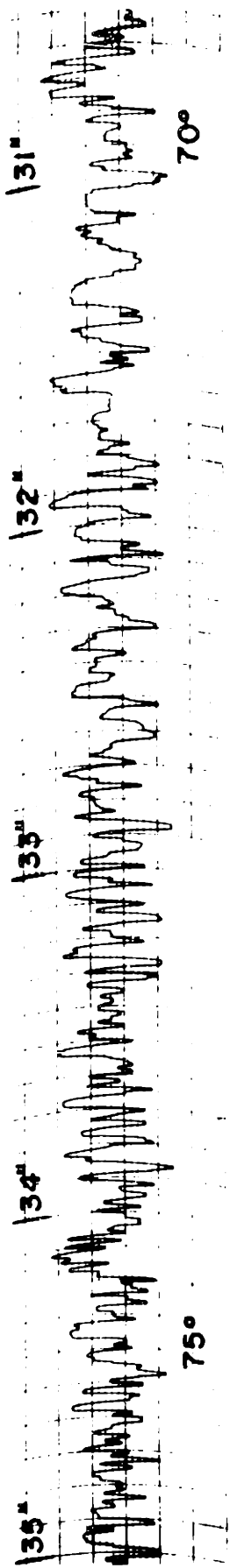
We now enquire whether the short-time spectra confirm the above frequency estimates. There is seen to be a fairly broad hump in the one second time interval in question. The peak of

[REDACTED]

the hump occurs between 18 and 20 cps. Evidently it is produced by the 16 and 20 cps. components together, the latter being the dominant one because of its larger amplitude. The analyzer was unable to resolve the two components in this case. Since the analyzer's frequency band was set to cover 10 to 46 cps in this example, the four cps component therefore does not appear. The spectrum which appears at time  $57\frac{1}{6}$  seconds should be ignored, because it includes spurious responses caused by temporary overload of the spectrum analyzer. The conditions under which this equipment can be overloaded are discussed in Appendix A.

Figure 16 exhibits a sample of four point data, again from a B-29 flight. On comparing the envelope waveform with those generated by the simulator, one might conclude that the number of highlight points present is between four and six. However the probability distributions which appear at times 33,  $33\frac{1}{3}$  and 34 seconds are definitely four point in shape, as will be seen on comparison with the four point distributions in Fig. 12. In this example, therefore, the probability distribution yields a better estimate of the number of highlights than does the waveform. The band covered by the spectrum analyzer is again 10 to 46 cps. A study of the spectra indicates that highlight resolution is not generally successful in this case. For if resolution were adequate, we would expect to see six difference frequencies when four highlights are present. The closest approach to this number occurs at times  $33\frac{1}{2}$  and  $33\frac{2}{3}$  seconds, when four peaks are visible. There is a similar amount of activity in the neighborhood of 35 seconds, while at 34 seconds two peaks are predominant. It is to be noted that a given

[REDACTED]



B-29; BROADSIDE ENVELOPE



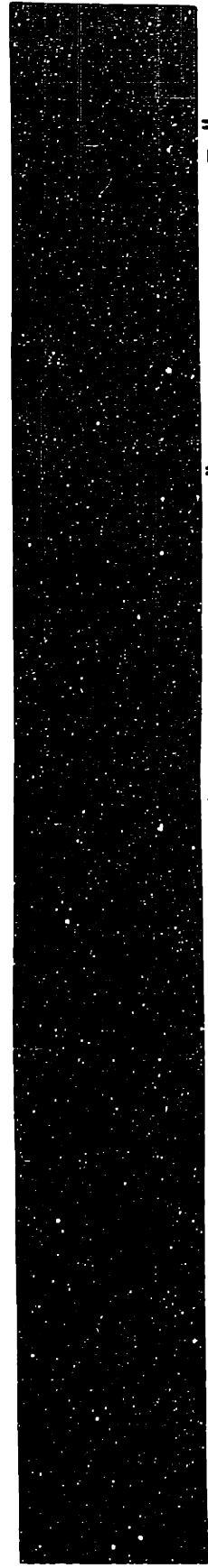
31"

PROBABILITY DISTRIBUTION

33"

34"

35"



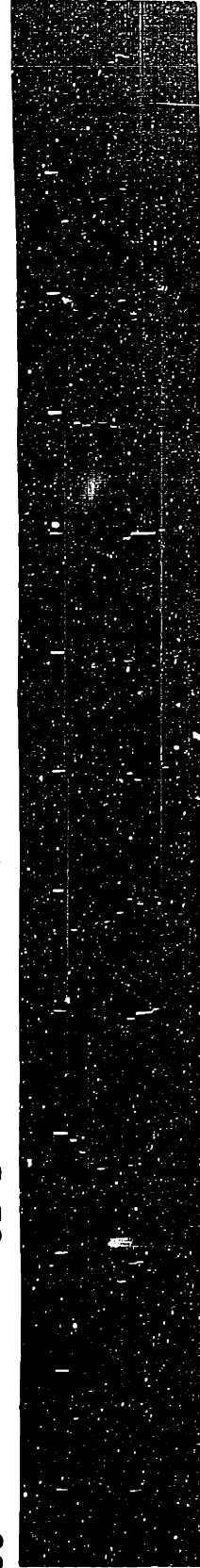
31"

31 1/2"

32"

32 1/2"

33"



33 1/2"

34"

34 1/2"

35"

SPECTRUM

FIGURE 16. PROBABLE FOUR POINT DATA FROM A B-29.

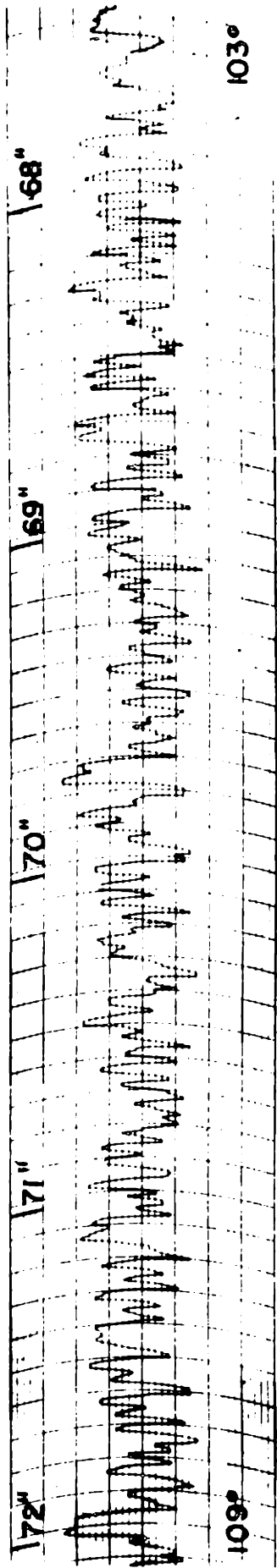


spectral pattern rarely lasts more than two consecutive pictures, or  $\frac{1}{3}$  second. This corresponds to an aspect change of approximately  $\frac{1}{2}$  degree, which may appear to imply that the highlight configuration can change appreciably for  $\frac{1}{2}$  degree change of aspect. One should be cautious about drawing such a conclusion from the spectral patterns however, because it is difficult to correlate the variations in the highlight configuration with the transient response which they induce in the filters comprising the analyzer.

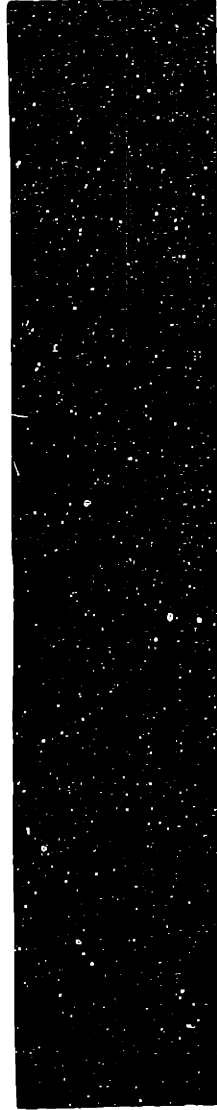
Another four point example, taken from a C-46 flight, appears in Fig. 17. The integrating time of the distribution analyzer was two seconds, and one picture per second was taken. The spectrum analyzer covered the band 4 to 22 cps, in two cps steps. Three spectral pictures per second were taken. All the distribution shapes are seen to be reasonably close to the ideal four point shapes which appear in Fig. 12. As in the preceding example, the spectra do not exhibit the expected six peaks. It is of course possible that some of the frequency components lie outside the band being analyzed. As before, there is usually an appreciable change in spectral shapes over successive  $\frac{1}{3}$  second intervals. However there is occasional evidence of frequency components with longer persistence than this. For example, a spike at 22 cps (at the lower edge in the pictures) is seen to persist from  $68\frac{1}{3}$  seconds to  $69\frac{1}{3}$  seconds.

The primary conclusions which are drawn from the above study are as follows:

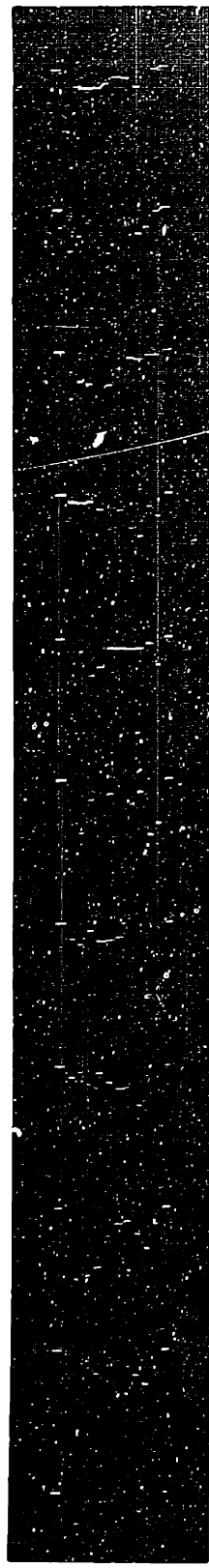
- (1) The presence of two and three highlight points is fairly easily recognized at 3 centimeters, both from the unprocessed



**C-46; BROADSIDE ENVELOPE**



72" 71" 70" 69" 68" 67"  
**PROBABILITY DISTRIBUTION**



70" 69" 68"  
**SPECTRUM**

FIGURE 17. ANOTHER FOUR POINT EXAMPLE, FROM A C-46.

[REDACTED]

envelope waveforms and from the probability distributions. Spectral analysis invariably exhibits an appropriate spike in the two point case, and can sometimes resolve spikes in the three point case.

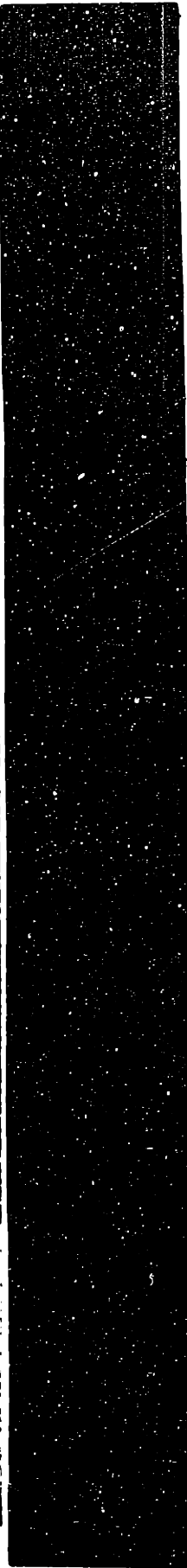
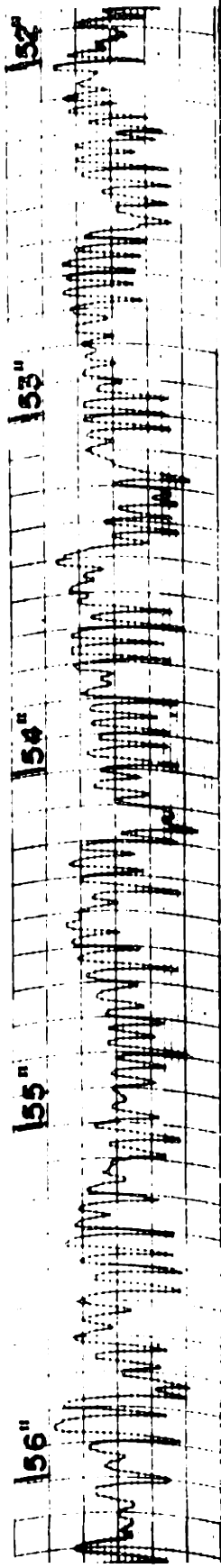
(ii) When four highlights are present, it is virtually impossible to determine the number from the unprocessed waveform, because of its complexity. The shape of the probability distribution provides the most reliable means of estimating the number in this case. The spectrum evidently does not yield adequate resolution for four points.

(iii) While no examples of more than four points were detected in the data, it is believed that highlight resolution and counting would not be successful for envelope data at 3 centimeters.

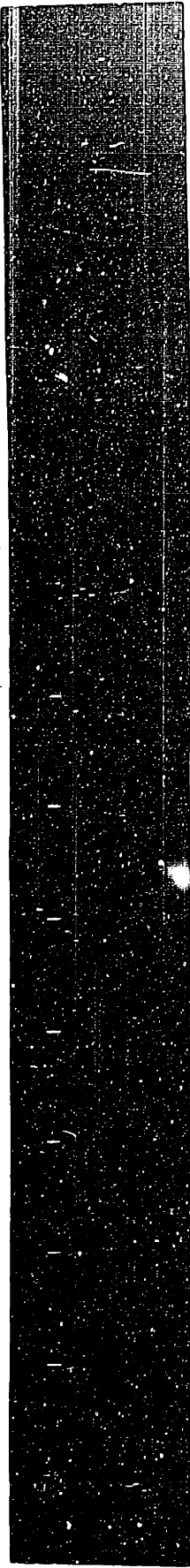
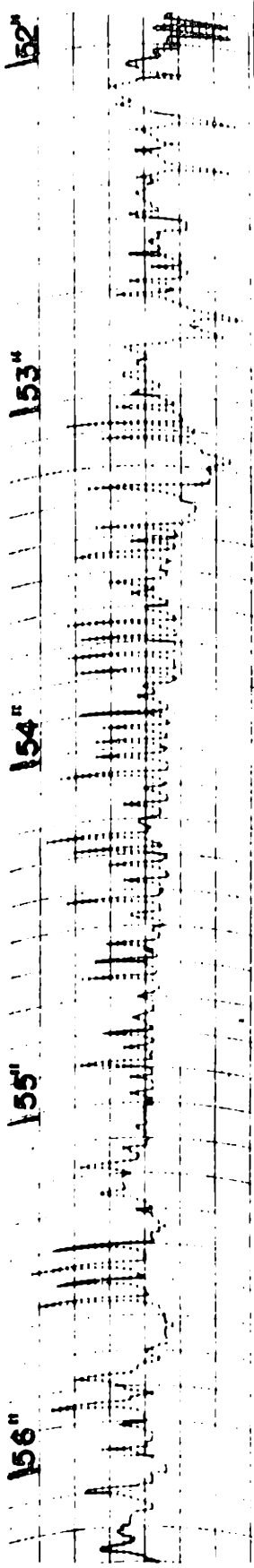
To conclude this section, two additional results of interest are mentioned. The first is a comparison of the spectra of envelope and wander waveforms. The purpose of the comparison is to confirm the theoretical prediction that the wander spectrum has a greater harmonic content than the envelope spectrum, thus making it less suitable for resolving highlights. Figure 18 presents simultaneous recordings of envelope and wander waveforms, and their associated spectra, for a circular flight by an AT-11 aircraft. The aspect is near broadside, so that the waveform has predominantly two point character. The analyzer covered the band 10 to 46 cps in four cps steps. Due to a sense reversal which inadvertently occurred in producing the contact print of the envelope spectra, the upper edge of this print corresponds to the high frequency end of the spectrum.

[REDACTED]

[REDACTED]



55" 54 1/2" 54" 53 1/2" 53  
 AT-11; BROADSIDE TURNING; ENVELOPE AND SPECTRUM

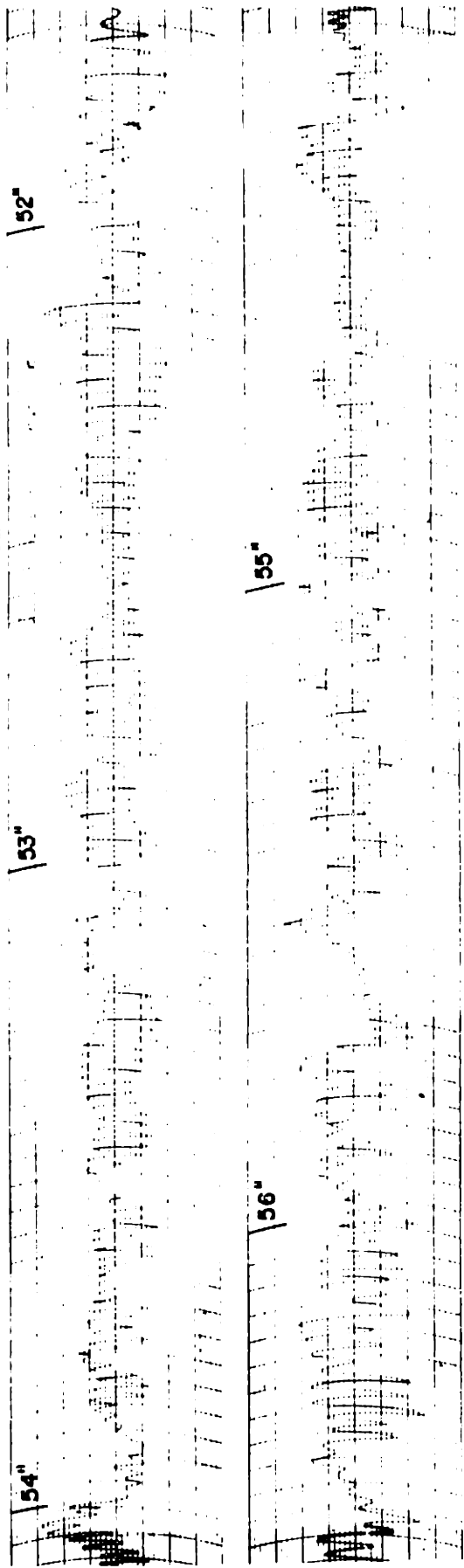


55" 54 1/2" 54" 53 1/2" 53"  
 AT-11; BROADSIDE TURNING; WANDER AND SPECTRUM

FIGURE 18. COMPARISON OF THE SPECTRA OF ENVELOPE AND WANDER.

The print of the wander spectra has the same sense as the previous pictures however, namely the upper edge corresponds to the low end of the spectrum. With this fact in mind, it is seen that the main peak in the envelope spectra occurs at about 22 cps for most of the pictures, and there is no appreciable evidence of second harmonic. In contrast, the corresponding peak in the wander spectra is not always present, and when present, is generally less well defined, mainly due to the appearance of appreciable energies at neighboring frequencies. Also, the second harmonic of 22 cps appears in a number of the wander spectra. It is particularly evident in those occurring at times  $53\frac{1}{6}$ ,  $53\frac{5}{6}$  and 54 seconds, and appears to a lesser extent in all the spectra between 54 and 55 seconds.

The second result of interest is the return signal from two aircraft in formation. Figure 19 presents a small section from a passing run of two T.B.M. aircraft, in which one was flying directly behind the other. There is inevitably a small amount of relative maneuvering of aircraft in a formation, which produces doppler difference frequencies in the envelope waveform. In the example shown, a high pass filter was used to eliminate most of the spectral energy lying below 15 cps, in order to accentuate the doppler beat frequency between the two aircraft. The spectrum analyzer covered the band 18 to 72 cps in six cps steps, and pictures were taken at a rate of six per second. The doppler difference frequency is seen to be about 20 cps at time  $51\frac{1}{2}$  seconds, and increases to 70 cps at 54 seconds. It remains in the region of 60 to 75 cps until 56 seconds, and



TWO T.B.M. ; BROADSIDE ; ENVELOPE




TWO T.B.M. ; BROADSIDE ; SPECTRUM

FIGURE 19. EXAMPLE OF DATA FROM TWO AIRCRAFT IN FORMATION.

then decreases again. Rates of change of frequency of 30 cps per second are observed to occur, and it is seen that the spectrum analyzer follows the changes in a reasonably adequate manner. Sudden changes in the amplitude of the waveform cause some broadening of the spectra. An outstanding example of this occurs at time  $56\frac{1}{3}$  seconds. In general it was found impossible to observe the multi-point character of the individual aircraft when they were in formation. This is to be expected because, with a conventional radar it is impossible to obtain azimuthal resolution of the highlight points of separate aircraft, as can be done with a multireceiver radar.

In addition to the work described above, at least two other types of experimental analysis were attempted, but these did not yield useful results. One was a zero crossing analysis of the envelope waveforms of the passing runs. Another was to apply corresponding envelope and wander waveforms respectively to the horizontal and vertical plates of a long persistence cathode ray tube, in order to detect correlation between these two waveforms. The probable reason for the failure of this experiment is that the two waveforms in question were recorded on separate tapes, hence it was impossible to achieve a sufficient degree of time synchronization between them to bring out the expected correlation effects.

In summary, the experimental work has shown that multi-point behavior is apparent at a wavelength of 3 centimeters, and that highlight resolution by spectral analysis is achievable in some circumstances. The results also indicate that the return signals



from different aircraft types are sufficiently distinctive to permit them to be distinguished under favorable operational conditions. If 3 centimeter doppler data had been available for analysis, it is likely that the possibilities of highlight resolution would have shown to better advantage than was the case with the envelope waveforms.






SUMMARY, AND SUGGESTIONS FOR FURTHER RESEARCH8.1 Summary of the Main Results.

We have been studying ways to obtain information concerning the surface geometry and motion of aircraft in flight by suitable analysis of microwave radar return signals, the ultimate objective being to recognize various aircraft types. The first step of the research was the realization that at microwavelengths, the total information concerning the geometry and motion is contained in the sequence of instantaneous highlight configurations. Hence the problem of aircraft recognition by radar can be divided into two phases; the first is to find methods of determining highlight configurations, and the second is to evaluate the possibility of distinguishing aircraft types from these configurations. The thesis research was confined entirely to the first phase.

For distant aircraft, we next showed that the projected highlight distribution is given approximately by the Fourier transform of the received field over an aperture. (Chapter 2). This result is not particularly original, since it has been known for some time in optical theory that the field over the image plane of a lens is the Fourier transform of the field over the lens aperture. The main contribution here was the recognition that the phenomenon of highlight variation versus aspect angle invalidates the Fourier relation at longer wavelengths and prevents determination of the highlight distribution. The obvious way of minimizing this undesirable effect is to



make the aperture sufficiently small so that highlight positions and intensities are essentially constant over it. This in turn requires use of a short wavelength in order to maintain the ratio of aperture dimension to wavelength sufficiently large to provide adequate highlight resolution. As a logical deduction from the above considerations, it was proved that the projected highlight distribution can be obtained as exactly as desired from the Fourier transform of the received field, by letting both the aperture dimension and the wavelength approach zero.


Next, the Fourier transform relation was used as the basis of design proposals for multireceiver radar systems which determine one-dimensional projections of the highlights (Chapter 3). It was concluded that a system for determining the projected distribution directly is not feasible at present, but a system for determining the autocorrelation was found practicable. Derivation of the highlight distribution from its autocorrelation was shown to be possible under suitable conditions (Appendix B), thus enhancing the value of the latter system.

The possibilities of obtaining highlight information with a conventional radar were thoroughly studied in Chapter 4, and it was shown that a "relative" one-dimensional projected distribution, and its autocorrelation, could be determined. Certain limitations to the operational conditions under which the former function is obtainable were discussed, while the latter function was seen to be derivable under all conditions. Collaterally, consideration was given to the possibilities of

determining the characteristics of random aircraft motion, flexural vibrations and propeller rotation at short micro-wavelengths. It was concluded that the first two effects would be more easily detected with conventional radars, while the latter would reveal its characteristics more clearly in the multireceiver systems.

In Chapter 5 a method was presented for determining the maximum permissible wavelength for the resolution of highlights having a prescribed minimum spacing, when the effects of highlight variation with aspect were taken into account. The method was general enough to cover the case of a conventional radar. It was shown later that the general results could be specialized to apply to multireceiver systems. The wavelength predictions were not accurate in the latter case however, due to an approximation in the analysis which was unjustifiable in the multireceiver situation. Numerical calculations indicated that a wavelength of not more than 2 or 3 millimeters must be used to obtain adequate resolution with a conventional system. It was estimated that similar resolution might be obtained at 5 to 6 millimeters with multireceiver systems.

The experimental work, whose primary objective was to check the above theory, consisted of analysis of 3 centimeter data. It was found that highlight resolution was possible only very occasionally at this wavelength, which is in agreement with the theoretical predictions of Chapter 5. However the fact that highlights could be resolved at all indicated that 3 centimeters is on the upper edge of the wavelength region in which resolution is practicable. Another significant result was that it was




possible to distinguish several different aircraft types for broadside viewing aspects, this despite the fact that highlight resolution was far from adequate. The distinctive characteristics of the return signals would undoubtedly have stood out more clearly had the wavelength been appreciably shorter than 3 centimeters.

## 8.2 Suggestions for Further Research.


The most obvious requirement for further research is that of obtaining more adequate experimental verification of the theoretical results. It is most desirable that experiments be carried out at millimeter wavelengths, where highlight resolution is achievable for a reasonable percentage of the time. It is believed that the use of a conventional radar at about 5 millimeters will provide an adequate test of the theory provided measurements are made on aircraft executing the idealized motion described in section 5.3. To approximate ideal motion, a suitable flight course would be a circle whose radius is appreciably smaller than the distance from its center to the radar. Non-turbulent atmospheric conditions would be required, in order to minimize random motions and flexural vibrations, and the bank angle should be kept as constant as possible since sudden changes in the latter will impair the desired constancy of rate of change of aspect. If good resolvability is achieved with a conventional radar at 5 millimeters, equally good performance would be ensured for a multireceiver radar at this wavelength.

The possibility of recognizing different aircraft types



from their highlight configurations depends on whether the latter differ significantly from one type to another for corresponding viewing aspects. A simple and yet reasonably effective way of comparing highlight configurations is by photographing highly polished aircraft models which are illuminated by a narrow light beam in a darkened room. This method will yield the projected highlight positions accurately as a function of aspect, and will also yield good estimates of highlight intensities in most cases. However, since there are certain geometries for which the intensities are dependent upon wavelength, care would have to be taken in estimating correct values corresponding to a specific wavelength. In addition to determining identification possibilities, the optical model studies would yield much information concerning the dependence of highlight positions and amplitudes on aspect angle. It was shown in section 5.2 that the statistics of these quantities must be known in order to determine the maximum wavelength for a given probability of resolving highlight points of prescribed spacing.

There are two potential limitations to the practical value of our theory which have not been considered previously, and it is probable that their effect can be assessed only by full scale radar measurements at short microwavelengths. One is due to the presence of irregularities on the aircraft surfaces. The theoretical analysis has tacitly assumed perfectly smooth surfaces, which implies that microwave reflections are perfectly specular. Obviously the presence of irregularities will tend



to cause diffuse reflection, and the effect will become more serious as the wavelength is decreased. This will result in a smearing out of the highlights, thus causing a deterioration in resolution. The wavelength at which this effect becomes appreciable is difficult to estimate, and moreover may depend markedly upon the particular type of aircraft. In this regard it is noted that the modern trend is to smoother surfaces in order to reduce drag and surface heating at high speeds.

The other possible limitation is due to the phenomenon of atmospheric absorption and scattering at short microwavelengths. The primary effect of this phenomenon would be to reduce the overall level of the return signal below a usable value at moderate and long aircraft ranges. It may also produce rapid fading, which in turn could vitiate the resolving capabilities of a conventional radar, but should have appreciably less effect on a multireceiver system.


  
APPENDIX AEQUIPMENT DETAILS

This appendix describes equipment in sufficient detail to indicate the functions of individual circuits and the manner in which those functions are performed. Circuit diagrams are not included because circuits are for the most part quite conventional. Before discussing the two analyzers, a few words will be said about the control equipment.

A.1 Control Equipment.

The controlling units are concentrated in the left hand rack of Fig. 20. They include a Magnecorder tape recorder, a variable low frequency oscillator, an f-m demodulator, oscilloscope and distribution panel. As mentioned in Chapter 6, the data on the tape are in the form of wide-band frequency modulation, with a center frequency of approximately 4000 cps. Thus the output of the playback amplifier must first be passed through the f-m demodulator. The demodulated signal is taken to the distribution panel, and thence to the pre-amplifier/filter selector circuit, at the bottom of the right hand rack in Fig. 20. The output of this unit returns to a gain control on the distribution panel, and is then distributed to the two analyzers. There is a second f-m demodulator, amplifier and filter in the probability distribution analyzer, in case it is desired to operate this equipment simultaneously with the spectrum analyzer.

The outputs from the two analyzers are brought out on the distribution panel, which therefore forms a convenient central



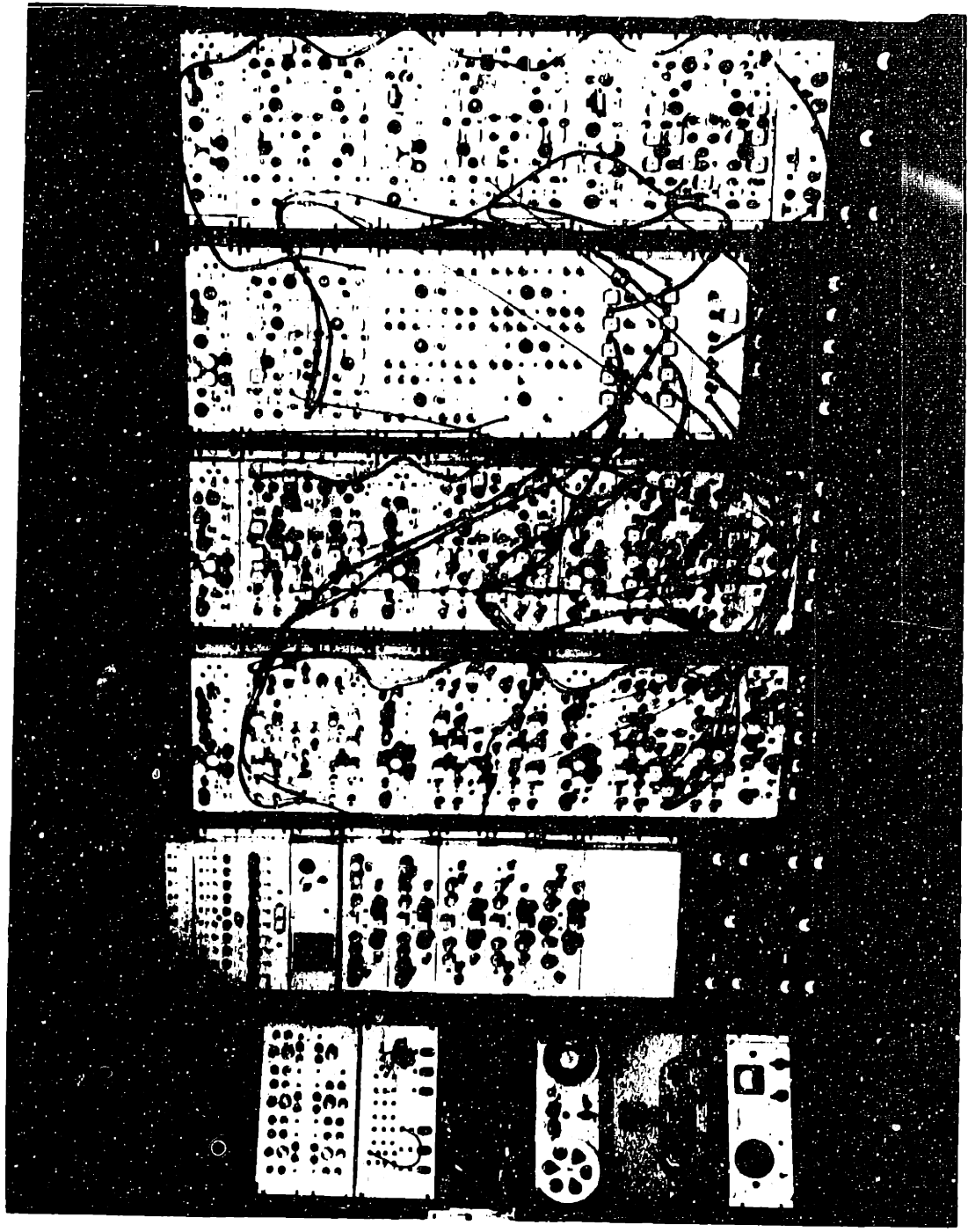
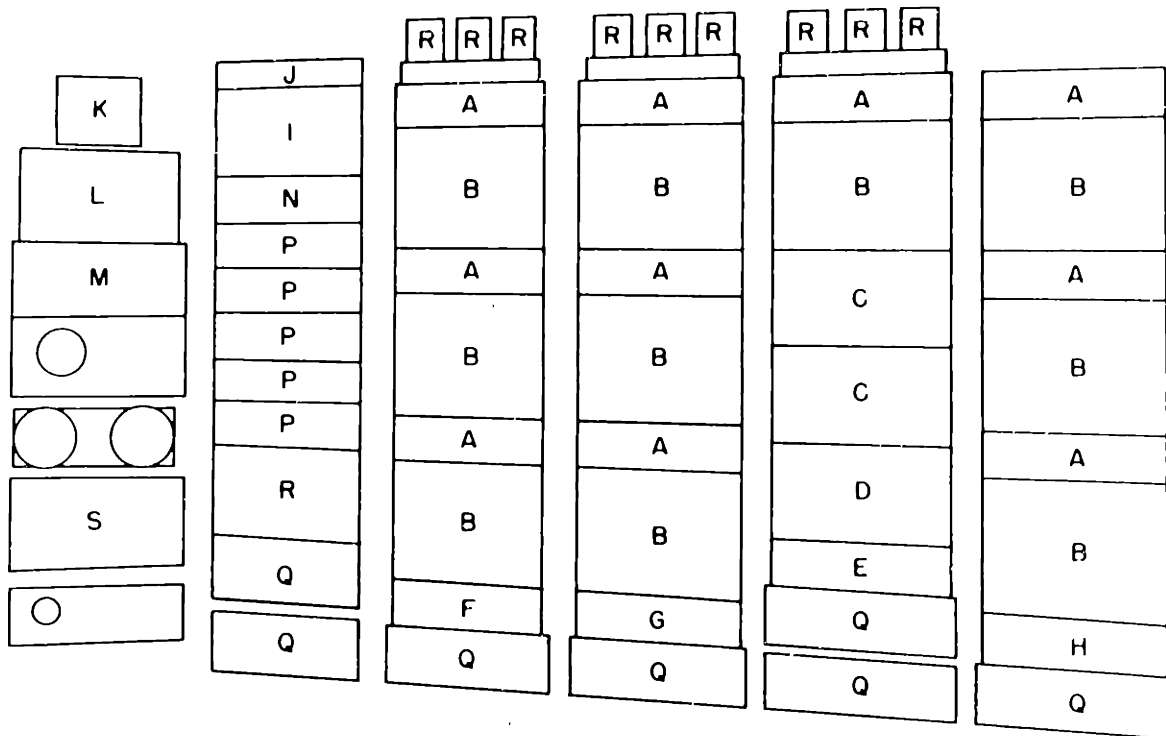


FIGURE 25. PHOTOGRAPH OF SPECTRUM ANALYZER.






LEGEND

- |   |                                       |
|---|---------------------------------------|
| A - LOW FREQUENCY OSCILLATOR                  | K - F-M DEMODULATOR                   |
| B - CHANNEL FILTER CIRCUIT                    | L - SEQUENTIAL SAMPLER                |
| C - SEQUENTIAL SAMPLER                        | M - DISTRIBUTION PANEL                |
| D - 150 KC AND 200 KC OSCILLATORS             | N - PRECISION VOLTAGE MONITOR         |
| E - 500 KC OSCILLATOR                         | P - VOLTAGE REGULATORS                |
| F - LOW FREQUENCY TEST OSCILLATOR             | Q - POWER SUPPLIES                    |
| G - INPUT AMPLIFIER/DISTRIBUTION PANEL        | R - FILAMENT TRANSFORMERS             |
| H - PRE-AMPLIFIER/FILTER SELECTOR CIRCUIT     | S - VARIABLE LOW FREQUENCY OSCILLATOR |
| I - POST-INTEGRATION CIRCUITS                 |                                       |
| J - RECORDING OSCILLOGRAPH DISTRIBUTION PANEL |                                       |

FIGURE 21. IDENTIFICATION CHART FOR PHOTOGRAPH OF SPECTRUM ANALYZER




point for monitoring inputs and outputs with the rack mounted scope. Not shown in Fig. 20 is a Dumont dual beam scope, which was used for photographing the probability and spectral distributions. Associated with it is a trace brightening circuit, which permits the analyzer outputs to appear on the scope for about 1 or 2 hundredths of a second, at uniformly spaced intervals variable from  $\frac{1}{6}$ th to 2 seconds. Such a circuit is necessary because the oscillograph camera ran the 35 mm. film at a continuous rate, whereas it was desired to obtain the effect of frame-by-frame photography.

The variable low frequency oscillator was used as a test signal source for both the analyzers. Another useful piece of test equipment, only partly visible to the left of the rack mounted scope in Fig. 20 is a Voltohmyst meter, which was used to monitor dc voltage levels at various test points in the spectrum analyzer. The remaining unit in the control rack is a sequential sampler circuit, which properly belongs to the spectrum analyzer but could not be accommodated in the remaining racks.

## A.2 Short-Time Spectrum Analyzer.

Figure 21 provides the key to the physical layout of units in the spectrum analyzer. Items N, P, Q and R furnish all the power for the spectrum analyzer and a good deal of that required for the distribution analyzer as well. Each Q unit contains two 400 cps supplies, each supply having a 400 ma capacity. The voltages used in the spectrum analyzer are +300, +150, -100, -150 and -300 volts. The associated voltage regulators are contained in the P panels, two per panel. The regulators use dry cell battery



[REDACTED]

reference, have a loop gain of approximately 2500, and a stability after warmup of  $\pm \frac{1}{100}$  volt. Unit N is a voltage monitor, which contains a standard cell and several precision resistance dividers. The supply voltages are fed to this unit, where they are divided down for comparison with the standard cell. This permits the absolute values of the supply voltages to be accurately maintained over long periods.

#### A.21 Low Frequency Oscillators.

A functional block diagram of one of the low frequency oscillators (labelled A in Fig. 21) appears in Fig. 22. The oscillations are produced by a feedback loop comprising a 6AC7 amplifier, a cathode follower and a twin T network in the feedback path. The rejection frequency of the twin T determines the oscillator frequency. The oscillator output amplitude is stabilized by a slow acting AGC, which controls the grid bias of a 6AC7 AGC amplifier. The AGC circuit contains a delay potentiometer, a 6SN7 cathode follower, a diode averaging detector, a low-pass filter and a second cathode follower. The delay control, in conjunction with the diode, determines the oscillator amplitude at which AGC action is initiated. The low-pass filter determines the AGC time constant. Following the AGC amplifier is a 400 cps twin T trap which eliminates 400 cps ripple, and an RC filter to reduce second harmonic distortion. The half power point of this filter is equal to the oscillator frequency. The quadrature outputs are obtained by simple 45 degree RC lead and lag circuits, whose phase shifts are adjustable by a ganged potentiometer. The output cathode followers can be switched either to the internal

[REDACTED]

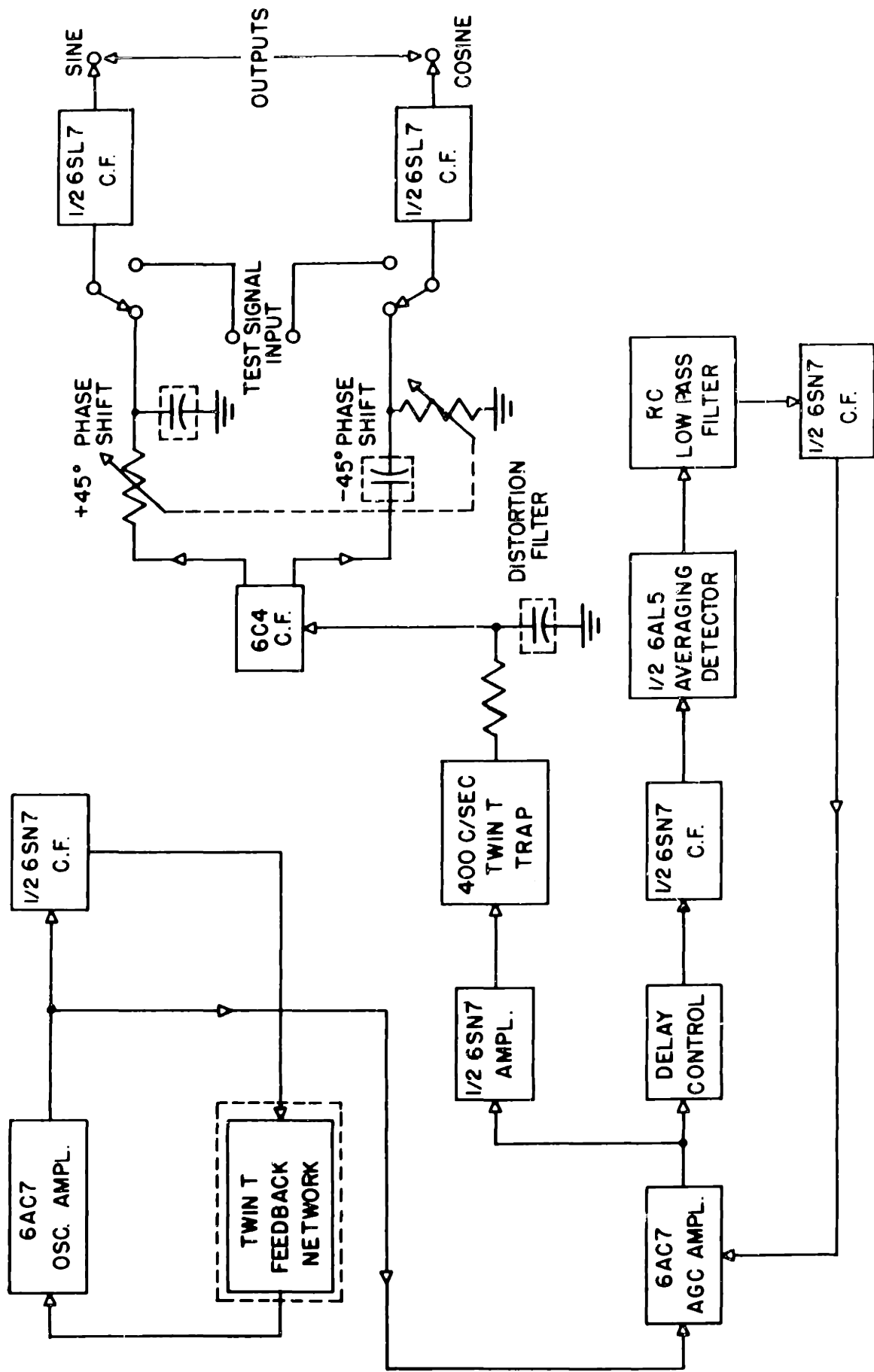


FIGURE 22. FUNCTIONAL BLOCK DIAGRAM OF LOW FREQUENCY OSCILLATOR.

[REDACTED]

oscillator or to an external test oscillator (item F in Fig. 21).

The important design requirements for the low frequency oscillator are that the harmonic distortion be less than 2 percent, the amplitude be maintained constant to within 5 percent, and the dc output levels remain constant to within  $\frac{1}{20}$ th volt after warmup. The distortion requirement is easily satisfied provided the gain around the oscillator feedback loop is properly adjusted. The AGC circuit ensures that the necessary amplitude stability is achieved, while the 6SL7 cathode followers maintain the output dc levels to within approximately  $\pm \frac{1}{50}$ th volt after warmup. The four circuits which are enclosed by broken lines in Fig. 22 are mounted on a plug-in unit, since the values of the involved components depend on the oscillator frequency. This permits any oscillator panel to generate any of the frequencies in the range covered by the plug-in units.

#### A.22 Channel Filter Circuit.

The most complex circuits of the spectrum analyzer are contained in the channel filter panels (labelled B in Fig. 21). The functional block diagram of one of these panels appears in Fig. 23. Referring to this diagram, it is seen that the circuit is symmetrical with respect to the vertical center line, so that only the circuits on the left side, and those on the center line, will be described. Starting near the top left hand corner of the figure,  $\sin \omega_A t$  represents a quadrature output from the associated low frequency oscillator, and  $f(t)$  represents the output waveform whose short-time spectrum is to be obtained. The two voltages are applied to identical suppressed carrier modulators,

[REDACTED]

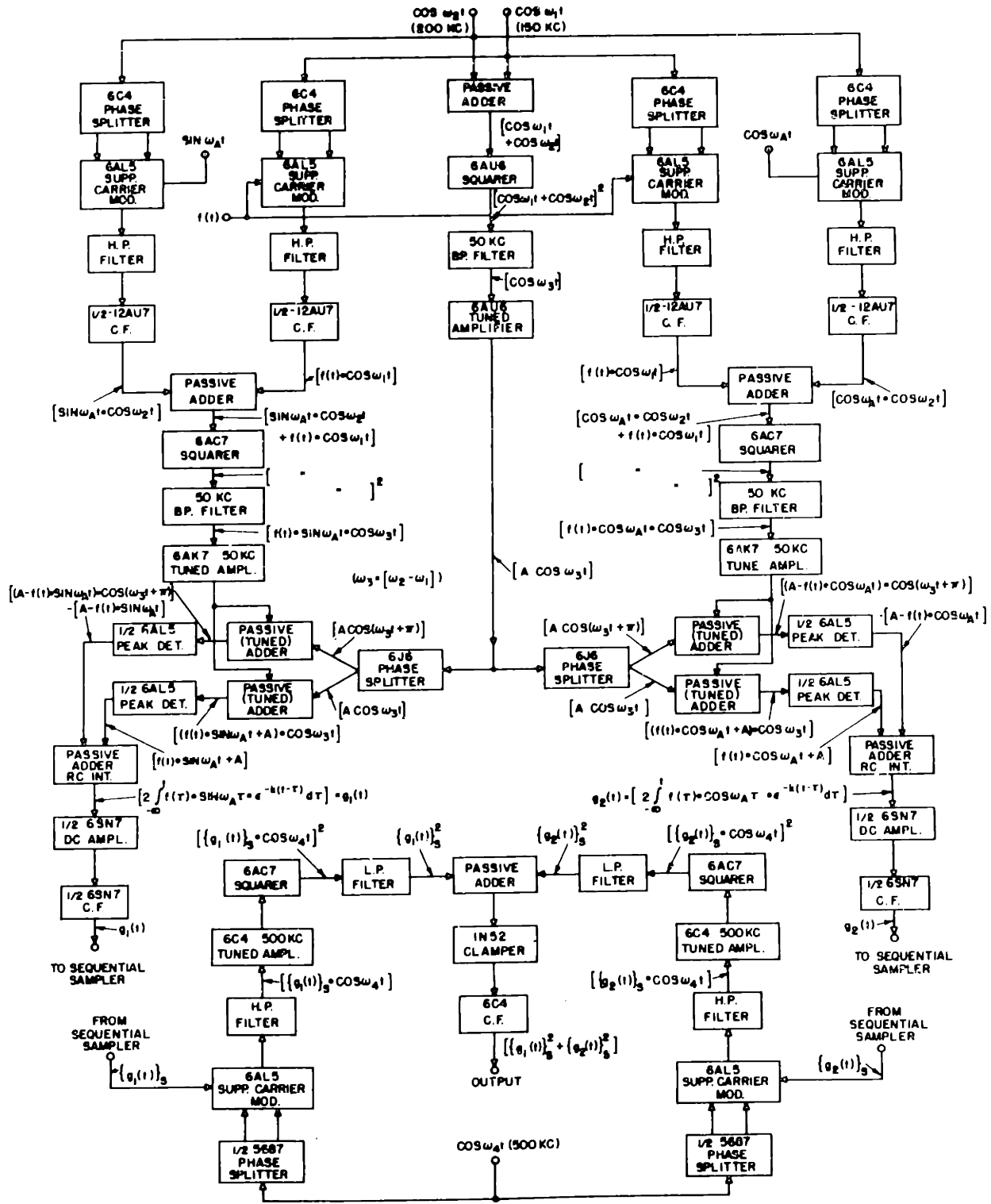


FIGURE 23. FUNCTIONAL BLOCK DIAGRAM OF CHANNEL FILTER CIRCUITS

[REDACTED]

whose carrier frequency voltages,  $\cos \omega_1 t$  and  $\cos \omega_2 t$ , have frequencies of 150 and 200 KC respectively. The modulator is a conventional type in which the two halves of a 6AL5 double diode are connected in series between the plate and cathode of a 6C4 phase splitter, and the modulating voltage is applied from the junction of the diodes to ground. Unwanted low frequency components of the modulation process are removed by RC high-pass filters, and the two suppressed carrier modulations are added at the cathodes of 12AU7 cathode followers, the sum being applied to the grid of a 6AC7.

By using about -3.3 volts bias and a peak-to-peak signal of not more than about 2 volts, the 6AC7 operates essentially as a squarer. Thus its plate current contains a term representing the cross product of the two modulations, namely

$$\left[ 2 f(t) \cdot \sin \omega_A t \cdot \cos \omega_1 t \cdot \cos \omega_2 t \right]$$

and this quantity may be expressed as the sum of two modulations whose mean frequencies are  $(\omega_2 + \omega_1)$  and  $(\omega_2 - \omega_1)$  respectively. The tuned plate circuit of the 6AC7 selects only the difference-frequency suppressed carrier term, namely  $\left[ f(t) \cdot \sin \omega_A t \cdot \cos \omega_3 t \right]$ , where  $\omega_3 = (\omega_2 - \omega_1)$ . The other terms produced by the squaring operation are eliminated by the tuned filter.

The next step is to synchronously demodulate the selected term, and the method used here is to convert it to amplitude modulation by adding a synchronous unmodulated carrier,  $A \cos \omega_3 t$ . The latter is generated by the circuits on the center line of Fig. 23, which form the sum of  $\cos \omega_1 t$  and  $\cos \omega_2 t$ , square it in a 6AU6, and select the difference frequency term by a tuned filter.

[REDACTED]

[REDACTED]

The filter output is amplified and passed through a 6J6 phase splitter, whose outputs are then added to the suppressed carrier term. The amplitude  $A$  of the added carriers must be appreciably greater than the maximum value of  $|f(t) \cdot \sin \omega_A t|$  so that the depth of amplitude modulation remains well below 100 percent. The two amplitude modulations are now applied to individual peak diode detectors, which are connected in such a way as to produce detected output voltages of opposite sign, namely  $-[A - f(t) \cdot \sin \omega_A t]$  and  $[A + f(t) \cdot \sin \omega_A t]$ . Addition of these quantities results in cancellation of the carrier amplitude  $A$  and yields  $[2f(t) \cdot \sin \omega_A t]$ . Although it is not necessary to use balanced detection here, it has the merit that the output is ideally independent of variations in  $A$ .

The sum of the detected outputs is then integrated by a single stage RC low-pass filter, whose time constant determines the bandwidth of the filter channel. The integrated voltage is represented by  $g_1(t)$  for brevity, the full expression being given in Fig. 23. In the actual circuit the summing and integration are performed in a single circuit.

A similar chain of operations is performed on the right hand side of Fig. 23, the resulting integrated function being denoted by  $g_2(t)$  for brevity. The function of the remaining circuits in Fig. 23 is to form the sum of the squares of  $g_1$  and  $g_2$ . Before squaring, both of these functions are passed through sequential sampler circuits (labelled C in Fig. 21) in order to avoid dc drift problems in the squarer output circuits. Thus  $\{g_1(t)\}_S$  denotes the sampled equivalent of  $g_1(t)$ . The sampling rate is

[REDACTED]



[REDACTED]

approximately 600 pulses per second. Sampling at this point is not shown in the simplified block diagram of Fig. 9 since it is not theoretically essential to the operation of the analyzer.

The method of squaring is similar to that used for multiplying. First  $\{g_1(t)\}_s$  is suppressed carrier modulated onto a 500 KC carrier (denoted by  $\omega_4$ ), and then passed through a 6AC7 which acts essentially as a squarer. The low-pass RC filter in the 6AC7 plate circuit then removes all terms except  $\{g_1(t)\}_s^2$ , which is added to a similarly generated term  $\{g_2(t)\}_s^2$ . Their sum is clamped positively by a 1N52 diode, and the output is taken from a 6C4 cathode follower.

Since the output waveform is already sequentially sampled, it could be added to the sampled outputs from the nine remaining channel filters to produce the desired histogram display of the short-time spectrum on an oscilloscope. However there is some undesirable noise on the individual outputs, and its removal is effected by peak detecting and post integrating each output in panel I (Fig. 21). The post integration time constant is normally somewhat shorter than that used in the channel filter circuits. The outputs from the post integrators are sequentially sampled a second time (in panel L, Fig. 21), added, and applied to an oscilloscope.

The overall design requirement for the channel filter circuit was that it could be aligned to reproduce the specified functional operations to an accuracy of better than  $\pm 10$  percent over a range of 27 db at the output, and should be stable enough to maintain this alignment over an operating period of 1 or 2 hours. The

[REDACTED]

[REDACTED]

equipment did not meet the stability requirement, mainly due to dc drifts in the output stage of the multiplying circuits. The primary sources of instability were known, but time did not permit them to be effectively corrected, and in any case the circuit performance was just adequate to carry out the experimental work satisfactorily.

One characteristic of the channel filter circuits was that they were very sensitive to overload. Specifically, when the quadrature outputs of the low-frequency oscillators were set at  $6\frac{1}{2}$  volts peak-to-peak, the peak-to-peak values of the signal waveform  $f(t)$  could not exceed about 12 volts at the channel filter input terminals without causing large spurious responses at the outputs of all channels. The reason for the sudden onset of overload is that a number of the active circuits in each channel were operated at high average signal levels, thus an increase in level beyond the critical value drove a number of tubes into distortion simultaneously. However, the maximum operating level of the spectrum analyzer as a whole was determined by the post integration circuits, whose cathode followers produced appreciable limiting before overload of the channel filters occurred. It was therefore necessary to adjust the level of  $f(t)$  at the beginning of each analyzer run such that its peak-swings produced negligible limiting in the post integrator during the run.

#### A.23 Sequential Sampler.

Two sequential samplers were used in the spectrum analyzer and one in the probability distribution analyzer, and all used essentially the same circuits, whose operation will now be described.

[REDACTED]

[REDACTED]

A sampler which is designed to sample  $N$  channels sequentially consists of  $(N + 2)$  one-shot pulse generators connected in a ring, so that the trailing edge of the output pulse of the  $n$ th generator triggers the  $(n + 1)$ st generator for any  $n$ , and the  $(N + 2)$ nd generator triggers the first one. Thus the ring continues to drive itself as soon as one of the generators is pulsed. Figure 24(a) illustrates the ring operation.

With each of the first  $N$  generators is associated a diode switch which is closed for the pulse duration of the associated generator. The  $(N + 1)$ st and  $(N + 2)$ nd generators do not drive switches, but merely produce dead time between each complete cycle of the  $N$  switches, in order to provide a suitable display of the  $N$  sampled channels on a scope. A trigger pulse, generated at the end of the  $(N + 1)$ st pulse, causes the cathode ray tube spot to start a new sweep. The timing sequence of the pulses is shown in Fig. 24(b).

Each one-shot pulse generator consists of a screen-coupled phantastron, a phase splitter and a pulse inverter, as shown in Fig. 24(c). The negative pulse from the pulse inverter of the succeeding generator is differentiated, so that its trailing edge produces a positive trigger pulse which is applied to the suppressor of the 6AS6 phantastron. The pulse duration of the phantastron is determined by the time constant of an RC coupling circuit between its plate and grid. The resulting positive pulse from the phantastron screen is applied to both the phase splitter and the pulse inverter. Pulses of opposite polarity from the former drive a bridge of 6AL5 diodes into conduction at junctions

[REDACTED]



[REDACTED]

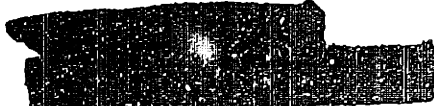
a and b, while the signal which is to be sampled is applied at junction c. The sampled output appears at junction d.

#### A.24 Remarks on the Spectrum Analyzer Design.

The complexity of the spectrum analyzer arises largely from the particular type of active filters employed in the channel circuits. This type was used because it appeared to offer the only means of obtaining a set of filters whose center frequencies and bandwidths could be accurately set to various prescribed values, including a minimum bandwidth setting of  $\frac{1}{2}$  cps and an accuracy in center frequency spacing of at least  $\frac{1}{20}$  cps. As a result of the experimental work it was found subsequently that 2 cps was the smallest bandwidth required. Thus it appears that a simpler and more conventional design might have been possible, namely the waveforms to be analyzed could have been translated in frequency to 200 cps, and a bank of filters covering the band 200 - 280 cps (corresponding to 0 - 80 cps before translation) could then have been used.

Since 2 cps is now the minimum required frequency separation, a center frequency stability of  $\frac{1}{5}$  cps at 200 cps., or about 1 part in 1000, would suffice for each filter. Also the maximum filter Q would be about  $\frac{250}{2}$ , or 125, which could be achieved at 200 cps by toroids having a Q of 30, in conjunction with Q multipliers. These requirements can be met without great difficulty. Filter bandwidths could be altered by changing the Q multiplying factor, while adjustment of center frequency would require variable tuning condensers. The output of each filter would be detected and then sequentially sampled as before.

[REDACTED]




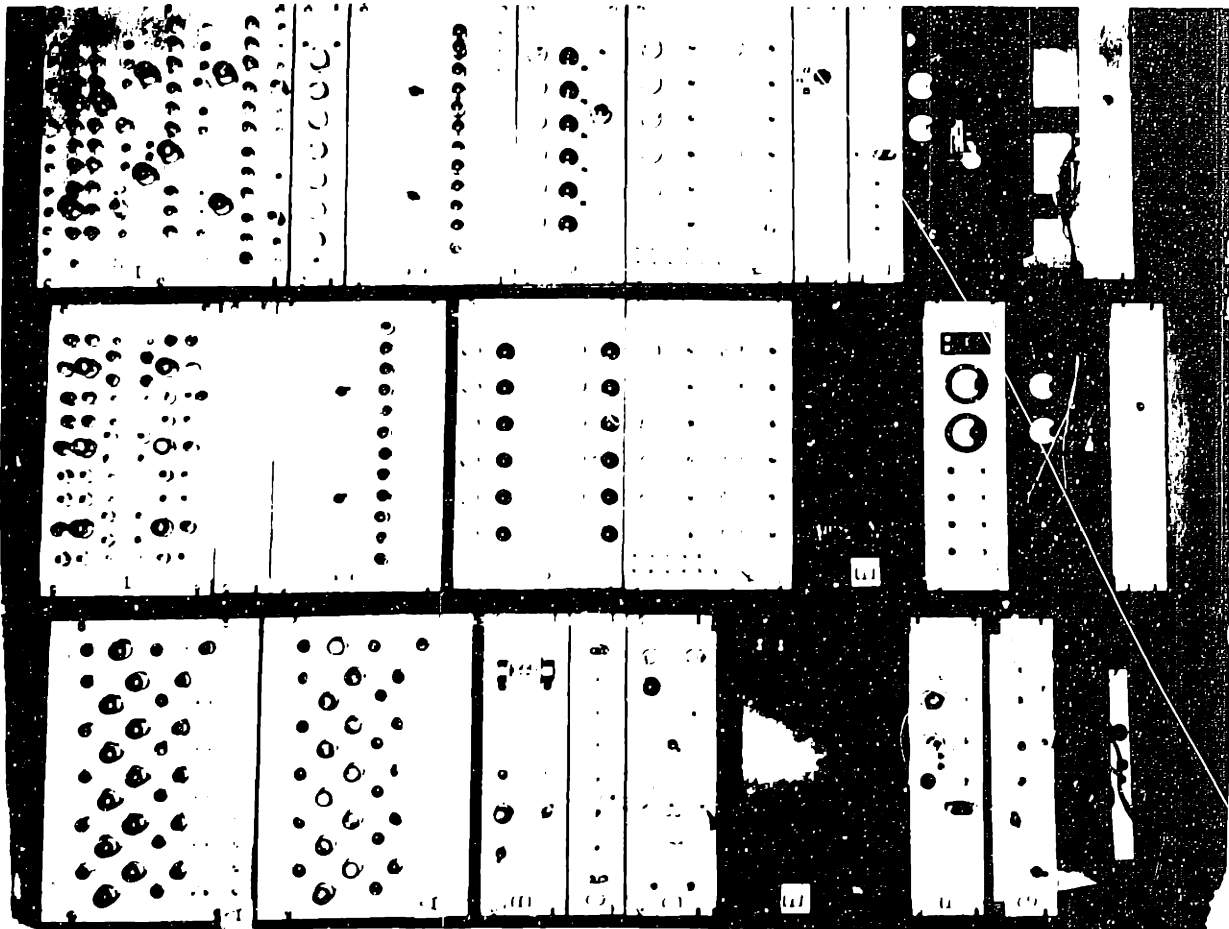
The resulting simplification should be substantial. For example the low-frequency oscillators and the dual circuits (operating in phase quadrature) in the existing channel filters would be eliminated. Elimination of the latter occurs because it is now no longer necessary to square and add quadrature components to obtain the square of the spectral amplitude; in the proposed circuits this would be done by a simple square law detector following each filter. If the spectral amplitude rather than its square is desired, a linear detector would be used instead.

### A.3 Short-Time Distribution Analyzer.

The physical layout of units in the distribution analyzer is shown in Fig. 25, and a detailed block diagram of one complete slicing channel, denoted as the  $n$ th, appears in Fig. 26. The broken lines in Fig. 26 indicate the physical grouping of circuits in the analyzer, the upper case letters providing cross-reference between the units in the block diagram and the equipment layout in the photograph. Referring to the block diagram, the waveform  $f(t)$  which is to be analyzed is passed through a variable gain amplifier followed by a fixed gain dc amplifier. The output of the dc amplifier is capacity coupled to 24 identical level selector circuits. The purpose of the selectors and the immediately following anti-coincidence circuits is to divide  $f(t)$  into 23 horizontal amplitude slices of equal width.

The voltage transfer characteristic of the level selectors is shown in Fig. 27(a). It is essentially the characteristic of a bistable flip-flop, whose state changes when its input voltage





LEGEND

- A - LEVEL SELECTOR CHANNELS
- B - GAIN CONTROL AMPL/ZERO OFFSET
- C - INPUT DISTRIBUTION PANEL
- D - TRIANGULAR WAVEFORM GENERATOR
- E - COUPLING CAPACITOR BOARDS
- F - DC AMPLIFIER
- G - FM DEMODULATOR
- H - SEQUENTIAL SAMPLER
- I - INTEGRATING CHANNELS
- J - DRIVER CHANNELS
- K - ANTI-COINCIDENCE CHANNELS
- L - OUTPUT PANEL

FIGURE 25 PHOTOGRAPH OF DISTRIBUTION ANALYZER

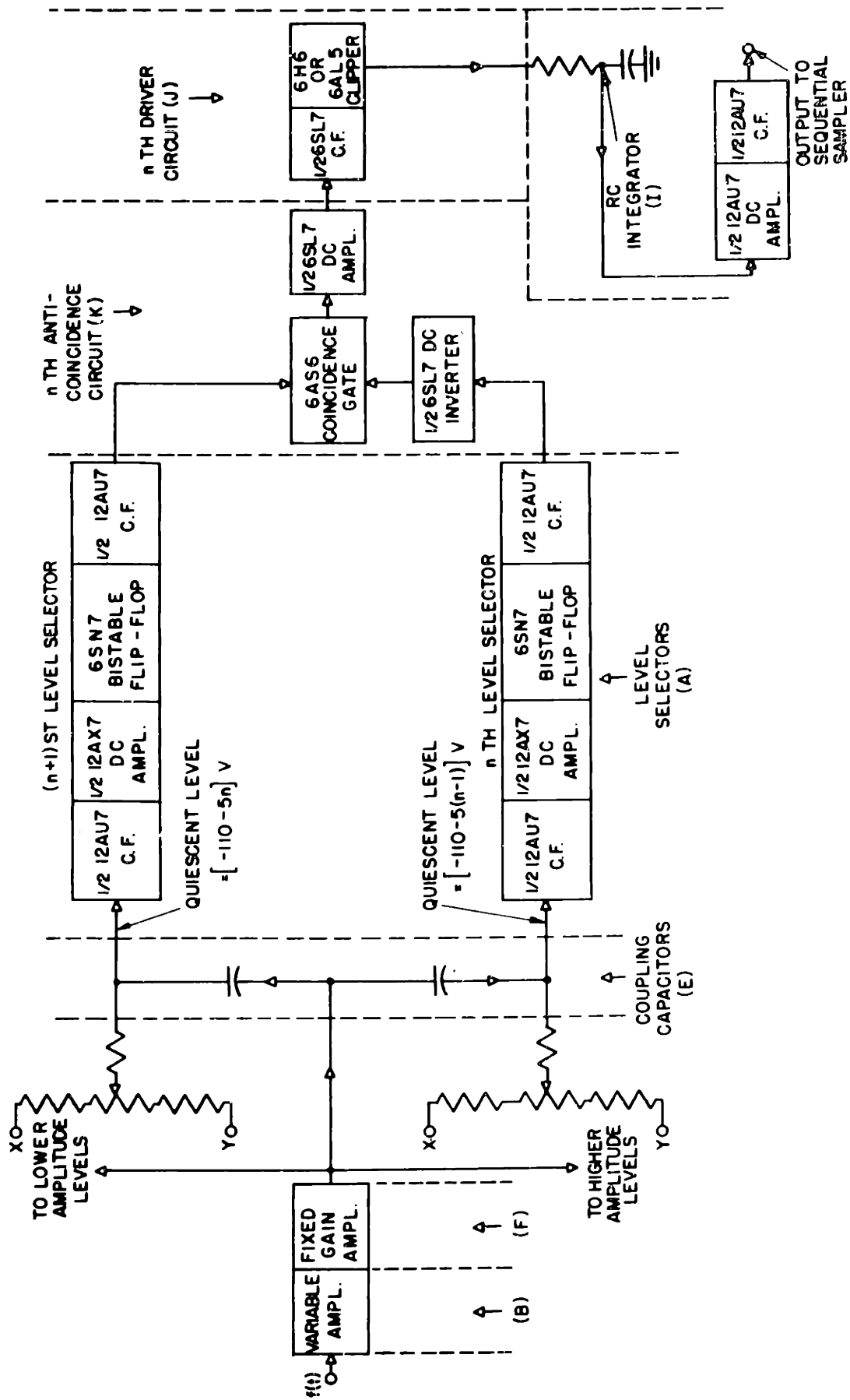


FIGURE 26. FUNCTIONAL BLOCK DIAGRAM OF THE  $n$ th SLICING CHANNEL OF THE DISTRIBUTION ANALYZER



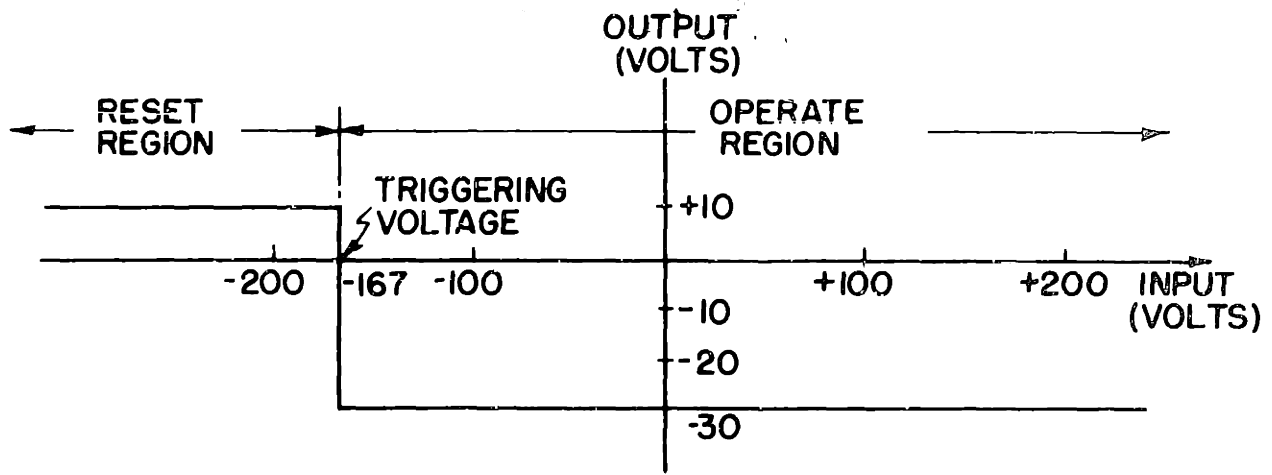


FIG. 27(a)-TRANSFER CHARACTERISTIC OF LEVEL SELECTOR

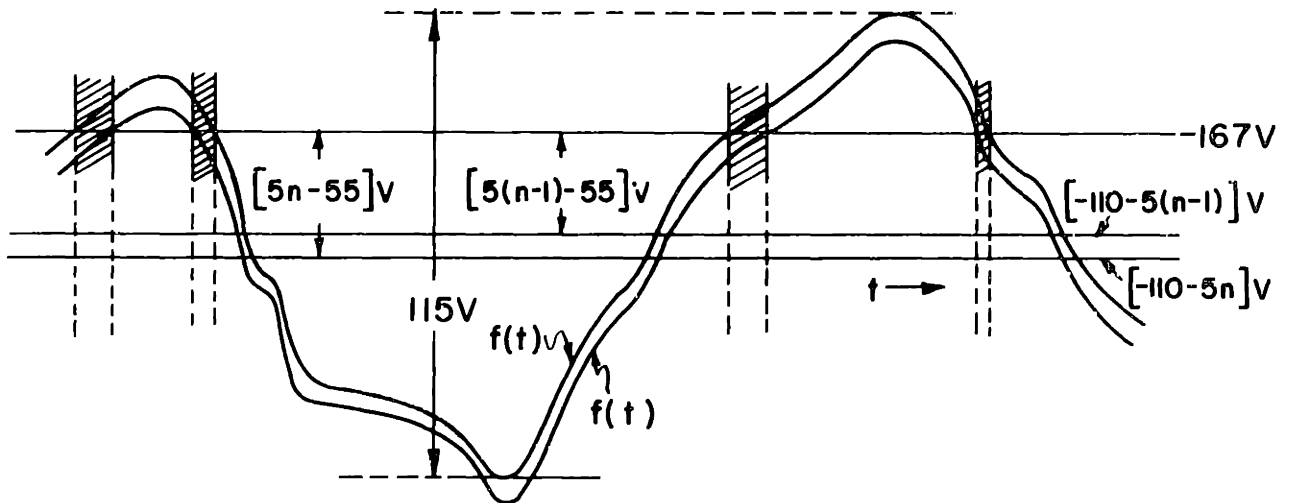


FIG. 27(b)-WAVEFORMS AT INPUTS TO  $n$ th AND  $(n+1)$ st LEVEL SELECTORS



FIG. 27(c)-OUTPUT OF  $n$ th ANTI-COINCIDENCE CIRCUIT

FIGURE 27.

Level Selector and Anti-Coincidence Operation.

[REDACTED]

passes through -167 volts, which we shall hereafter refer to as the triggering voltage. For clarity we shall use the following terminology. The level selector is said to be "operated" when it is triggered by a rising voltage at the selector input, and to be "reset" when triggered by a falling voltage. Thus in the region to the right of -167 volts in Fig. 27(a) the level selector is in the operated condition while to the left of -167 volts it is in the reset condition. The level selector consists of a 12AU7 cathode follower, a 12AX7 dc amplifier, a 6SN7 bistable flip-flop (sometimes called a Schmidt trigger circuit), and a second cathode follower.

The level selecting phase of the slicing process is performed by setting the mean value of  $f(t)$  at 24 equally spaced voltages, distributed above and below the triggering voltage. Since the peak-to-peak amplitude of  $f(t)$  is 115 volts at the selector inputs, the spacing of the levels is  $\frac{115}{23} = 5$  volts, so the quiescent voltages of successive selector inputs are set 5 volts apart. The quiescent voltages are obtained from precision resistance dividers connected between two supply voltages denoted as X and Y in Fig. 26. The latter can be varied synchronously by ganged potentiometers, such that  $(X - Y)$  remains constant. If  $f(t)$  makes equal peak swings about its mean value, as is the case if its amplitude distribution is symmetrical about the mean, X and Y are set so that the quiescent voltage of number one level selector is -110 volts, while that of number 24 is -225 volts. These values differ by 115 volts, and are equally spaced above and below the triggering voltage. If  $f(t)$  is asymmetrically distributed about its mean, the whole waveform is shifted by varying X and Y,

[REDACTED]

to ensure that the total peak-to-peak range of the waveform triggers all the level selectors. In the symmetrical case, the quiescent voltage at the  $n$ th selector input is  $[-110-5(n-1)]$  volts as indicated in Fig. 26.

The outputs of the  $n$ th and  $(n + 1)$ st level selectors are combined in the  $n$ th anti-coincidence circuit, which produces a positive output only when the  $n$ th level selector is in the operated condition and the  $(n + 1)$ st level selector is in the reset condition. For the remaining two conditions, namely both selectors operated and both reset, the anti-coincidence circuit gives a negative output. Referring to Fig. 27(b), it is seen that the shaded areas represent the times when the anti-coincidence output is positive, and these are the times when the instantaneous value of  $f(t)$  lies between  $[5(n - 1) - 55]$  and  $[5n - 55]$  volts at the selector inputs. Calling the region between these two amplitude levels the  $n$ th amplitude slice, it follows that the combined action of the  $n$ th and  $(n + 1)$ st level selectors and the  $n$ th anti-coincidence circuit is to produce a positive output pulse when  $f(t)$  lies in the  $n$ th slice, and negative otherwise, as indicated in Fig. 27(c).

The anti-coincidence circuit consists of a 6SL7 dc converter, a 6AS6 coincidence gate and a 6SL7 dc amplifier. The output of the  $n$ th selector is passed through the inverter and applied to the suppressor grid of the 6AS6, while the  $(n + 1)$ st selector output is applied directly to the 6AS6 control grid. The 6AS6 is cut off unless both grids are positive, at which time its plate goes negative. This causes the 6SL7 amplifier to cut off, so that

[REDACTED]

its plate goes positive, producing the desired positive pulse.

The driver in Fig. 26 circuit comprises a 6SL7 cathode follower and either a 6H6 or 6AL5 diode. The latter clips both the positive and negative excursions of the applied waveform, so that the output assumes only the values 0 and +16 volts. The integrator is the simple RC type, followed by a 12AU7 dc amplifier and cathode follower. The cathode follower output is applied to the sequential sampler along with the outputs from the 22 remaining slicing channels.

In operation, the distribution analyzer was sufficiently stable to maintain its alignment within 5 percent for a period of two or three hours after warmup. The only daily alignment required was to adjust the gain and zero set potentiometers of the dc amplifiers following the integrators. To facilitate this procedure, a triangle wave generator was used, whose amplitude distribution is ideally flat between its two peak values. First the zero set controls were adjusted so that all the sampled outputs were zero with no input to the analyzer, then the triangle wave was applied and the gain controls adjusted so that all channels had the same output amplitude. About once a month it was necessary to adjust the potentiometers at the level selector inputs so that successive level selectors triggered for each 5 volt increment in the amplitude of a test sine wave. The purpose of this adjustment is to equalize the widths of all the amplitude slices.

[REDACTED]

APPENDIX B

EVALUATION OF THE PROJECTED DISTRIBUTION FROM ITS AUTOCORRELATION

We wish to consider in more detail the problem posed in section 2.4, which is to determine  $|A(y)|$  from  $|R_A(y)|_+$ , where these functions are given by Eqs. (28) and (27) respectively. The problem has two parts. The first is to determine under what conditions (if any) a unique solution exists. The second is to evolve a method for finding the solution. At the time of writing, the author has been unable to obtain a general solution to the first part. It appears that a proof by induction should be possible, but certain steps in the proof are still missing. However, a method of finding a solution has been evolved, and its application to numerous examples strongly indicates that the solution is unique under certain conditions. This method will be described after the nature of the problem has been more fully explained.

It was shown in section 2.4 that the problem reduces to determining the set of number pairs  $\{K_m; y_m\}$ , where  $m = 1, 2, \dots, M$ , from the set of number pairs  $\{K_m K_n; y_m - y_n\}$ , where  $m = 2, 3, \dots, M$ ;  $n = 1, 2, \dots, M-1$ ; and  $m > n$ . For brevity we shall denote  $K_m K_n$  by  $K_{mn}$ , and  $(y_m - y_n)$  by  $a_{mn}$ .

It is evident that the set  $\{K_m\}$  can be determined only after the set  $\{y_m\}$  has been determined. This is because the members of the set  $\{K_{mn}\}$  are not given to us with the identifying subscripts attached. They are merely a set of real numbers, and we do not know which pair of subscripts to associate with each until the set  $\{y_m\}$  is known. When the latter set

[REDACTED]

is determined, we can order it. Suppose the subscripts are chosen so that the following rule of ordering is fulfilled.

$$y_1 < y_2 < y_3 < \dots < y_{M-1} < y_M$$

From the above ordered set we can regenerate the set  $\{a_{mn}\}$ , and therefore determine the correct subscript pairs to associate with each member of  $\{K_{mn}\}$ . It is now a simple matter to solve for each  $K_m$ , since:

$$K_m = \left[ \frac{K_{mn} K_{mp}}{K_{np}} \right]^{\frac{1}{2}}, \text{ or: } K_m = \left[ \frac{K_{rm} K_{qm}}{K_{nq}} \right]^{\frac{1}{2}}$$

In the first expression, n and p are any subscripts such that  $m \neq n \neq p$ , while in the second expression r and q are any subscripts such that  $r \neq q \neq m$ .

The crux of the problem is therefore to determine the set  $\{y_m\}$  from the set  $\{a_{mn}\}$ . Although we have been unable to prove it in general, we believe that  $\{y_m\}$  is uniquely derivable from  $\{a_{mn}\}$  provided the members of the latter set are all different. It is also suspected that this result is true when not more than two of the  $a_{mn}$  are equal. However we shall confine attention to the case where none are equal. It can readily be shown in this case that there are  $N = \frac{1}{2}(M)(M-1)$  members of  $\{a_{mn}\}$ . We know that there is at least one set  $\{y_m\}$  which is a solution to the problem, namely the set of projected highlight positions which originally generated the set  $\{a_{mn}\}$ . We therefore wish to show that there are no other sets of M numbers which can generate the same  $\{a_{mn}\}$ . We

[REDACTED]

shall now show how to go about constructing a  $\{y\}$  set from the given  $\{a\}$  set.

To clarify the procedure, introduce a new set of symbols  $\{a_k\}$  to replace  $\{a_{mn}\}$ . The new subscripts are to be chosen so that the following rule of ordering is fulfilled.

$$a_1 < a_2 < a_3 < \dots < a_{N-1} < a_N$$

It is evident that the difference  $(y_M - y_1)$  is  $= a_N$  because  $y_1$  and  $y_M$  are the end points of the array of projected highlights. It is also evident that  $y_1$  may be chosen arbitrarily, because the set  $\{a_k\}$  determines only differences between projected highlight positions, and not absolute values.

Therefore we shall choose  $y_1 = 0$ . A little thought will also show that the same set  $\{a_k\}$  would result from either  $\{y_m\}$  or the set obtained by forming the mirror image of  $\{y_m\}$  in any plane perpendicular to the  $y$  axis. This is because the operation of mirror imaging does not change any of the projected distances between points. Hence there is an ambiguity in determining the projected distribution from its autocorrelation function, in that we have lost the sense of ordering of the projected points. For example, in computing the projected highlight distribution from its autocorrelation function for a broadside aircraft aspect, we would not know which end of the distribution to associate with the aircraft's nose, and which end with the tail.

The procedure for deriving a  $\{y\}$  set may now be described. From the ordered set  $\{a_k\}$ , pick out all pairs  $(a_j, a_k)$

[REDACTED]

defined as follows:  $a_j$  is  $< \frac{1}{2} a_N$ , and  $a_k = (a_N - a_j)$ .

There will be at least (M-2) pairs which satisfy these conditions, because there are (M-2) remaining y's to be determined\*, and the m th y generates the following two members of  $\{a_{mn}\}$ , among others:

$$a_{m1} = (y_m - y_1) = a_j$$

and

$$a_{Mm} = (y_M - y_m) = [(y_M - y_1) - (y_m - y_1)] = (a_N - a_j) = a_k$$

We shall consider the case of exactly (M-2) such pairs, since it is unlikely that there will be more than this. The remaining (M-2) y's are to be selected one from each of the number pairs  $(a_j, a_k)$ . For clarity we shall identify these number pairs by adding superscripts thus:  $(a_j^p, a_k^p)$ ,  $p = 1, 2, \dots, (M-2)$ . The p superscripts are chosen to satisfy the ordering:

$$a_k^1 < a_j^2 < \dots < a_j^{M-2} < (\frac{1}{2} a_N)$$

This ordering implies that

$$a_k^1 > a_k^2 > \dots > a_k^{M-2} > (\frac{1}{2} a_N)$$

It is evident that we must choose  $y_2 = a_j^1$ , due to the rules of ordering. The remaining (M-3) y's can be chosen in

\*  $y_1$  and  $y_M$  are already determined, because  $y_1$  is selected = 0, and  $y_M = (y_1 + a_N)$ .



any one of  $(2)^{M-3}$  ways. The procedure is to test the possibilities in a systematic manner, until one is found that generates the correct set  $\{a_k\}$ . For example, we could test all the sequences for which  $y_3 = a_j^2$ , then all those for which  $y_3 = a_j^3$ , followed by those for which  $y_3 = a_j^4$ , etc., the last two being the sequences for which  $y_3 = a_j^{M-2}$  and  $a_k^{M-2}$  respectively. The number of sequences in each of these categories is  $(2)^{M-4}$ ,  $(2)^{M-5}$ ,  $(2)^1$ ,  $(2)^0$  and  $(2)^0$  respectively. The method of testing a  $\{y\}$  sequence is to start evaluating the members of the  $\{a\}$  set corresponding to that sequence, and discarding it as soon as a number is found which does not belong to the given set  $\{a_k\}$ .

The procedure will be illustrated by the following example in which  $M=6$ . The given set  $\{a_k\}$  is shown in Fig. 28. For simplicity we have chosen the members of  $\{a_k\}$  to be integers, as follows:

$$\{a_k\} = (1, 2, 3, 4, 5, 6, 7, 8, 9, 10, 11, 12, 17, 18, 21)$$

Examination of this set shows that the admissible pairs from which  $(y_2, y_3, y_4, y_5)$  must be chosen are  $(a_3, a_{14})$ ,  $(a_4, a_{13})$ ,  $(a_9, a_{12})$  and  $(a_{10}, a_{11})$ . The appropriate  $p$  superscripts to be associated with these pairs are indicated in the figure. As explained previously,  $y_2$  is to be chosen =  $a_3$ . Hence we are faced only with the choice of  $y_3, y_4,$  and  $y_5$ . There are  $2^{(6-3)} = 2^3 = 8$  possible choices, which are enumerated in tabular form in the figure. Upon testing these choices in the order indicated, it is found that choice No. 2 yields the correct set  $\{a_k\}$ , while no other choice does. Choice No. 2 corresponds to the

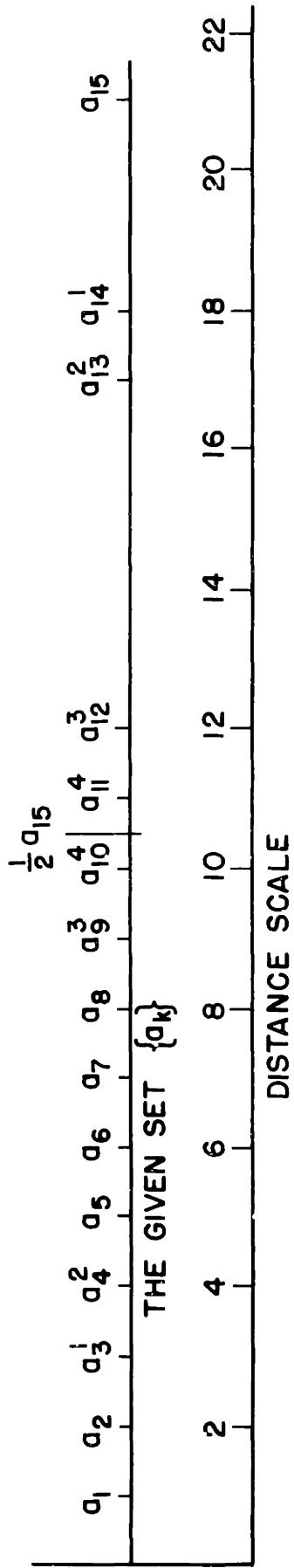


TABLE OF POSSIBLE CHOICES OF  $y_3, y_4,$  AND  $y_5$

CATEGORY #	CHOICE #	$y_3$	$y_4$	$y_5$
1	1	$a_4^2$	$a_9^3$	$a_{10}^4$
	2	$a_4^2$	$a_9^3$	$a_{11}^4$
	3	$a_4^2$	$a_{10}^4$	$a_{12}^3$
	4	$a_4^2$	$a_{11}^4$	$a_{12}^3$
2	5	$a_9^3$	$a_{10}^4$	$a_{13}^2$
	6	$a_9^3$	$a_{11}^4$	$a_{13}^2$
3	7	$a_{10}^4$	$a_{12}^3$	$a_{13}^2$
	8	$a_{11}^4$	$a_{12}^3$	$a_{13}^2$

FIGURE 28.  
An Example for  $M = 6$ .

following complete set of y's: (0, 3, 4, 9, 11, 21)

It is to be noted that we can find a set of more than six points which apparently generates the same  $\{a\}$  set as was given in the above example. For instance, if in addition to the six y values determined above, we add  $y = 12$ , a quick check will show that this additional y generates no a's whose values are different from the existing ones. The explanation is that, strictly speaking, we have generated a different set, say  $\{a\}'$ , but several members of this set have the same value. Hence  $\{a\}'$  and  $\{a\}$  are equivalent insofar as they contain the same numbers. The above example confirms the fact that a unique solution does not exist unless all the members of the corresponding  $\{a\}$  set are different, or unless only two at most are equal.

## BIOGRAPHICAL NOTE

Douglas Byron Armstrong was born on March 17, 1918, in Toronto, Canada. The latter part of his primary schooling, and his secondary education, were obtained at the University of Toronto Schools. In 1936 he entered the Mathematics and Physics course at the University of Toronto, specializing in physics in the junior and senior years, and graduating with a B.A. degree in 1940. He was enlisted as a radar officer in the Canadian Naval Volunteer Reserve from August 1940 to November 1945, and was on loan to the British navy during this entire period.

He joined the Canadian Marconi Company, Montreal, in December 1945, where he was engaged in the design of radio broadcast antenna arrays and in transmitter development. He entered M.I.T. as a full time research assistant and graduate student in September 1948, and received the M.S. degree in electrical engineering in February 1951. His work was in connection with classified military projects. He joined the switching research group at the Bell Telephone Laboratories, Murray Hill, in December 1954.


He is a member of Sigma Xi, and the Canadian Naval Radar Officers' Association.

[REDACTED]

BIBLIOGRAPHY

1. D. Kerr; "Propagation of Short Radio Waves"; Radiation Laboratory Series; Vol. 13.
  2. J. B. Angell: "Errors in Angle Tracking Radar Systems Caused by Complex Targets", Meteor Report No. 77; Research Laboratory of Electronics, M.I.T.; Oct. 15, 1951.
  3. Lawson and Uhlenbeck; "Threshold Signals"; Radiation Laboratory Series; Vol. 24; Sect. 10.5.
  4. Philco Corporation (Research Division); "Summary Engineering Report on Airborne Detection of Moving Ground Targets"; April 23, 1952.
  5. Franklin Institute Research Laboratories; "Research on Radar Terrain Return Theory, Instrumentation and Techniques"; Franklin Inst. Lab. Report Nos. P-2186-3 through P-2186-30; 1950-1953.
  6. Lincoln Laboratories; A. S. Soltes, J. I. Elkind, P. H. Baldwin, W. H. Huggins, J. C. R. Licklider; "An Application of Aural Presentation"; Preliminary Report of Project Buzz Saw, Lincoln Laboratory, M.I.T., Technical Report No. 53, July 30, 1954.
  7. Naval Research Laboratories; "Quantitative Measurements of Radar Echoes from Aircraft"; A sequence of reports numbered I through X; 1950 - 1953.
  8. Ohio State University; "Echo Measurements of Various Aircraft"; O. S. U. project report Nos. 475-1 through 475-5; 1951 - 1953.
  9. Willow Run Research Center, University of Michigan; "Studies in Radar Cross Sections"; A sequence of reports numbered I through XII; 1950 - 1953.
- [REDACTED]

10. R. H. Delano; "A Theory of Target Glint or Angular Scintillation in Radar Tracking"; Proc. I.R.R.; Vol. 41 (1953); pg. 1778.
11. S. Silver; "Microwave Antenna Theory and Design"; Radiation Laboratory Series; Vol. 12.
12. Slater and Frank; "Electromagnetism"; McGraw Hill Book Co.; 1947.
13. R. C. Spencer; "Back Scattering from Conducting Surfaces"; Radiation Laboratory Report No. 661, Jan. 26, 1945. Also Air Force Cambridge Research Laboratory Report No. E-5070.
14. P. M. Marcus; "Reflection of Radiation from Curved Surfaces"; Radiation Laboratory Report No. 1029; Jan. 16, 1946.
15. Carlson and Goudsmit; "Microwave Radar Reflections"; Radiation Laboratory Report No. 195; Feb. 20, 1943.
16. Goudsmit and Weiss; "Possible Measurements of Radar Echoes by Use of Target Models"; Radiation Laboratory Report No. 196; Mar. 4, 1943.
17. Reports Nos. VI, VII and VIII of Reference 9. (Respectively U.M.M. 106, 108 and 115.)
18. Jenkins and White; "Fundamentals of Physical Optics"; McGraw Hill; 1st Ed. (1937).
19. Koenig, Dunn and Lacy; "The Sound Spectrograph"; Jour. Acous. Soc. Am.; Vol. 18 (1946); Pg. 19.
20. J. Marique; "The Response of a Circuit to a Linear-Frequency-Sweep Voltage"; Onde. Elect.; Vol. 13 (1951); pp. 313-315.
21. W. R. Bennett; "Distribution of the Sum of Randomly Phased Components"; Quart. App. Math; Vol. 5 (1948); pp. 385-393.



22. Nakagami; "Study on the Resultant Amplitude of Many  
Vibrations whose Phases and Amplitudes are at Random";  
Nippon Elect. Comm. Engineering (Tokyo); No. 22 (Oct. 1940);  
pp. 69 - 92.